
# Metal-Organic Framework-Based Composites for Adsorption-Driven Heat Transformation Applications and Sulfur Dioxide Adsorption Applications

Inaugural dissertation
presented to the Faculty of Mathematics and Natural Sciences
of Heinrich-Heine-University Düsseldorf
for the degree of
Doctor of Philosophy (Ph.D.) in Natural Sciences

by

**Yangyang Sun**
from Jilin, China

Düsseldorf, September 2021

from the Institute for Inorganic and Structural Chemistry I

at Heinrich-Heine-University Düsseldorf

Printed by permission of the Faculty of Mathematics and Natural Sciences of

Heinrich-Heine-University Düsseldorf

Examiners:

1. Prof. Dr. Christoph Janiak

2. Prof. Dr. Christian Ganter

Date of the oral defense: 16 September 2021

## Eidesstattliche Erklärung

Ich versichere an Eides statt, dass die Dissertation von mir selbstständig und ohne unzulässige fremde Hilfe unter Beachtung der „Grundsätze zur Sicherung guter wissenschaftlicher Praxis“ an der Heinrich-Heine-Universität Düsseldorf erstellt worden ist. Die aus fremden Quellen direkt oder indirekt übernommenen Gedanken sind als solche kenntlich gemacht. Die Arbeit wurde bisher weder im Inland noch im Ausland in gleicher oder ähnlicher Form einer anderen Prüfungsbehörde vorgelegt. Es wurden keine früheren erfolglosen Promotionsversuche unternommen.

| | |
|---|---|
| ……..... | ……..... |
| Ort, Datum | Unterschrift |

## Acknowledgments

I would like to express my sincerest gratitude to my supervisor, Professor Christoph Janiak, who gave me the opportunity to join his research group at Heinrich Heine Universität Düsseldorf. Thank you for his guidance, encouragement and gracious supports throughout the course of my study, as well as the freedom and new challenges you gave me, so that I can learn and grow from it.

I also thank Professor Christian Ganter for being the co-supervisor.

I sincerely thank the China Scholarship Council (CSC) for providing me with a scholarship to complete my four-year Ph.D. in Germany.

My sincere thanks to Steffanie Bügel for her companionship, support, and understanding. Thank you for all your help during my stay in Germany.

I am grateful to Jun Liang for his great help in the research. His diligent work spirit is worthy of admiration.

I would like to thank Simon Millan for the warm welcome and care he gave me when I first came to the group.

I would like to thank Christian Jansen for discussing my first project with me.

I thank István Boldog for his efforts and kind guidance in my second project, and I respect his spirit of defending scientific research.

I would like to thank Alex Spieß for the scanning electron microscope measurements.

I would like to thank Alexander Nuhnen for the helpful discussion of my first project.

I thank Shanghua Xing for her kind help when encountering some learning problems.

Raphael Wiedey (Institut für Pharmazeutische Technologie & Biopharmazie) is thanked for cyclic water sorption measurements of the samples.

Dr. Sebastian-Johannes Ernst (Fraunhofer Institute for Solar Energy Systems, Freiburg) is thanked for the COP (coefficient of performance) calculation of the heat pump and the working principle scheme of an adsorption-based thermal battery (ATB).

Birgit Tommes is thanked for the FI-IR spectroscopy measurements and teaching me the use of the device.

Annette Ricken is thanked for the technical assistance and the atomic absorption spectroscopy (AAS) measurements.

Marcell Demandt is thanked for helping me with computer technical issues.

I express my gratitude to all the AC1 group members for their harmonious working atmosphere and helpfulness. I thank Carsten Schlüsener, Moritz Steinert, Li Wang, Daniel Komisarek, Dennis Woschko, Marcus Fetzer, Vasily Gvilava, Tobias Heinen, Dennis Woitassek, Simon-Patrick Höfert, Olga Koikolainen, Ülkü Kökçam-Demir, Saskia Menzel, Robert Oestreich, Secil Öztürk, Dietrich Püschel, Lars Rademacher, Linda Sondermann, Irina Gruber, Maximilian Klopotowski, Ilka Simon, Niels Tannert, Dr. Anna Goldman, Dr. Philipp Brandt, Dr. Serkan Gökpinar, Dr. Emrah Hastürk, Dr. Alexa Schmitz, Dr. Tobie Matemb Ma Ntep, Dr. Bastian Moll, Dr. Beatriz Giesen, Dr. Sandra Nießing, Dr. Dennis DietrichDr. José Moya-Cancino, Dr. Bahareh Nateghi, Dr. Laura Schmolke, Dr. Marvin Siebels, Dr. Nader de Souza Amadeu, Dr. Vera Vasylyeva-Shor, Dr Mahsa Armaghan, Abdulrahman Mohabbat, Malte Hähnel, Marylin Kaul, Janis Wiebe, Fabian Zajusch. I have spent an unforgettable time among you over the past four years and have left lasting memories.

Last and most importantly, I am very grateful to my family, my Fiancé, and my friends, who are always there for me, giving me timely encouragement and support. I appreciate much their concern and understanding during these years. I also want to thank myself for my growth and continuous efforts.

## Publication lists

1 Tunable LiCl@UiO-66 composites for water sorption-based heat transformation applications.

**Yangyang Sun**, Alex Spieß, Christian Jansen, Alexander Nuhnen, Serkan Gökpinar, Raphael Wiedey, Sebastian-Johannes Ernst and Christoph Janiak*, *J. Mater. Chem. A*, 2020, **8**, 13364-13375. DOI: 10.1039/d0ta03442h.

2 Cucurbit[6]uril@MIL-101-Cl: loading polar porous cages in mesoporous stable host for enhanced $SO_2$ adsorption at low pressures.

**Yangyang Sun**, Jun Liang, Philipp Brandt, Alex Spieß, Secil Öztürk and Christoph Janiak*, *Nanoscale*, 2021. DOI: 10.1039/D1NR04432,

3 A chemically stable hydrogen-bonded organic framework for $SO_2/CO_2$.

Jun Liang, Shanghua Xing, Philipp Brandt, Alexander Nuhnen, Carsten Schlüsener, **Yangyang Sun** and Christoph Janiak*, *J. Mater. Chem. A*, 2020, **8**, 19799-19804. DOI: 10.1039/d0ta07457h.

4 A Series of new Urea-MOFs Obtained via Post-synthetic Modification of $NH_2$-MIL-101(Cr): $SO_2$, $CO_2$ and $H_2O$ Sorption.

Tannert, Niels, **Sun, Yangyang**, Hastürk, Emrah, Nießing, Sandra, Janiak, Christoph*, *Z. Anorg. Allg. Chem.*, 2021, **647**, 1124-1130. DOI: 10.1002/zaac.202100023

5 Cucurbituril–Encapsulating Metal–Organic Framework via Mechanochemistry: Adsorbents with Enhanced Performance.

Jun Liang, Vasily Gvilava, Christian Jansen, Secil Öztürk, Alex Spieß, Jingxiang Lin, Shanghua Xing, **Yangyang Sun**, Hao Wang, and Christoph Janiak*, *Angew. Chem. Int. Ed.* 2021, 60, 15365-15370. DOI: 10.1002/anie.202100675.

6 Binary and ternary covalent triazine framework/ionic liquid/Matrimid® mixed-matrix membranes for $CO_2/CH_4$ separation.

Stefanie Bügel; Quang-Dien Hoang; Alex Spieß; **Yangyang Sun**; Shanghua Xing and Christoph Janiak*

# Zusammenfassung

Diese Arbeit untersucht Komposite von Metallorganischen Gerüstverbindungen (engl. *Metal-Organic Frameworks*, MOFs) durch die Einführung funktioneller Materialien in die Poren des MOFs, um die Adsorptionseigenschaften zu verbessern. In dieser Arbeit wurden MOF-basierte Kompositverbindungen für Anwendungen in der Adsorptionswärmetransformation (engl. *Adsorption Heat Transformation*, AHT) (Abschnitt 3.1) oder der Schwefeldioxidadsorption (Abschnitt 3.2) untersucht.

In Abschnitt 3.1 wurde LiCl@UiO-66 als Kompositsalz in poröser Matrix erfolgreich synthetisiert, indem hygroskopisches Lithiumchlorid in das mikroporöses MOF UiO-66 als Wirtsmatrix durch die Nassimprägnierungsmethode eingebaut wurde. Die Komposite weisen die folgenden Eigenschaften auf: (i) Im Vergleich zum Ausgangsmaterial UiO-66 erhöht LiCl die Wasseradsorptionskapazität stark. UiO-66 mit einem Gehalt von 30 Gew.-% LiCl hat eine achtmal höhere Wasseraufnahme als das ursprüngliche UiO-66 bei $p\ p_0^{-1}$ = 0,1. Darüber hinaus zeigen (ii) die Wasserdampf-Isothermen einen Hydratationszustand von LiCl innerhalb des MOF von LiCl·2–4$H_2O$ in den drei Kompositen (LiCl@UiO-66_19, LiCl@UiO-66_29, LiCl@UiO-66_30), der viel höher ist als für reines LiCl mit 0,5 $H_2O$ bei $p\ p_0^{-1}$ = 0,1, wahrscheinlich aufgrund der Dispersion von kleinen LiCl-Clustern mit ihrer hohen Oberflächenenergie in der porösen Matrix. (iii) Die kinetische Analyse der Wasseraufnahme in gravimetrischen Messungen über die Zeit zeigt, dass die erwartete Adsorption in LiCl@UiO-66 langsamer ist als die in reinem UiO-66 aufgrund von Porenblockierungseffekten. (iv) Die hohe Wasseradsorptionskapazität (271 mg $g^{-1}$) bei $p{\cdot}p_0^{-1}$ = 0,1 von LiCl@UiO-66_30 fällt mit einer hohen thermischen Speicherkapazität (900 kJ $kg^{-1}$, 0,25 kWh $kg^{-1}$) zusammen, was dieses wasserstabile Komposit für thermische Batterieanwendungen geeignet macht. (v) Die Leistungszahl (engl. *Coefficient of performance*, COP) für den Wärmepumpenmodus (bei $T_{des}/T_{ads}/T_{evap}$ =

90/40/10 °C) für LiCl@UiO-66_30 beträgt 1,64 und übertrifft damit die meisten der anderen MOF-, Salz@MOF- oder Salz@Kieselgel-Komposite.

In Abschnitt 3.2 wurde das Cucurbituril-MOF-Komposit CB6@MIL-101-Cl synthetisiert, durch Einlagerung der Cucurbit[6]uril-Moleküle in die großen Poren des MIL-101 zusammen mit einem OH-zu-Cl-Ligandenaustausch. CB6@MIL-101-Cl kombiniert die starke $SO_2$-Affinität der starren CB6-Makrozyklen und die hohe $SO_2$-Aufnahme von MIL-101, daher zeigt es eine hervorragende $SO_2$-Aufnahme von 438 $cm^3\ g^{-1}$ (19.5 mmol $g^{-1}$) bei 1 bar und 293 K. Die Menge an $SO_2$, die von CB6@MIL-101-Cl bei 0,01 bar und 293 K aufgenommen wurde, betrug 2,1 mmol $g^{-1}$, was dreimal höher ist als die des Ausgangsmaterials MIL-101 (0,7 mmol $g^{-1}$) unter den gleichen Bedingungen. Die $SO_2$-Adsorptionsenthalpie bei nahezu Nullbedeckung von CB6@MIL-101-Cl beträgt 50 kJ $mol^{-1}$, höher als die 35 kJ $mol^{-1}$ von MIL-101. Es spiegelt den Einfluss der eingebauten CB6-Makrocyclen wider, die eine höhere Affinität zu $SO_2$ aufweisen. Die Wechselwirkungen zwischen $SO_2$ und den Cucurbit[6]uril-Anteilen des CB6@MIL-101-Cl wurde durch Fourier-Transformations-Infrarotspektroskopie (FTIR) verifiziert.

MIL-101 erwies sich als instabil gegenüber trockenem $SO_2$ durch den Verlust von Kristallinität und Porosität nach der $SO_2$-Adsorption wie Pulver-Röntgendiffraktometrie (PXRD) und $N_2$-Adsorptions-Desorptionsmessung zeigten. Im Vergleich zu MIL-101 wurde die Stabilität durch einen unerwarteten Austausch von Hydroxid-zu-Chlorid im $\{Cr_3(O)X(BDC)_3\}$-Metallknoten von MIL-101 zu CB6@MIL-101-Cl verbessert. Energiedispersive Röntgenspektroskopie (EDX) und Röntgenphotoelektronenspektroskopie (XPS) Analysen unterstützten das Vorhandensein des OH-zu-Cl-Ligandenaustauschs. Zyklische $SO_2$-Adsorptions-Desorptions-Messungen bestätigten die Stabilität von CB6@MIL-101-Cl über 10 Zyklen. Nach der Behandlung mit feuchtem $SO_2$ verringerte sich die $SO_2$-Aufnahmekapazität von nanoCB6-H aufgrund der geringeren Porosität. Für

MIL-101 und CB6@MIL-101-Cl verringerte sich die Aufnahmekapazität bei 1 bar und 293 K jeweils um ca. 20 % im Vergleich zu ihrem jeweiligen Verhalten unter trockenen Bedingungen, jedoch zeigte sich bei 0,01 bar eine bessere Adsorptionsleistung für CB6@MIL-101-Cl als für MIL-101. CB6@MIL-101-Cl ist daher aufgrund seiner ausgezeichneten Zyklenstabilität, hohen Kapazität und starken Affinität für $SO_2$ bei niedrigen Drücken ein attraktives Sorptionsmittel für die $SO_2$-Abtrennung.

## Summary

This work investigates composites of Metal-Organic Frameworks (MOFs) via the introduction of functional materials into the pores of the MOF, in order to improve the adsorption properties and to better suit certain practical applications. In this thesis, we have synthesized different MOF-based composites compounds for Adsorption Heat Transformation (AHT) applications (section 3.1) and sulfur dioxide adsorption applications (section 3.2), respectively.

In section 3.1, LiCl@UiO-66 as a 'composite salt inside porous matrix' (CSPM) was successfully synthesized via incorporating hygroscopic lithium chloride into microporous UiO-66 (University of Oslo) as the host matrix through the wet impregnation method. The composites exhibit the following advantages: (i) Compared to the parent UiO-66, the LiCl@UiO-66 composite features a strongly enhanced water adsorption capacity. UiO-66 with a 30 wt% content has an 8 times higher water uptake over the parent UiO-66 at $p\,p_0^{-1} = 0.1$. In addition, (ii) the water vapor isotherms show a hydration state of LiCl inside of the MOF of LiCl·2–4$H_2O$ in the three composites (LiCl@UiO-66_19, LiCl@UiO-66_29, LiCl@UiO-66_30), which is much higher than for bulk LiCl with 0.5 $H_2O$ at $p\,p_0^{-1} = 0.1$, due to the dispersion of small LiCl clusters with their high surface energy in the porous matrix. (iii) Kinetic analysis of water uptake in gravimetric measurements over time shows that the expected adsorption in LiCl@UiO-66 is slower than that in pure UiO-66 due to pore blocking effects. (iv) The high-water adsorption capacity (271 mg $g^{-1}$) at $p{\cdot}p_0^{-1} = 0.1$ of LiCl@UiO-66_30 coincides with a high thermal storage capacity (900 kJ $kg^{-1}$, 0.25 kWh $kg^{-1}$), which makes this water-stable composite suitable for thermal battery applications. (v) The coefficient of performance (COP) for the heat pump mode (at $T_{des}/T_{ads}/T_{evap}$ = 90/40/10 °C) for LiCl@UiO-66_30 is 1.64, which outperforms most of the other MOF, salt@MOF or salt@silica gel composites.

In section 3.2, the cucurbituril-MOF composite CB6@MIL-101-Cl was synthesized by incorporating cucurbit[6]uril molecules into the large cages of the MIL-101 together with a concomitant OH-to-Cl ligand exchange. CB6@MIL-101-Cl combines the strong $SO_2$ affinity of the rigid CB6 macrocycles and the high $SO_2$ uptake of MIL-101, thus it shows an excellent $SO_2$ uptake of 438 $cm^3 \cdot g^{-1}$ (19.5 mmol $g^{-1}$) at 1 bar and 293 K. The amount of $SO_2$ captured by CB6@MIL-101-Cl at 0.01 bar and 293 K is 2.1 mmol $g^{-1}$, which is three times higher than that of the parent MIL-101 (0.7 mmol $g^{-1}$) under the same conditions. The $SO_2$ adsorption enthalpy of CB6@MIL-101-Cl near zero-coverage is 50 kJ $mol^{-1}$, which is higher than 35 kJ $mol^{-1}$ of MIL-101. It reflects the influence of the incorporated CB6 macrocycles which have a higher affinity towards $SO_2$. The interactions between $SO_2$ and the cucurbit[6]uril moieties of the CB6@MIL-101-Cl were verified by Fourier-transform infrared spectroscopy (FTIR).

MIL-101 was shown to be unstable to dry $SO_2$ due to the loss of crystallinity and porosity of MIL-101 after $SO_2$ adsorption, as evidenced by powder X-ray diffraction (PXRD) and $N_2$ adsorption-desorption measurement. Compared to MIL-101, the stability of CB6@MIL-101-Cl was improved, which may be due to the unexpected exchange of hydroxido-to-chlorido in the $\{Cr_3(O)X(BDC)_3\}$ metal node of MIL-101. Energy-dispersive X-ray spectroscopy (EDX) and X-ray photoelectron spectroscopy (XPS) analysis supported the existence of the OH-to-Cl ligand exchange. Cyclic $SO_2$ adsorption-desorption measurements further confirmed that CB6@MIL-101-Cl was stable over 10 cycles. After exposure to humid $SO_2$, the $SO_2$ uptake capacity of nanoCB6-H decreased due to its decreased porosity. For MIL-101 and CB6@MIL-101-Cl, the uptake capacity at 1 bar and 293 K both decreased around 20% compared to their respective behavior under dry conditions, however, at 0.01 bar CB6@MIL-101-Cl exhibited a better adsorption performance uptake than MIL-101. CB6@MIL-101-Cl is therefore an attractive sorbent for $SO_2$ capture due to its excellent cycling stability, high capacity and strong affinity for $SO_2$ at low pressures.

## List of abbreviations

| | |
|---|---|
| AHT | Adsorptive Heat Transformation |
| ATB | Adsorption Thermal Battery |
| AHP | Adsorption Heat Pump |
| COP | Coefficient of Performance |
| EDX | Energy Dispersive X-ray spectroscopy |
| XPS | X-ray Photoelectron Spectroscopy |
| AAS | Atomic Absorption Spectroscopy |
| TGA | Thermogravimetric Analysis |
| PXRD | Powder X-ray Diffraction |
| SEM | Scanning Electron Microscopy |
| BET | Brunauer–Emmett–Teller |
| PSD | Pore Size Distribution |
| NLDFT | Non-Local Density Functional Theory |
| MOF | Metal-Organic Framework |
| TDC | Thermally Driven Chiller |
| UiO | Universitetet i Oslo/ University of Oslo |
| MIL | Materials of Institute Lavoisier |
| HKUST-1 | Hong Kong University of Science and Technology |
| ICP-OES | Inductively Coupled Plasma-Optical Emission Spectrometer |
| FTIR | Fourier-transform Infrared spectroscopy |
| ATR | Attenuated Total Reflection |
| ESI–MS | Electrospray Ionization–Mass Spectrometry |
| AWH | Atmospheric Water Harvesting |
| DOE | Department of Energy |
| $\Delta H_{ads}$ | Isosteric enthalpy of adsorption |
| $Q_{evp}/Q_{ads}/Q_{cond}/Q_{des}$ | Heat of evaporation/adsorption/condensation/desorption |
| Å | Ångström or Angstrom (1 Å = $10^{-10}$ m) |
| CUS | Coordinatively unsaturated metal sites |
| EA | Elemental Analysis |
| DMSO | Dimethyl Sulfoxide |

| | |
|---|---|
| IUPAC | International Union of Pure and Applied Chemistry |
| NMR | Nuclear magnetic resonance |
| IAST | Ideal Adsorbed Solution Theory |
| FGD | Flue Gas Desulfurization |
| TFA | Trifluoroacetate |
| RH | Relative Humidity |
| THF | Tetrahydrofuran |
| MeOH | Methanol |
| EtOH | Ethanol |
| PCNs | Porous Coordination Networks |
| DMF | *N,N*-dimethylformamide |
| DEF | *N,N*-diethylformamide |
| DMA | *N,N* dimethylacetamide |
| TCPP | tetrakis(4-carboxyphenyl)porphyrin |
| $CDCl_3$ | Deuterated chloroform |
| SBUs | Secondary building units |
| CSD | the Cambridge Structural Database |
| POMs | Polyoxometallates |
| $H_2BDC$ | Benzene-1,4-dicarboxylic acid |
| $H_2BPDC$ | 4,4′-biphenyl dicarboxylic acid |
| $H_2TPDC$ | *p*-terphenyl-4,4′-dicarboxylic acid |
| PTFE | Polytetrafluoroethylene |
| SALI | Solvent Assisted Ligand Incorporation |
| wt% | Weight percentage |

**Table of Contents**

# 1 Introduction

This introduction covers the research of the metal-organic framework (MOF)-based composite materials in two applications: adsorption heat transformation and sulfur dioxide adsorption. The introductory section consists of the following parts: The overview of porous metal-organic framework materials and some prototypical MOF structures will be presented (Section 1.1); Functionalization of MOF will be introduced (Section 1.2); MOF-based composites and their synthesis method will be described (Section 1.3); The potential applications of MOFs will be introduced, including adsorption-based heat transformation and sulfur dioxide adsorption (Section 1.4).

## 1.1 Metal-Organic Frameworks

Metal-organic frameworks (MOFs) are organic-inorganic hybrid solids with an infinite, uniform framework structure built from inorganic metal ions or metal-containing cluster nodes and organic ligands. It possesses the features of zero-, one-, two-, or three-dimensional framework structures via coordinative metal-ligand interactions (Figure 1).[1] MOFs possess the features of large surface area, high porosity, highly tunable pore size/shape and surface functionality. Owing to these unique features, MOFs have been of great interest and importance in various potential applications, such as gas storage (hydrogen/methane),[2,3] gas adsorption and separation.[4,5] Alongside this outstanding interest in gas uptake, other applications include heterogeneous catalysis,[6] chemical sensing,[7] proton conduction[8], luminescence[9] and biotechnology.[10]

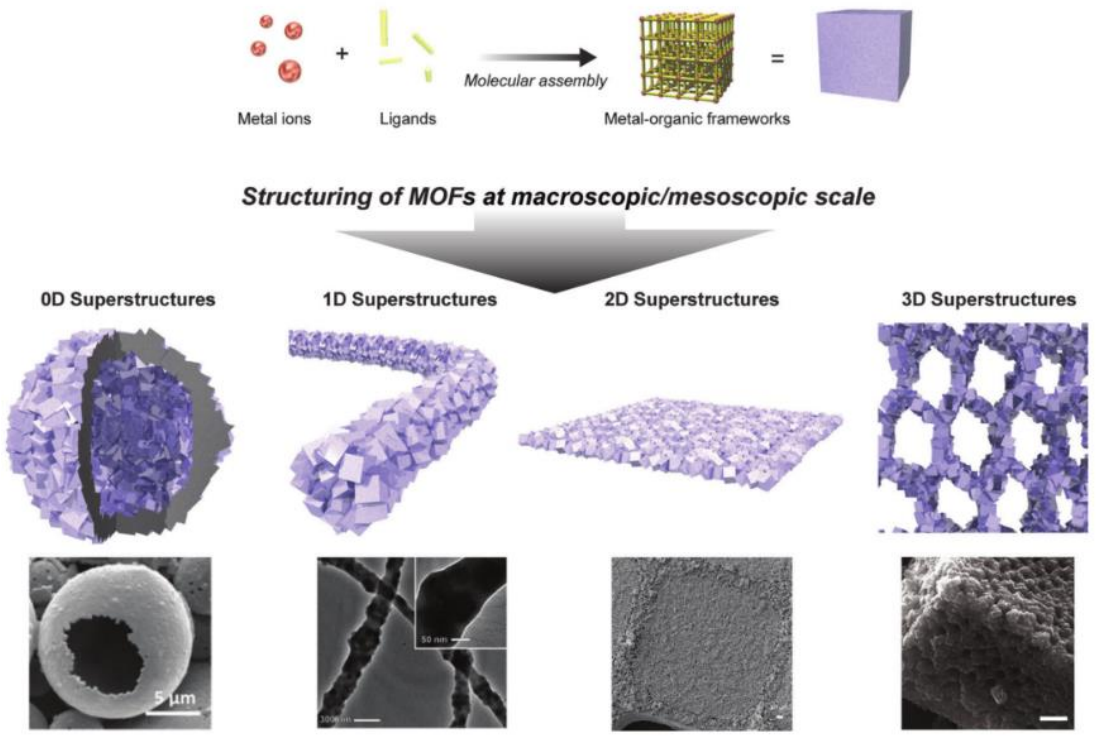


**Figure 1** Conceptual diagram of MOFs at the micro/meso scales. Four different dimensionalities as presented: zero-dimensional (0D) structure, one-dimensional (1D) structures, two-dimensional (2D) structures, and three-dimensional (3D) structures. Reproduced with permission form ref 1. Copyright 2014 Royal Society of Chemistry

### 1.1.1 Some prototypical MOFs

In the 1990s, two milestone MOFs emerged, MOF-5 ($[Zn_4O(BDC)_3]$, BDC = 1,4-benzenedicarboxylate) [11] and HKUST-1 ($[Cu_3(BTC)_2(H_2O)_3]$, BTC = 1,3,5-benzenedicarboxylate)[12] with their prominent robust porosity. These findings prompted the development of other novel porous materials. Shortly afterward, in 2005 Férey *et al.* reported a representative MOF with high chemical and thermal stability, MIL-101 ($[Cr_3(\mu_3\text{-}O)X(H_2O)_2(BDC)_3]$, X = F, OH)[13]. In 2008, Cavka *et al.* discovered another new type of MOF, UiO-66 $[Zr_6(\mu_3\text{-}O)_4(\mu_3\text{-}OH)_4(BDC)_6]$[14]. The rapid development of the field during these two decades has been driven largely by the observation of the various exciting properties and promising applications of these porous solid materials.

MOF-5 is also termed IR-MOF-1. It is a three-dimensional cubic porous framework with $[Zn_4O]^{6+}$ clusters linked together through 1,4-benzenedicarboxylate ($BDC^{2-}$) ligands.[11] It is thermally stable up to 300 °C but is unstable to water.[11, 15] Water molecules can dissociate the structure of MOF-5, thereby destroying the relatively weak metal-ligand interactions in MOF-5. IR-MOF-n (n = 1–16)[16] is a series of cubic isoreticular MOF structures built from the same secondary building unit (SBU) [$Zn_4O(-COO)_6$] and various linear dicarboxylate linkers (Figure 2). IR-MOF-n crystalline materials possess up to 91% void space of the unit cell volume in the solvent-guest free state, large tunable pore sizes ranging from 3.8 to 28.8 Å, and specific pore volumes up to 1 $cm^3\ g^{-1}$.[16] Of these, IR-MOF-16 has a record-high porosity of 91% of the unit-cell volume in the solvent-guest free state.

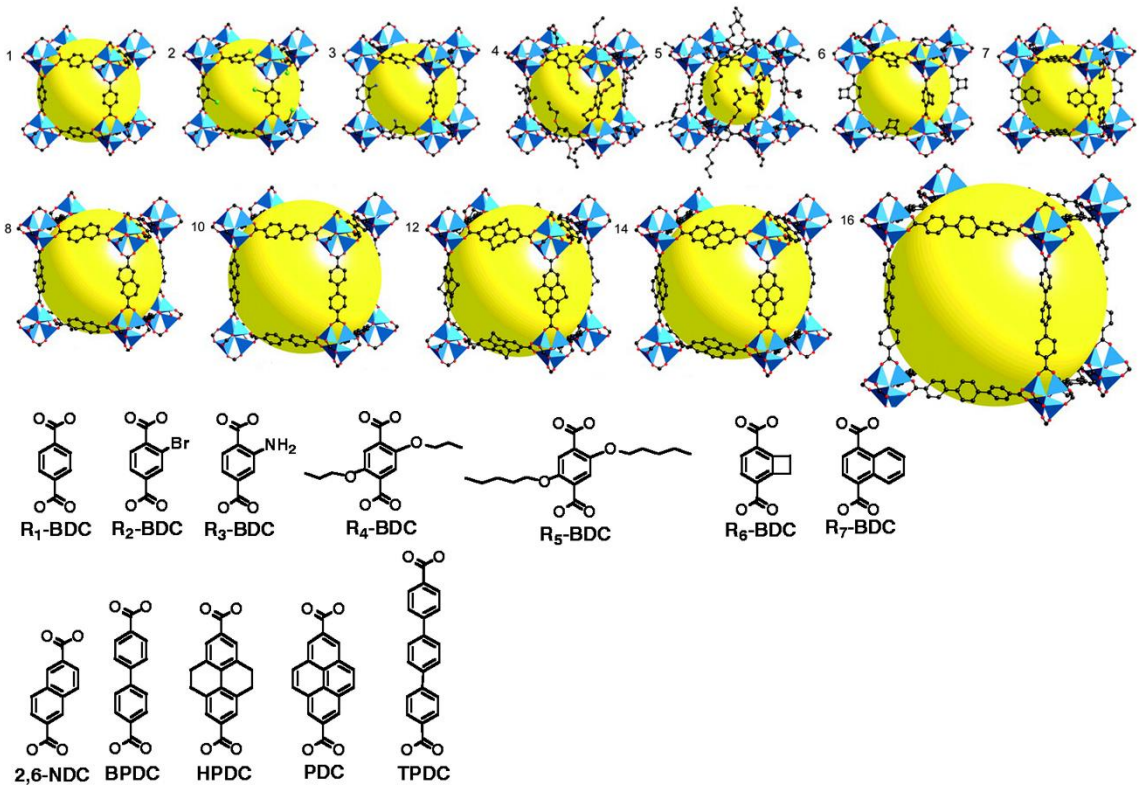


**Figure 2** A series of isoreticular MOFs and central spheres represent open pore spaces such as those shown (MOF-5, CSD-Refcodes SAHYIK, SAHYOQ, and EDUSIF). The different objects in this figure are not drawn to scale. Reproduced with permission form Ref 16 Copyright 2002 American Association for the Advancement of Science.

HKUST-1 is a three-dimensional copper-trimesate compound that is well investigated in crystal structure and surface area,[17,18,19] as well as water vapor uptake.[20,21,22,23] HKUST-1 consists of square $Cu_2$ paddlewheel clusters coordinated with four independent BTC linkers (Figure 3).[24] It has a rigid porous framework with a face-centered-cubic (fcu) topology, and large square-shaped pores (9 Å × 9 Å). The framework of HKUST-1 is stable up to 240 °C.[25] It features bimodal pore size distributions and it is one of the most studied MOFs with unsaturated metal sites (open metal site).[26] It has a high-water vapor uptake of 32 mmol $g^{-1}$ at 298 K and 90 % relative humidity (RH).[27] The crystalline structure of HKUST-1 will suffer an irreversible degradation when exposed to water in a liquid or vapor form in a long term, due to the very strong interactions between open Cu (II) sites from the copper paddlewheel and water molecules.[28]

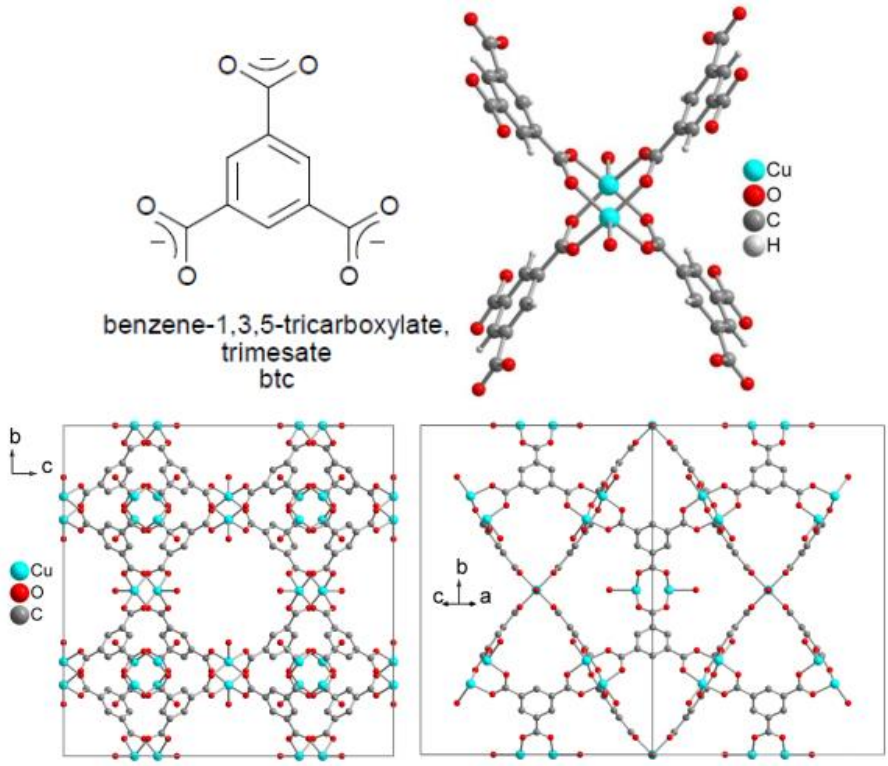


**Figure 3.** The structural components of trimesate and $\{Cu_2(COO)_4\}$ building unit in HKUST-1 (top) and two directions of the packing mode (bottom). (CSD-Refcode FIQCEN). The different objects in this figure are not drawn to scale. Reproduced with permission form Ref 24. Copyright 2010 Royal Society of Chemistry.

UiO-66 (University of Olso) is the progenitor of a family of zirconium-based MOFs, and it is made up of $[Zr_6O_4(OH)_4]$ clusters with 1,4-benzenedicarboxylate ($BDC^{2-}$), forming a fcu topology (Figure 4).[29] The microporous UiO-66 features octahedral and tetrahedral cages, with the diameter of 11 Å and 8 Å, respectively.[30] Based on the same SBU $\{Zr_6O_4(OH)_4(COO)_{12}\}$, UiO-67 and UiO-68 with the same topology were synthesized via the extended number of benzene rings, 4,4′-biphenyl dicarboxylic acid ($H_2BPDC$) and *p*-terphenyl-4,4′-dicarboxylic acid ($H_2TPDC$). The stability of the framework is primarily controlled by the inorganic unit and the strength of the chemical bond between the inorganic unit and the linker. Group four elements have a strong interaction with oxygen, and therefore they are considered to be stable inorganic cornerstones. In addition, UiO-66 and UiO-67 have the same decomposition temperature ($T_{decomp}$ = 540 °C), due to the weakest bond between the benzene rings and the terminal carboxyl group instead of the connection between the inorganic brick and the linker or the inorganic brick itself.[14]

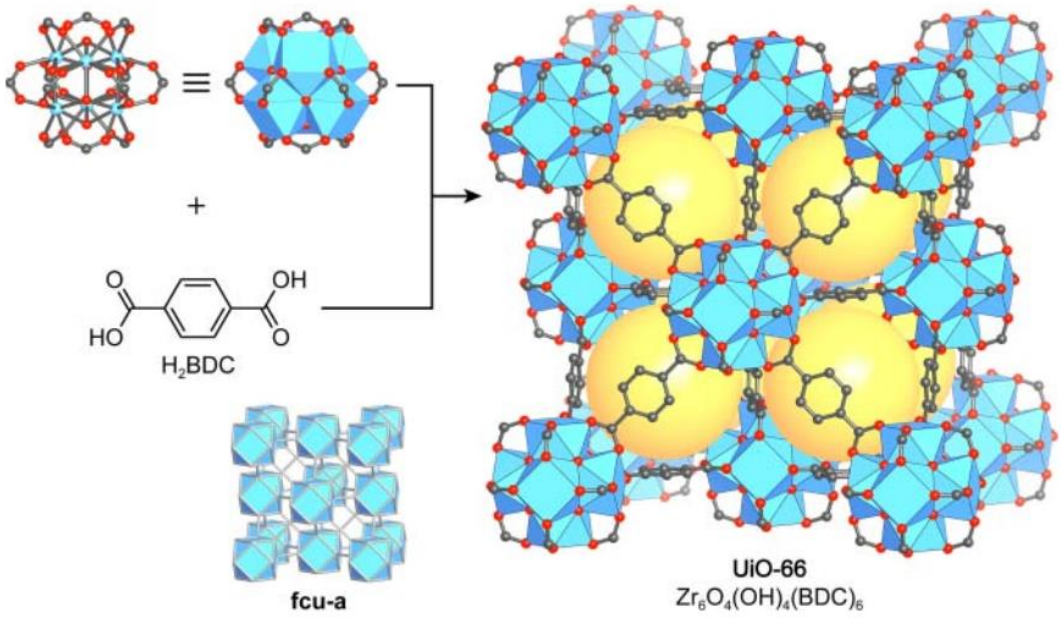


**Figure 4** Crystal structure and fcu topology of UiO-66 MOFs. All hydrogen atoms are omitted for clarity. Color code: Zr, blue; C, gray; O,red. The orange spheres indicate the largest pores in the tetrahedral cages. (CSD-Refcodes RUBTAK). Adapted with permission from ref 29. Copyright 2019 Jonh Wiley and Sons.

The MIL-n series (Materials Institute Lavoisier) originated from the Férey group. The metal is found to be some transition metals, such as trivalent cations, such as chromium(III),[31] iron(III)[32,33] and vanadium(III), Titanium(IV)[34] and p-elements, for instance, aluminum(III),[35] gallium(III) or indium(III).

MIL-101 is one of the MIL-n series structures with the outstanding properties of high porosity and hydrothermal stability. MIL-101 is stable over months under air atmosphere, even treated with organic solvents at high temperature or boiling water for a week.[36] The detailed structure of MIL-101(Cr) will be introduced in Chapter 2.

### 1.1.2 Synthesis and design of MOFs

Metal-organic frameworks are mostly synthetized via solvothermal/hydrothermal (water as reaction solvent) methods, where the initial mixture is often heated at temperatures less than 250 ℃. In general, metal sources, organic chemicals and the solvent are mixed, then in some case modulator is added to modulate the pH of the solution. After stirring for a period, the mixture is transferred to the autoclave with a PTFE inset or glass vessel for crystallization. Different MOFs can be generated even from the same reaction mixture, which is affected by many factors, such as temperature, pH, heating time and so on. Besides solvothermal methods,[26,37,38] other synthesis methods, such as electrochemical methods,[26] microwave-assisted heating, [39] mechanochemical[40,41] and sonochemical methods.[37,38] Different synthesis methods may have a significant effect on yield, particle size, morphology or the possibility of large-scale implementation.

The design and synthesis of MOF similar to conventional zeolites with various topologies has been well described and summarized.[42] A wide variety of MOF structures can be obtained through the ideal choice of metal ions and linkers of different sizes and shapes. Moreover, a great number of MOFs with different compositions and porosity originated from the various building units and connection modes. Some

common SBUs are shown in Figure 5.[43] Furthermore, the pore size of the MOF structure can also be modulated by the length of various organic ligands (biphenyl, tetrahydropyrene, pyrene, and terphenyl).[44]

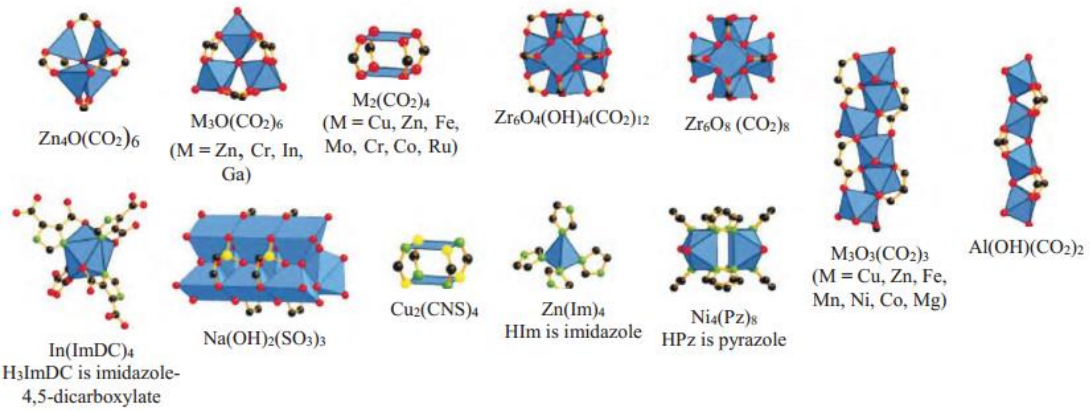


**Figure 5** Some inorganic SBU examples. Reproduced from ref 43. Copyright 2013 American Association for the Advancement of Science.

### 1.1.3 Hydrolytic stability of MOFs

Some benchmark MOFs like HKUST-1 (copper trimesate) and MOF-5 (Zinc terephthalate) are not water stable. The weak coordinative bonds between metal nodes and linker molecules can be attacked by nucleophilic $H_2O$, resulting in the degradation of the framework structure and the loss of porosity.[45,15]

In the presence of water, the degradation of MOFs usually occurs through either hydrolysis or linker replacement.[46] In the case of hydrolysis, the metal-organic bond is broken while metal-hydroxide and the conjugated acid of the ligand (neutral) are formed (eqn 1). During ligand replacement, the water molecules are inserted into the metal-linker bond, leading to the formation of a hydrated SBU and a deprotonated linker (eq 2).

$$M–L + H_2O \rightarrow M–(OH) + HL \qquad \text{eqn 1}$$

$$M–L + H_2O \rightarrow M–(OH_2) + L \qquad \text{eqn 2}$$

The thermodynamic and kinetic factors that affect the hydrolytic stability of MOFs are listed in Table 1. According to Lewis acid–base chemistry, the higher the p$K_a$ of the protonated linker, the stronger the metal–linker bond. Compared to carboxylate-based linkers (e.g., benzenedicarboxylic acid and benzenetricarboxylic aicd, p$K_a$ ≈ 4), imidazolate or pyrazolate-based linkers have stronger bonding to the metal component of the framework (e.g., imidazole, p$K_a$ ≈ 14.5; pyrazole, p$K_a$ ≈ 19.8).[47,48,49] This makes metal-nitrogen bonds thermodynamically more stable than metal-oxygen bonds in carboxylate-based MOFs.

Moreover, the higher the charge of the metal and the smaller the ionic radius, the stronger the acidity and therefore the stronger the bond between the metal and the organic ligand. Thus, MOFs incorporated with trivalent metal ions seem to be more stable than bivalent metal ions,[46,50] while high stability is attributed to tetravalent Zr/Hf.[14,50,51]

In addition, metal ions with 6-fold coordination are often more stable than the corresponding 4-fold coordination metal ions, because the dense packing of coordination spheres makes the coordination of water and metal ions more difficult.[52]

The steric hindrance can be achieved by the high coordination number,[53] bulky linkers[54] or interpenetration of the framework. Note that although these factors are discussed separately, in practice they cannot always be completely separated (Table 1).

**Table 1** The effect of the thermodynamic and kinetic factors on the stability of MOFs in the presence of water.

| Thermodynamic stability/instability | Kinetic inertness/lability |
|---|---|
| • p$K_a$ of the linker (basicity)<br>• Oxidation state and ionic radius of the metal (acidity)<br>• Reduction potential of the metal<br>• Coordination geometry | • Steric hindrance (i.e. "coordination number") and rigidity of the constituents<br>• Steric hindrance through interpenetration<br>• Hydrophobicity<br>• Electronic configuration of the metal ions |

## 1.2 Functionalization of MOFs

The functionalization of MOF can finely adjust the structure and property of MOFs, thus improving the performance in practical applications and broadening the application range of this material. The functionalization of MOF is mainly divided into the following three categories: in-situ, pre-synthetic, and post-synthetic modification. The post-synthetic modification are divided into weak, strong, and covalent modifications according to the strength of the interaction (Figure 6).[55]

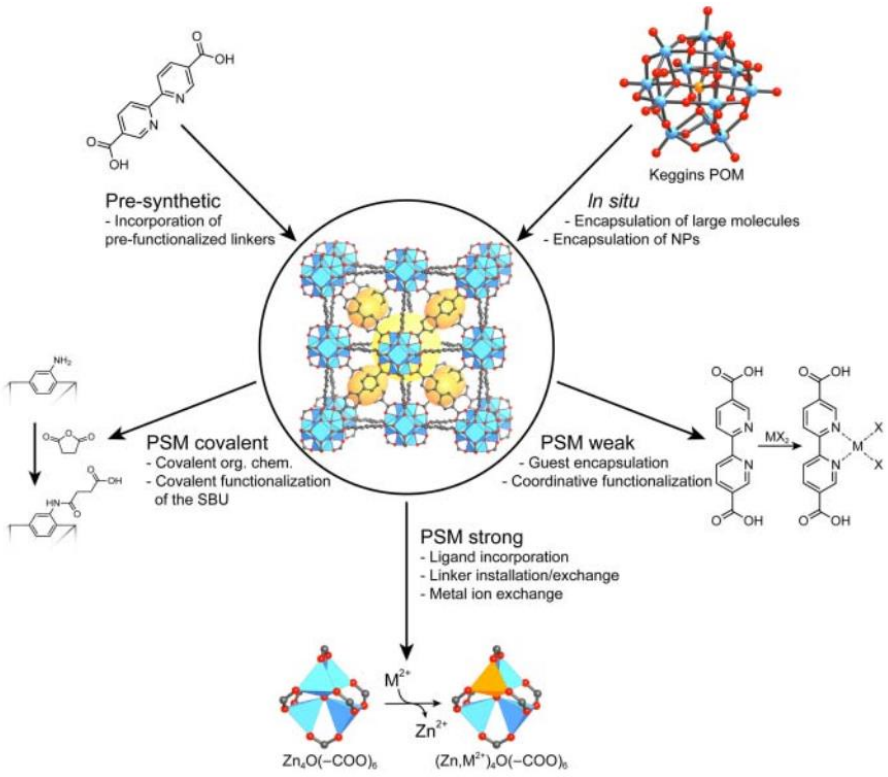


**Figure 6** Possibilities of chemical functionalization of MOFs. Adapted with permission from ref 55. Copyright 2019 Jonh Wiley and Sons.

### 1.2.1 In situ functionalization

In the MOF synthesis, guest molecules are introduced into the structure of MOF, this approach is termed *in situ* functionalization. This type of functionalization needs to meet either of these two prerequisites: a) the kinetic diameter of the guest moieties is bigger than the pore aperture, or b) binding sites exist within the pores between the

framework structure and guest molecules. For example, large inorganic molecules polyoxometalates (POMs) with a catalytic function were encapsulated in the pores of MIL-101 during the framework formation.[56, 57] This approach can be used to immobilize a wide variety of target molecules in porous MOF matrices that confer specific functionality.

### 1.2.2 Pre-synthetic functionalization.

Prior to the synthesis of MOFs, the organic linker can be modified. However, this method, termed pre-synthetic functionalization, has many limitations. It is necessary to consider the compatibility of the modified organic ligand with the MOF synthesis conditions. Importantly, the modified part cannot affect the formation of the desired MOF. A representative and successful example is the synthesis of MIL-125($NH_2$) using $NH_2$-BDC instead of $H_2$BDC linker.[58] MIL-125($NH_2$) exhibited different properties in UV absorption. In contrast to the absorption in the UV region of MIL-125, MIL-125($NH_2$) demonstrated a second absorption band in the visible region due to the electron-donating nature of the $-NH_2$ group.[58,59]

### 1.2.3 Post-synthesis modification

Post-synthetic modification (PSM) of MOFs allows for a deliberate functionalization, such as the position and the degree under the premise of retaining the crystallinity, original structure framework. It is also a complementary tool for the pre-synthetic modification. As for PSM of MOFs, three approaches are mostly applied according to the interaction strength between the framework and the additional unit:

a) via weak interactions (encapsulation of guests,[60] coordinative functionalization of open metal site[61] or coordinative functionalization of the linker[62])

b) via strong interactions (solvent assisted ligand incorporation,[63, 64] post-synthetic linker exchange[65] or post-synthetic linker installation[66])

c) via covalent interactions (e.g. covalent bond via amino-functionalized MOFs[67])

For guest encapsulation approach, the size of the guest molecule is limited by the pore opening of the host framework. The molecule is bound to the framework by weak interactions. The potential problem is leaching phenomenon due to the absence of spatial confinement.[60] Other types with weak interactions also include post-grafting of coordinated unsaturated metal site (CUS) with chelating agents or electron-rich molecules via coordinative bond.[61]

For solvent assisted ligand incorporation (SALI) technique, a functional group is introduced as charge compensation, and is firmly bound to the metal cluster. In general, solvent-assisted ligand exchange is achieved by immersing a MOF in a concentrated solution, and the terminal ligands such as –OH and $–OH_2$ are replaced by other Lewis basic charged molecules. For example, with the help of solvent-assisted ligand incorporation method, perfluoroalkane carboxylates was incorporated into Zr-based MOF NU-1000 (NU = Northwestern University) through the interactions with eight terminal –OH ligands (Figure 7).[63] Post-synthetic linker exchange is mostly used to extend the isoreticular structure while maintaining the framework topology. For instance, UiO-66 was soaked in a solution containing functionalized BDC derivatives to form a linker exchanged UiO-66 analogue.[65] In contrast, post-synthetic linker installation is used for the topological transformation, thus leading to changes in the physical, chemical, and mechanical properties of the MOF.[66] For example, MOF-520, $Al_8(OH)_8(HCOO)_4(BTB)_8$, was constructed from octametallic ring-shaped 12-c aluminum SBUs and trigonal tritopic BTB linkers, with a FON topology. The BPDC linker matches well the distance between adjacent SBUs, can be introduced as a new bridged linker, making the transition from FON into the SKL topology.[68]

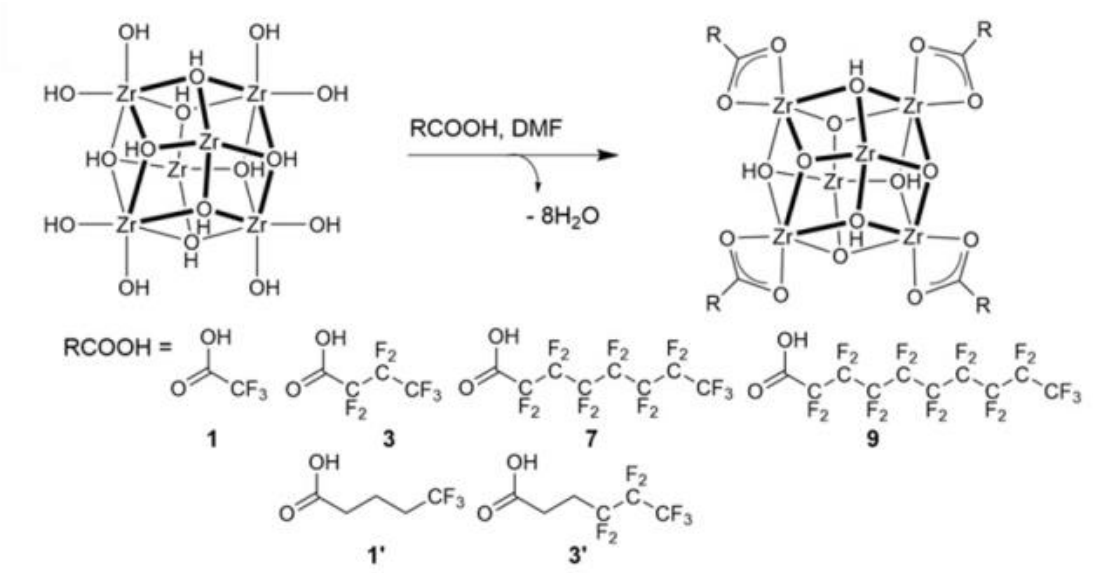


**Figure 7** Schematic representation of solvent-assisted ligand incorporation method. Perfluoroalkane carboxylates are attached to the 8-c zirconium SBUs in the structure of NU-1000. Reproduced from ref 63. Copyright 2013 American Chemical Society.

For the covalent interactions approach, it was mainly achieved via amide coupling reactions. For example, IRMOF-3 was constructed by $Zn_4O$ nodes bridged by $NH_2$–$H_2BDC$ linkers. The amino group ($–NH_2$) does not participate in the coordination to the metal nodes and has potential access to various organic reactions. IRMOF-3 was successfully acetylated through the covalent interactions of free amino groups with acetic.[67]

## 1.3 MOF-based composites

A lot of research efforts have been mainly aiming at preparing new MOF structures and exploring their various applications. However, MOF materials exhibit weaknesses such as poor chemical stability, low uptake in gas adsorption that impede the use of their full potential. In order to improve these problems, MOF-based composites composed of one MOF and one or more other functional materials have emerged, and have demonstrated the ability to combine the advantages of individual components and improve the weaknesses.[69]

Due to the large BET surface area, high porosity, and structural diversity and tunability, MOF is an ideal host platform for encapsulating other functional materials. The properties of MOF-based composites can be improved further for the greatly enhanced performance, stability or even novel properties in a specific application, compared to single-component materials. Until now, lots of examples of MOF composites have been successfully reported with different functional materials, including polyoxometalates (POMs), metal nanoparticles (NPs), carbon nanotubes (CNTs), oxides, quantum dots (QDs), polymers, ionic liquids (ILs), macrocyclic organic molecules, inorganic salts and so on, resulting in new properties that are superior to those of the individual component (Figure 8).[69,70,71]


**Figure 8** The composites of MOFs and functional materials. Reproduced from ref 69 Copyright 2014 Royal Society of Chemistry

### 1.3.1 Synthesis of MOF-based composites

Several methods and approaches have been applied for the preparation of MOF-based composites.[72] Here we focus on the approach of "ship-in-a-bottle", which realizes the encapsulation of the functional materials into the pores of the prefabricated MOF. In this case, the MOF (bottle) is prefabricated, and the functional material or its precursor is dissolved in a solvent, and the diffusion of the precursor is carried out inside the cages of the preformed MOF by a solvent system, then the formation of functional materials (ship) occurs inside of the cages. The particles of the functional materials stay stable

inside the pores of the MOFs, probably due to the particle size being larger than the pore apertures of the MOF,[73] or by means of chemical or thermal methods. This "ship-in-a-bottle" approach can be achieved using various techniques such as wet impregnation, solvent-free solid grinding, and chemical vapor deposition (CVD).

One of the most extensive post-synthesis impregnation methods is wet impregnation. In this method, the solvent volume exceeds the pore volume of the MOF material. The functional material such as inorganic salts, organic macrocyclic molecules, or the precursors of the functional material such as ILs, NPs are first dissolved and well dispersed in a solvent, the desolvated MOF is then added to the solution. The target product is obtained from the solvent through solvent evaporation or centrifugation, and in some cases, a washing process is needed, to remove the functional materials adhering to the outside surface of MOF particles. Through this strategy, many examples of IL/MOF,[74,75,76] NP/MOF[77] or inorganic salt/MOF[78,79] composite materials have been successfully reported and used in adsorption or catalytic applications.

Another technique is solvent-free solid grinding. In this approach the preformed MOF and the functional material such as ILs are directly mixed without using other solvents. By using a mortar and a pestle, ILs are incorporated into the pores of the MOF. In order to achieve a better diffusion of ILs into the pores of MOF, the mixtures are usually heated for a couple of hours. Some researches on IL/MOF,[80,81] NP/MOF,[82] MC5@MIL-100Fe[83] composite materials use this post-synthesis impregnation technology.

Chemical vapor deposition is also a common technique for the construction of MOF-based composites. In this technique, a precursor of the functional material such as metal nanoparticles generate the vapor under vacuum, which is introduced into the pores of the MOFs. Metal NPs are formed inside the pore of the MOF by thermal decomposition or hydrogen reduction. The MOF-based composites using this synthesis technology are

MNP@MOF-5 (M = Pd, Au and Cu),[84] Pd@MOF-177, Cu@MOF-177,[85] Ni@ZIF-8,[86] and so on.

## 1.4 Potential applications of MOFs

At present, "energy" and "environment" have become two of the critical issues facing humanity in this era. Lots of examples demonstrate that MOFs provide enormous application values for implementation in real-world systems, especially those pertinent to issues concerning energy and environment. Thus, we focus on these two applications adsorption-based heat transformation and sulfur dioxide adsorption.

### 1.4.1 Adsorption-based Heat Transformation

Adsorption-based heat transformation (AHT) is a physical process based on the cycling adsorption-desorption of a working fluid in a porous adsorbent material. It makes full use of low-temperature sources (solar, geothermal, industrial waste heat, etc.)[87] for heat and cold reallocation, as driving heat for the regeneration. In other words, it converts exothermic and endothermic process into the useful heating and cooling by applying the thermodynamic principle. Thus, AHT contributes to energy-saving technologies, due to the huge demand for electricity or fossil fuels consumption in the conventional vapor compression systems.[88] AHT includes different branches, such as adsorption heat pump (AHP), adsorption chiller (AC) and heat storage.

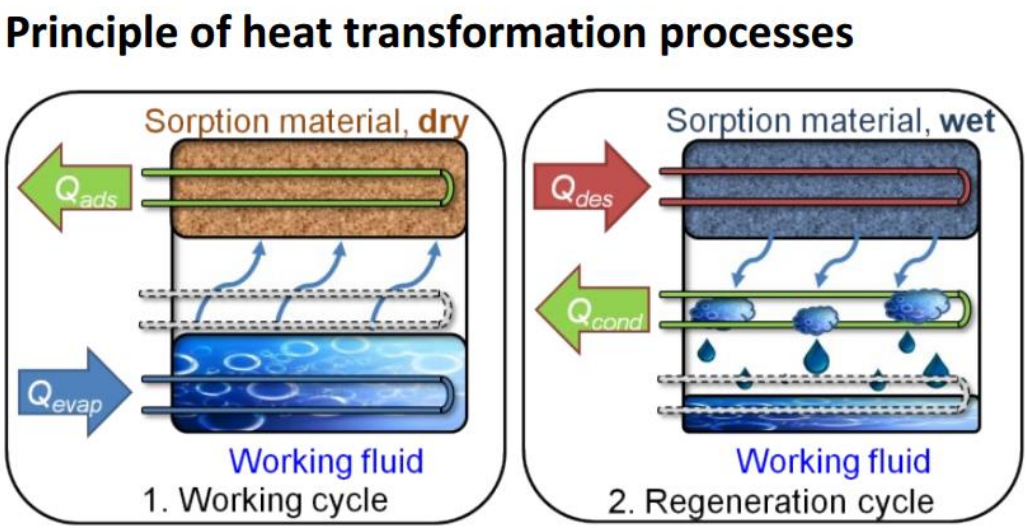


**Figure 9.** In the working cycle, a working fluid is evaporated at a low pressure, taking up evaporation heat $Q_{evap}$. During incorporation into a porous material, heat of adsorption $Q_{ads}$ is released. In the regeneration cycle, driving heat for desorption $Q_{des}$ is applied, and further condensation takes place at a medium temperature level and releases condensation heat $Q_{cond}$. Two applications can be chosen: (i) cooling ($Q_{evap}$) or (ii) heating ($Q_{ads}$+$Q_{cond}$). Reproduced from ref 89. Copyright 2013 American Association for the Advancement of Science.

As an alternative to traditional heat exchangers, AHT has been intensively developed over the last two decades, including thermally driven adsorption chillers (TDCs), adsorption heat pumps (AHPs) and heat storage. The schematic diagram of the working principle is also illustrated in Figure 9.[89] Heat is taken up from the surroundings by the evaporation of the working fluid ($Q_{evp}$), when an active dry adsorbent carries out the adsorption process on the working liquid. The part of heat converts into the useful cooling in thermally driven adsorption chillers (TDCs). As the adsorption is exothermic ($Q_{ads}$), heat will be released into the surroundings at a higher temperature level. Once the adsorbent is saturated with working fluid, regeneration is processed by using a low driven temperature (solar heat or waste heat). Energy is taken up from an external heat source to desorb the working fluid ($Q_{des}$), subsequently heat is released by the process of the condensation of the working fluid ($Q_{cond}$). The heat of adsorption by the active sorbent materials and the heat of condensation of the working fluid both can be used in

the adsorption heat pumps (AHPs).[90] Therefore, AHT can be used for heating or cooling applications, depending on whether an exothermic or endothermic process is utilized.

Furthermore, the working pairs and boundary working conditions have been intensively discussed.[91,92] The working pair of adsorbent-adsorbate plays a vital role in the performance of the adsorption system. Silica gel, activated carbon and zeolites are commonly chosen as adsorbent and water, methanol, ethanol[93] and ammonia can be used as adsorbate (working fluid). The basic thermodynamic data of the working fluids is shown in Table 2. Among them, water is the most used as working fluid, due to its non-toxic, high evaporation enthalpy (2440 kJ $mol^{-1}$ at 25 °C) and harmless to the environment.

**Table 2** Thermodynamic properties of common working fluids.

| Working fluid | Heat of vaporization at 25 °C [kJ/kg] | Freezing point at 101.3 kPa | Saturation vapor pressure at 25 °C |
|---|---|---|---|
| **Water ($H_2O$)** | 2440 | 0 °C | 3.2 kPa |
| **Methanol ($CH_3OH$)** | 937 | –98 °C | 17.0 kPa |
| **Ethanol ($C_2H_5OH$)** | 724 | –114 °C | 8.0 kPa |
| **Ammonia ($NH_3$)** | 502 | –78 °C | 1003 kPa |

The cycle conditions strongly determine the adsorption performance of a specific adsorbent. The temperature boundaries are defined by the setup of the equipment and the specific application procedure. Some common heat sources are listed in Table 3.

**Table 3** Overview of temperature boundaries for AHT.[94]

| | Application | Heat source | Temperature |
|---|---|---|---|
| **Low temperature source** | Heating | Earth probe | 10°C |
| | Heating | Ambient air | –10°C to 15°C |
| | Cooling | Ambience | –10°C to 20°C |
| **Middle temperature** | Heating | Floor heating | 35°C |
| | Heating | Radiator | 60°C |
| | Cooling | Ambience | 35°C |
| **Desorption temperature** | — | Waste heat | 55–100°C |
| | — | Gas burner | >100°C |

The requirements for the adsorbent can be derived from the application. AHT is a cyclic application, the adsorbents ought to possess high hydrothermal stability at application temperatures for thousands of cycles. The relative pressures at these temperatures ($p_S$(T)) can be calculated for adsorption and desorption when steep adsorption/desorption occurs:

$$\left(\frac{p}{p_0}\right)_{ads} = \frac{p_s(T_{evap})}{p_s(T_{ads})}, \qquad \left(\frac{p}{p_0}\right)_{des} = \frac{p_s(T_{cond})}{p_s(T_{des})}$$

For a typical heat pump setup, equipped with an evaporation temperature of 10 °C (water saturation pressure of 1.2 kPa), a middle temperature of 35 °C (water saturation pressure of 5.6 kPa) and a regeneration temperature slightly below 100 °C (water saturation pressure of 80 kPa), the preferable relative pressure is from 0.07 to 0.22.

The properties of adsorbents suitable for AHT applications include low regeneration temperature, high uptake at low relative pressures, and long-term hydrothermal stability.

The coefficient of performance (COP) is a commonly used parameter to describe energy efficiency. The COP is defined as the useful energy output divided by the energy required as input. For heating and cooling, the individual COPs become:

$$COP_H = \frac{-(Q_{con} + Q_{ads})}{Q_{regen}}, \qquad COP_C = \frac{Q_{evap}}{Q_{regen}}$$

$Q_{con}$ is the energy released during the condensation process, and $Q_{ads}$ is the energy released during the adsorption phase. Both have a negative value, because it is an exothermic process and energy is released from the adsorption cycle. $Q_{evap}$ is the energy taken up in the evaporator. $Q_{regen}$ is the energy required for regeneration of the adsorbent. Both have a positive value as energy is added to the system (ideally $Q_{ads} + Q_{con} = Q_{des} + Q_{ev}$). The energy required for regeneration ($Q_{regen}$) is in the same order of magnitude as the energy gained during adsorption ($Q_{ads}$). In addition, as the enthalpy

of adsorption is physically greater than the enthalpy of evaporation, $Q_{ads}$ will be also greater than $Q_{con}$ in absolute value. Thus, the coefficient of performance for adsorption and desorption process becomes:

$$1 \leq COP_H \leq 2 \quad COP_C \leq 1$$

The $COP_H$ range from one to two and $COP_C$ values range from zero to one. Thus, an optimal adsorbent should offer a higher energy efficiency towards the adsorbate at a specific boundary condition of the cycle.

### 1.4.2 Sulfur Dioxide Adsorption

In recent years, there are approximately 1.2 million tons of $SO_2$ generated by coal-fired power plants each year in the United States.[95] The first environmental problems associated with $SO_2$ occurred in the last century was acid deposition, which led to the loss of minerals and nutrients in the soil.[96] In addition, the dramatic rise in atmospheric $CO_2$ levels is largely attributed to the burning of coal, oil, and natural gas, which account for 80% of the $CO_2$ emissions worldwide.[97,98] Those gases have forced humanity to confront various related environmental issues, such as global warming, acid rain, ecological imbalance and so on.[99] As an example of the adverse effects on humans, the World Health Organization (WHO) announced that air pollution caused about 4.2 million premature deaths in 2016.[100]

Sulfur dioxide ($SO_2$) in the atmosphere primarily comes from the combustion of fossil fuels to generate electricity. The main components contain $CO_2$ (10–15% [v]), $N_2$ (70–75% [v]) and $H_2O$ (~10–18% [v]) in the industrial flue gas stream,[101,102] with the trace amount of $SO_2$ (0.00325% [v], 500–3000 ppm)[103]. Flue-Gas Desulfurization (FGD) is a technology that removes sulfur dioxide ($SO_2$) or sulfur oxides ($SO_x$) from the flue gas emitted by thermal power plants or other industrial facilities such as incinerators.[104,105] The wet scrubbing FGD technologies is the most mainstream, and have advantages in their large-scale implementation and mature technology. As shown in Figure 10a, the

fly ash is processed by an electrostatic precipitator, the flue gas is blown into the reaction tank, also termed a scrubber. Lime or limestone slurry is pumped in and sprayed from the top of the tank, and reacts with the $SO_2$ in the flue gas to form insoluble $CaSO_3$, which further reacts with oxygen to generate gypsum ($CaSO_4 \cdot 2H_2O$). Generally, up to 95% $SO_2$ from the gas mixture can be removed by the limestone scrubbing GFD.[106] However, trace amounts of $SO_2$ <500 ppm remain in the flue gas and are emitted into the atmosphere. Therefore, further reducing the $SO_2$ content in flue gas is of high economic and environmental importance.

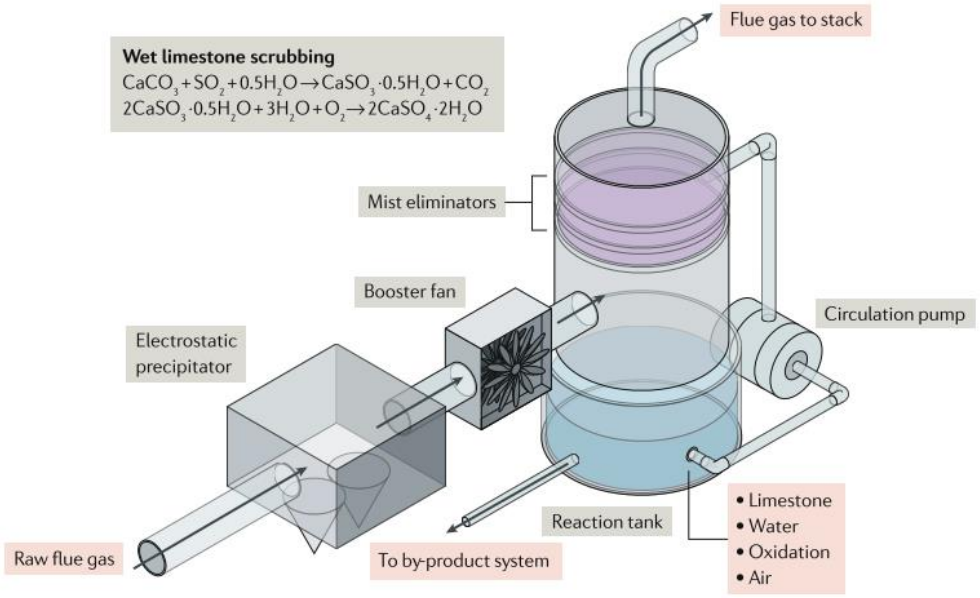


**Figure 10.** Schematic of $SO_2$ removal through wet limestone scrubbing flue gas desulfurization (FGD) process. Reproduced with the permission from ref 108. Copyright 2019 Nature Publishing Group.

MOF materials are a promising alternative for the capture of $SO_2$, mainly due to the specific chemical functionality and pore dimensions.[107,108] The porosity properties of MOFs, such as BET surface area, and pore volume determine the $SO_2$ uptake capacity. Due to their adsorption properties can be finely tuned according to the pore topology and chemical composition (chemical functionalities), MOFs are one of the most promising candidates for capturing the toxic $SO_2$ gas. The interaction between MOFs and the toxic molecules can be optimized and the gas adsorption performance can be

enhanced. The affinity of $SO_2$ and MOFs structure could be improved by the following strategies:

(i) coordinatively unsaturated metal sites (open metal sites). For example, MFM-170 was reported by Yang and Schröder in 2019, and in its paddlewheel SBU one $Cu^{2+}$ center is axially coordinated to the nitrogen atom of the pyridyl ligand, and the other $Cu^{2+}$ coordinatively unsaturated towards the center of the pore. It was demonstrated that the open $Cu^{2+}$ site is the thermodynamically strongest $SO_2$ binding site, but it is weak enough to almost completely desorb when the pressure is reduced.[109]

(ii) OH groups. MFM-300(In) reported by Yang and Schröder in 2016, consists of SBU $[InO_4(OH)_2(COO)_4]$ octahedra and tetradentate ligands ($L^{4-}$ = biphenyl-3,3',5,5'-tetracarboxylate).[110] It is confirmed that $SO_2$ molecules are mainly bonded to the μ-OH groups through hydrogen bonds and the hydrogen bonds is further enhanced by surrounding weak supramolecular interactions with C-H atoms from the aromatic ring of the ligand.[111]

(iii) defective sites. Navarro and co-workers reported defective nickel pyrazolate MOF materials for the enhanced $SO_2$ adsorption uptake and $SO_2/CO_2$ selectivity, via incorporating extra-framework $Ba^{2+}$ ions inside the pores of the framework.[112] Owing to the introduction of defects, the basicity of the nickel hydroxide cluster was increased, accompanied by the enhanced affinity with $SO_2$ molecules via acid-base interaction. Moreover, the presence of extra-framework $Ba^{2+}$ located close to the defect sites contributes to the formation of more stable $MSO_3$ sulfite species.

(iv) halogen functionalization. Xing reported in 2017 a series of MOF materials SIFSIX-1-Cu, SIFSIX-2-Cu, SIFSIX-2-Cu-i, SIFSIX-3-Zn and SIFSIX-3-Ni containing inorganic hexafluorosilicate ($SiF_6^{2-}$, SIFSIX) anions (wherein ligand 1 = 4,4'-bipyridine, 2 = 4,4'-dipyridylacetylene, i = interpenetrated, 3 = pyrazine), the results showed that SIFSIX-1-Cu exhibits a high $SO_2$ adsorption capacity

(11.01 mmol·g$^{-1}$ at 1.01 bar) with an excellent $SO_2/CO_2$ selectivity of 54–70. SIFSIX-1-Cu and SIFSIX-2-Cu-i showed significantly high $SO_2/N_2$ selectivity, owing to the strong electrostatic interaction between the $SO_2$ molecules and the $SiF_6^{2-}$ anions, supplemented by the dipole-dipole $SO_2$-$SO_2$ interactions.[113]

The structural stability and reusability of the MOFs are also important parameters for capturing corrosive $SO_2$ in a practical environment. Similar to the factors affecting the water stability of MOFs, some of those also affect the stability of MOFs toward $SO_2$, such as the strength of the metal-ligand bond, the oxidation state of the central metal atoms, the robustness of the metal clusters and the supramolecular host-guest interactions. In addition, some materials are stable to corrosive gases in single-component studies, however, in actual industrial applications, the potential side reaction of acid gases to produce strong acids in the humid air will make them unstable.[114,115] For example, a series of M-DMOF-TM (M = Co, Ni, Cu or Zn) materials were confirmed to be stable both in the presence of water vapor up to 85% relative humidity and after exposure to dry $SO_2$, however, M-DMOF-TM materials were decomposed when exposure to humid $SO_2$.[114] Besides, MIL-125 and $NH_2$-MIL-125, reported by Walton group in 2016, were investigated with a combination of experimental and computational methods, MIL-125 was stable after exposure to either dry $SO_2$ or water, while it was found to be unstable after exposure to humid $SO_2$, probably due to the formation of a new acidic species causing the degradation of the MIL-125 framework. Yet, $NH_2$-MIL-125 was stable under all the experimental conditions including dry $SO_2$, water and even humid $SO_2$. It was explained that the degradation reaction pathway under humid $SO_2$ conditions for $NH_2$-MIL-125 requires a higher energy barrier.[115] In addition, a facile regeneration condition for the materials used for the capture of $SO_2$ is highly considerable.

# 2 Motivation and objectives

For work one, a prototypical UiO-66 as a water adsorbent has been intensively investigated for adsorption heat transformation (AHT), but the uptake capacity at low pressure is still low (36 mg $g^{-1}$ at $p\,p_0^{-1} = 0.1$ and 179 mg $g^{-1}$ at $p\,p_0^{-1} = 0.3$). Inorganic salt such as LiCl has a high hydrophilic nature. Thus, a new strategy for the encapsulation of the inorganic salt LiCl in the pore of UiO-66 is proposed. The obtained composite could help improve the water adsorption capacity of UiO-66, which is favorable toward AHT application. Meanwhile, it could prevent the occurrence of deliquescence of LiCl, due to the limited confine space of adsorbed water inside the pore of UiO-66.

For work two, MIL-101(Cr) has a large BET surface area, high pore volume, and high-water stability, but low affinity for $SO_2$ under low pressure (0.7 mmol $g^{-1}$ at 0.01 bar). Cucurbit[6]uril (CB6) shows high affinity with $SO_2$ under low pressure, but has poor stability under humid conditions. Therefore, a composite material can be fabricated by dispersing CB6 molecules in the pore of MIL-101(Cr). The purpose is to increase the $SO_2$ adsorption capacity of MOF under low pressure while maintaining stability under wet $SO_2$. The composite material can be a promising candidate for the flue gas desulfurization application.

# 3 Cumulative Part

This chapter describes the published works for this thesis. Each published or submitted work is independent, including a separate short introduction section and a separate reference list. These publications are presented in scientific, peer-reviewed journals, attached the supplementary information. Figures, tables and schemes in each publication do not use the numbering of the thesis, but independently adopt the numbering of the publication itself. Each publication has a short introduction containing the journal name, graphical abstract, highlights and the authors' contribution to the work.

## 3.1 Tunable LiCl@UiO-66 composites for water sorption-based heat transformation applications

Yangyang Sun, Alex Spieß, Christian Jansen, Alexander Nuhnen, Serkan Gökpinar, Raphael Wiedey, Sebastian-Johannes Ernst and Christoph Janiak

Journal of Materials Chemistry A. 2020, 8, 13364-13375.

https://doi.org/10.1039/D0TA03442H

Impact factor 2020: 12.732

**Graphical abstract**

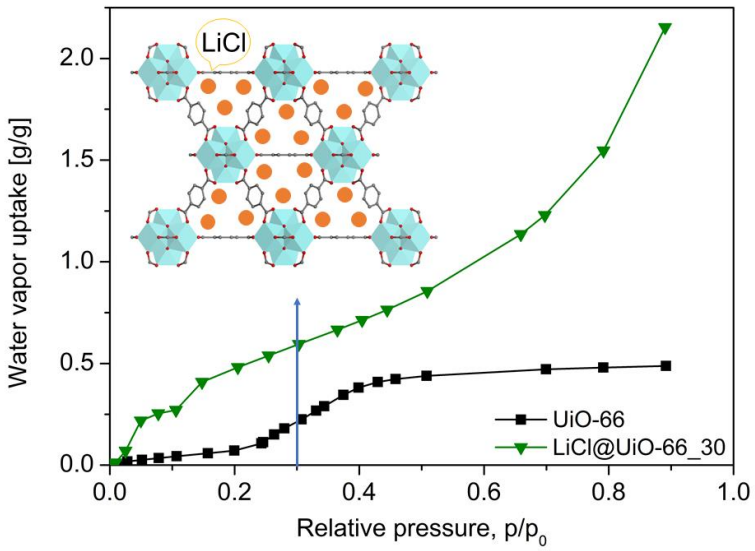


**Highlights:**

We report a salt@MOF composite with

- no deliquescence (contrary to many other literature reports on salt@MOF we did not let dry the excess salt solution but applied careful washing cycles);
- proven 10 cycle stability;
- increased water uptake over neat MOF;
- and higher water uptake over neat LiCl at low relative pressure (low humidity);
- a kinetics evaluation showing a faster water uptake over many other similar

composites;

- a coefficient of performance (COP) exceeding those of many other similar composites;

- a heat storage capacity ($C_{HS}$) of up to 900 kJ/kg (= 0.25 kWh/kg), exceeding the DOE target of 0.07 kWh/kg for thermal battery applications.

Author's contribution to the work:

My contributions:

- Experimental work and analysis (with the helpful discussion from Christian Jansen and Serkan Gökpinar)

- Writing the manuscript, drawing up the figures (exception: Scheme 1) and tables

- SEM images were taken by Alex Spieß

- The gravimetric cyclic water vapor measurements were processed with the help of Raphael Wiedey

- The schematic working principle (Scheme 1) of an adsorption-based thermal battery (ATB) was drawn by Sebastian-Johannes Ernst. The coefficient of performance (COP) for heating pump mode under the application-specific condition were calculated and discussed by Sebastian-Johannes Ernst and Alexander Nuhnen

Corrections of the manuscript and responses to reviewers during the review process were made by Prof. Christoph Janiak

The work presented in this chapter has been published in:

## Tunable LiCl@UiO-66 composites for water sorption-based heat transformation applications†

Yangyang Sun,[a] Alex Spieß,[a] Christian Jansen,[a] Alexander Nuhnen,[a] Serkan Gökpinar,[a] Raphael Wiedey,[b] Sebastian-Johannes Ernst,[c] Christoph Janiak[a]* *J. Mater. Chem. A*, 2020, **8**, 13364-13375. DOI: 10.1039/d0ta03442h.



## Abstract

Porous composite materials are potential candidates for water-based adsorptive heat transformation (AHT) applications. Here, the solid adsorbent LiCl@UiO-66 as composite 'salt inside porous matrix' (CSPM) has been prepared by incorporating hygroscopic lithium chloride into the microporous metal-organic framework (MOF) UiO-66 as host matrix through the wet impregnation method. In our wet impregnation we did not let dry the excess salt solution to prevent salt precipitation on the matrix surface. This yielded a true salt@MOF composite with no deliquescence of LiCl and strongly enhanced the water adsorption capacity of UiO-66 through the salt content. At $p/p_0 = 0.1$ the water vapor sorption isotherms show a hydration state of LiCl inside the MOF of LiCl·2-4$H_2O$ which is much higher than for neat LiCl with 0.5$H_2O$, due to the dispersion of a small particle size inside the matrix. LiCl@UiO-66 with 30 wt% LiCl content (LiCl@UiO-66_30) has a 3 to 8 times higher water uptake over neat UiO-66 (depending on relative pressure) and could reach a volumetric and gravimetric water uptake of over 2.15 g/g at $p/p_0 = 0.9$, which outperforms the so far known UiO-66-based composites. Cycling tests confirmed the hydrothermal stability of the LiCl@UiO-66 composites. Kinetic evalution of the gravimetric water uptake (at 90% relative humidity) over time yielded rate coefficients up to $2.0(1) \times 10^{-4}$ $s^{-1}$ which is

slower than in neat UiO-66 (6.7(6) × $10^{-4}$ $s^{-1}$) but faster than for salt@silica gel composites. The coefficient of performance for heat pumping mode (at $T_{des}/T_{ads}/T_{evap}$ set to 90/40/10 °C) of 1.64 for LiCl@UiO-66_30 exceeds those of other MOFs, salt@MOF or salt@silica gel composites. For thermal battery applications the heat storage capacity ($C_{HS}$) for LiCl@UiO-66_30 is 900 kJ/kg (= 0.25 kWh/kg), which can reach the Department of Energy (DOE) value of 2.5 kWh/35 kg with just 10 kg of material and outperforms $CaCl_2$@UiO-66_38 with a CHS value of 367 kJ/kg.

## Introduction

Adsorptive heat transformation (AHT) systems have demonstrated the possibility to run air conditioners with lower electricity consumption than compressor systems by operating on low thermal energy sources such as industrial waste heat and solar energy for regeneration and driving energy.[1-4] AHT is based on cycling adsorption and desorption of a working fluid in a highly porous substrate (Fig. S1, ESI†). AHT includes different branches such as adsorption heat pumps (AHPs), adsorption chillers and heat storage. Different vapors can be used as working fluid, like methanol, ethanol and water. Water is preferred for AHTs, because of its high evaporation enthalpy, ready availability and environmentally friendly features.

To date, many kinds of porous materials have been investigated for adsorptive heat transformation (AHT), including silica gels,[5] activated carbons,[6,7] zeolites,[8] aluminophosphates[9,10]and more recently metal-organic frameworks (MOFs).[11-16] Two recent studies of MOFs for AHT include a new MOF framework CAU-23 with ultra-low regeneration temperature for adsorption chillers[17] and an easy hydrophilicity tuning of Al-Based MOFs through solid-solution mixed-linker strategy.[18] MOFs can be designed or functionalized by post-synthetic modification to increase their water uptake capacity and adjust the relative vapor pressure region.[19-23] Although some investigations of MOFs have been made in AHT, disadvantageous aspects, such as low adsorption capacity are still to be tackled in real applications.

'Composites salts inside porous matrix' (CSPM) combine porous materials as matrix and inorganic salt as active ingredients.[24] The inorganic salt is intended to improve the water sorption capacity of the porous material, and the matrix of porous material could avoid the drawbacks of inorganic salts in an AHT process such as deliquescence and intumescence (swelling up). (Deliquescence is the absorption of moisture by a substance until it dissolves in the absorbed water to yield a solution.)

Mechanistically water sorption at a CSPM is considered to occur by water adsorption on the host matrix, inducing the chemical reaction between water and salt, resulting in the formation of crystalline hydrates, and eventually water *ab*sorption by the aqueous salt solution in the pores (Fig. S2, ESI†). The host matrix provides for efficient transfer of the heat of hydration and disperses the salt reagent, which greatly enhances the reaction kinetics. The vapor-solid reaction is much faster for a dispersed salt inside the host than for bulk salt, so that the rate of the sorption process is only controlled by inter- or intraparticle diffusion. Consequently, the water sorption by a composite is not a linear combination of that of the host matrix and salt.[24-27] Therefore, salt@MOF composites should combine the merits of the salt and the pore features of the MOF. The typical active salts for CSPMs are halides, sulfates, nitrates of alkali and alkali-earth metals.[28] Moreover, a porous material with an already higher water uptake capacity under low relative pressure ($p/p_0$ below 0.3) is preferred for AHTs.

Up to now, only a few MOF-based CSPMs have been reported. Garzón-Tovar *et al.* developed a UiO-66-based CSPM adsorbent with 38 wt% $CaCl_2$ for thermal batteries and 53 wt% $CaCl_2$ for refrigerator using a spray-drying continuous flow method.[29] Permyakova *et al.* analyzed six water-stable MOFs containing $CaCl_2$, prepared by soaking MOFs in the inorganic salt solution. It was demonstrated that mesoporous and amphiphilic robust MOFs could achieve a higher salt encapsulation rate. The higher loading lifts and energy storage densities of MIL-100(Fe) with 46 wt% $CaCl_2$ and MIL-101(Cr) with 62 wt% $CaCl_2$ composite sorbents were suggested for seasonal heat

storage.[30] Tan *et al.* synthesized the composites salt@MIL-101(Cr) whose salt content was up to 60 wt% $CaCl_2$ and 42 wt% LiCl when the salt solution concentration was 30% $CaCl_2$ and 20% LiCl through incipient wetness impregnation. For the 60 wt% CSPM deliquescence was observed, but the composites with 53 wt% $CaCl_2$ and 36 wt% LiCl exhibited low desorption activation energy, fast sorption rates and high adsorption in low humidity compared to neat MIL-101(Cr).[31] Xu et al. reported LiCl@MIL-101(Cr) composites through adding a specified quantity of LiCl into a well-dispersed MIL-101(Cr) aqueous suspension (5 mg/mL) for sorption-based atmospheric water harvesting (AWH) in arid climates. LiCl@MIL-101(Cr) composites have a high-water sorption performance of 0.77g/g under arid working conditions (30% RH at 30 °C) and an AWH device based on this composite adsorbent can be utilized by natural sunlight without putting in additional energy.[23] All these efforts showed that the water vapor uptake of MOFs could be improved after incorporating salt into the parent adsorbent.

Herein, we have explored the influence of three different weight fractions of LiCl on the sorption properties of UiO-66-based novel LiCl@UiO-66 CSPMs. Extensive thermodynamic and kinetic water adsorption studies were carried out on UiO-66-based CSPMs, which show no deliquescence but a higher water adsorption capacity than neat UiO-66. We selected UiO-66 as the porous matrix because of its exceptional chemical and thermal stability.[32] LiCl was chosen due to its known high hydrophilicity.[33]

## Experimental

### Materials and instrumentations

The chemicals used were obtained from commercial sources. Zirconium(IV) chloride ($ZrCl_4$, 98%) was bought from Alfa Aesar, 1, 4-benzenedicarboxylic acid ($H_2BDC$, > 99%) from Acros Organics, N,N-dimethylformamide (DMF, 99.5%) from Fisher Chemicals, and lithium chloride anhydrous was purchased from Fischer Scientific. No further purification was carried out. The water used was Millipore deionized water.

Powder X-ray diffractometry (PXRD) was performed at room temperature on a Bruker D2 Phaser powder diffractometer equipped with a flat silicon, low background sample holder using Cu-Ka radiation ($\lambda$ = 1.5418 Å) in the range of 5° < 2$\theta$ < 50° with a scanning rate of 0.0125° $s^{-1}$ (300 W, 30 kV, 10 mA). The analyses of the diffractograms were carried out with the "Match! 3.5.3.109" software.

SEM images were acquired on a Jeol JSM-6510LV QSEM Advanced electron microscope (Jeol, Akishima, Japan) with a LaB6 cathode at 5-20 keV. The microscope was equipped with an Xflash 410 (Bruker, Billerica, US) silicon drift detector and the Bruker ESPRIT software for EDX analysis.

The adsorption–desorption isotherms of nitrogen were measured at 77 K using an Autosorb-6 from Quantachrome and evaluated with the AsiQwin V3 software. For activation, the sample was degassed in a vacuum of $5 \times 10^{-2}$ mbar at 150 °C for 12 h. The Brunauer−Emmett−Teller (BET) surface areas were calculated in the $p/p_0$ range of 0.01−0.05. Total pore volumes were calculated from nitrogen adsorption isotherms at $p/p_0 = 0.90$. Nitrogen sorption isotherms were also measured on a Micrometrics ASAP 2020 in order to obtain the pore size distribution which was calculated using NDFT method at 77 K for "$N_2$ on cylindrical pores".

Flame atomic absorption spectroscopy (AAS) was performed on a PerkinElmer PinAAcle 900T spectrometer equipped with a single element lithium hollow cathode lamp using mixture gases of $N_2O$ and air. The wavelength of Li is 670.78 nm. The slit width in the spectrometer was 0.2 nm.

A Varian 715-ES ICP-optical emission spectrometer was used. Approximately 5 mg of the sample was mixed with 8 mL of aqua regia and 2 mL of hydrofluoric acid. The digestion was performed in a microwave-assisted sample preparation system "Multiwave PRO" from Anton Paar at ~220 °C and ~50 bar pressure. The digested

solution was filled up to 100 mL and measured with ICP-OES. The data analysis was performed on the Varian 715-ES software "ICP Expert".

Water vapor sorption multi-cycle tests of the composites were carried out with a gravimetric SPS11-10µ water sorption analyzer from proUmid, Germany. The mass of the sample was recorded every 10 minutes by an electronic balance with an accuracy of ±10 µg. For each sample, the mass change at different sorption times was calculated as mass change at equilibrium related to the lowest net weight in %. The cycles between a relative humidity of 90% and 0% were carried out under a maximum equilibration time of 3 hours per climate cycle. The minimal mass of each sample was 50 mg. The adsorption kinetics curve was acquired at 20 °C and at a set target relative humidity of 90%, which took around one hour to achieve in the chamber. Another 40 cycles were performed under a relative humidity of 80% and 20% with a maximal equilibration time per climate cycle of 2 h. The general equilibrium condition was 0.01% per 15 minutes.

Volumetric water vapor sorption isotherms were measured on a Quantachrome VSTAR vapor sorption analyzer at 293 K. For activation, the sample was evacuated on the FloVac®Degasser at 150 °C for 16 h. The volumetric water sorption measurement was performed under the possible "slowest" condition, that is, the maximum possible time provided by the setting parameters before the measurement advanced to the next data point. The equilibrium settings for volumetric measurement under ‘pressure points mode’ were ‘Equilibrium points number: 10’; ‘Equilibrium points interval time (s): 90 to 180’; ‘Sorption rate limit (Torr/min): 0.001 to 0.01’. From repeated and reproducible volumetric water vapor sorption isotherms the variance of the water uptake values is around 5%.

Thermogravimetric analysis (TGA) was done with a Netzsch TG 209 F3 Tarsus in the range from 25 to 600 °C, equipped with an $Al_2O_3$-crucible and applying a heating rate of 5 $K \cdot min^{-1}$ under air atmosphere.

**Synthesis of UiO-66**

UiO-66, $[Zr_6(\mu_3\text{-}O)(\mu_3\text{-}OH)_4(BDC)_6]$ (BDC = benzene-1,4-dicarboxylate, terephthalate) was synthesized using a slightly modified procedure of Lillerud *et al.*,[34] with decreasing the amount of N,N-dimethylformamide, DMF. The molar ratio of the reactants was $ZrCl_4$: $H_2BDC$: DMF = 1: 1: 135. The typical synthesis procedure was as follows: $ZrCl_4$ (2.33 g, 10 mmol) was dissolved in 55 mL of DMF and terephthalic acid (1.66 g, 10 mmol) in 50 mL of DMF. The ligand solution was slowly added to the metal salt solution and after 30 min of stirring, the mixture was distributed into three appropriately-sized Teflon-lined autoclaves. The autoclaves were placed in an oven at 120 °C for 24 h. The precipitates were collected via centrifugation, thoroughly washed with DMF (20 mL twice) and then immersed in 20 mL of methanol for 3 days. After separation, the solid products were dried in the oven at 65 °C overnight and then in a vacuum oven ($5 \times 10^{-2}$ mbar) at 150 °C for 12 h. The combined yield was 1.88 g (68%).

**Preparation of LiCl@UiO-66 CSPM samples**

Three different concentrations of LiCl solution with 5.9 mol/L, 10.1 mol/L and 15.5 mol/L were prepared. UiO-66 samples were outgassed at 150 °C under vacuum ($5 \times 10^{-2}$ mbar) to remove water and volatile impurities. Activated UiO-66 (500 mg) was immersed in 10 mL of LiCl solution with different concentrations for 4 hours at room temperature. The solid samples were separated from the LiCl solution by centrifugation and decantation of the supernatant, then washed one time with 8 mL of water for 5 minutes to remove any salt adhering to the outside surface of the MOF particles (Scheme S1, ESI†). Finally, the samples were dried at 65 °C in an oven overnight. Yields were 515 mg, 550 mg and 587 mg, for LiCl@UiO-66_x, x = 9, 19, 30, respectively. For impregnation, the times of 12 h[22,31] and of 2h or less[30,35] were reported in the literature. We have conducted the impregnation procedure for 6 or 4 hours with different concentrations of LiCl, which led to similar results. Thus, we decided to choose the less time-consuming procedure.

The composite LiCl@UiO-66_36 was obtained from UiO-66 impregnated with the 15.5 mol/L LiCl solution under the same condition, except that the washing process was only 2 minutes.

For the recycled UiO-66 from LiCl@UiO-66_30, samples of 50 mg each were immersed in 10 mL of methanol under stirring for 12 h, and then separated by centrifugation. The samples were dried and kept at 65 °C until analyzed further.

## Results and discussion

### Synthesis

Lithium chloride was used because of its large availability, low cost and excellent water vapor uptake capacity. Three UiO-66-based CSPMs were synthesized by immersion of activated UiO-66 (outgassed at 150 °C for 16 h under vacuum) in an aqueous solution (10 mL) of LiCl with different concentrations (5.9 mol/L, 10.1 mol/L and 15.5 mol/L) for 4 hours at room temperature (see Exp. section for details). We used a salt solution whose volume (Vs) exceeded the pore volume of the UiO-66 amount (Vp, that is, Vs > Vp). This method is called wet impregnation.[28] If the volume of the salt solution would have been the same as the pore volume (i.e. Vs = Vp) then this method is termed dry impregnation or incipient wetness impregnation.[28]

By mass, the offered amounts of LiCl were 2.5 g, 4.2 g and 6.7 g per 0.5 g of MOF. The samples were collected after centrifugation and washed to remove the inorganic salt adhering at the outside of the UiO-66 matrix. From atomic absorption spectroscopy (AAS) the mass fraction of LiCl in the CSPM samples was determined to 9, 19 and 30 wt% (see details in the ESI†). The samples were abbreviated accordingly as LiCl@UiO-66_x, where x is the mass fraction $m_{LiCl}/m_{CSPM} \times 100\%$ of LiCl in the composite (Table 1). The wt% of both Li and Zr was measured by inductively coupled plasma – optical emission spectroscopy (ICP-OES), confirming the above AAS values for wt% LiCl, and yielding the molar ratio of Li to Zr (Table 1). The amount of LiCl in

the composite increases, with the increase of impregnation salt concentration (Table 1). Still, from the theoretically possible loading of about 90 wt% of LiCl only about 30 wt% of LiCl were found incorporated (after the washing step).

**Table 1** LiCl content in UiO-66-based CSPMs

| Composite[a] | theor. max[b] wt% LiCl | wt% LiCl content[c] by AAS | wt% LiCl content[c] by ICP-OES | Atom ratio Li:Zr[d] |
|---|---|---|---|---|
| **LiCl@UiO-66_9** | 83 | 9 | 10 | 0.88 |
| **LiCl@UiO-66_19** | 89 | 19 | 20 | 1.53 |
| **LiCl@UiO-66_30** | 93 | 30 | 29 | 2.80 |

[a] The suffix _x in LiCl@UiO-66_x indicates the wt% LiCl = $m_{LiCl}/m_{CSPM} \times 100\%$ in the composite and was derived from the postsynthetic AAS measurement. [b] The theoretical maximum wt% LiCl if the full amount of LiCl would have been impregnated into the MOF. [c] LiCl content calculated from postsynthetic Li determination by AAS or ICP-OES, standard deviation of wt% LiCl is ±1. [d] The atomic ratio of Li: Zr was measured by ICP-OES

We emphasize that in our wet impregnation we did not let dry the excess salt solution to prevent salt precipitation on the matrix surface. In our work a specific amount of deionized water was used to remove the excess salt adhered on the external surfaces of the composites. Hence, only part of the salt inserted into the pores of the material and the rest was removed. It is worth noting that such washing workups are necessary in order to remove free inorganic salt precipitates from the external surfaces of MOF and to achieve a true salt@MOF incorporation in a composite. Yet such washing is rarely done in the literature following the wet impregnation.[23] Most authors simply allow the solvent from the salt solution to dry without separation by decantation or washing.[30,31] This then yields rather a physical mixture of salt and MOF with only part of the salt incorporated into the MOF. In comparison to other wet impregnation works with a similar separation (and washing) workup, the salt content of the LiCl@UiOs composite presented here is similar to the achieved salt incorporation in other works.[36.37] For example, for lithium chloride in silica gel the LiCl content in the composite was 13 wt% when the lithium chloride solution was 30 wt%.[36] When impregnating calcium chloride in silica gel the $CaCl_2$ content in the composite was between 12 and 35 wt% for $CaCl_2$

offered up to the solubility limit in water.[37] Noteworthy, for salt@MOF no similar separation (and washing) workups seem to have been done following wet impregnation. Other authors use wet impregnation without including a separation step of the supernatant excess salt solution and allow the salt solution to dry with salt precipitation on the matrix surface. Then higher weight percentages of salt@MOF became possible, such as 60 wt% $CaCl_2$ or 42 wt% LiCl in MIL-101(Cr).[31]

Powder X-ray diffractograms (PXRDs) of UiO-66 and CSPMs show that the structure of UiO-66 is preserved after the wet impregnation with LiCl solution (Fig. 1). Reflections corresponding to anhydrous or hydrated LiCl are not clearly observed in the PXRD pattern of the CSPM samples, although there may be an overlap with the nearby UiO reflections in the 2θ region of 30-36°. Still the almost absence of the characteristic peak at 24° 2θ for $LiCl{\cdot}H_2O$ rules out a significant $LiCl{\cdot}H_2O$ crystallization on the outer MOF surface. Inside the MOF, the pores are too small to allow for the formation of a diffracting crystalline LiCl phase, that is, with several unit cells in each direction. For the three CSPM samples, a significant decrease of the relative intensity of the diffraction Bragg peaks was observed with increasing LiCl content and in comparison to neat UiO-66 (under identical measurement conditions). This decrease is caused by the inorganic salt inside the matrix. We use approximately the same mass amount of the probes in our given sample holders. As the relative amount of MOF decreases in the composite with higher (non-diffracting) salt content, there will be less amount of MOF on the sample holder. With the incorporation of guest species in the pores of MOFs, also the electron density changes can lead to the decrease of PXRD intensity, especially in the low-angle range.[30,38,39] Scanning electron microscopy (SEM) images show that UiO-66 is crystallized as intergrown nano-sized particles. Under higher magnification, round 200 nm-sized particles could be observed. The SEM images of UiO-66 and its CSPMs show retention of crystallite morphology (Fig. 2). This also supports the absence of LiCl having formed outside the UiO-66 particles.

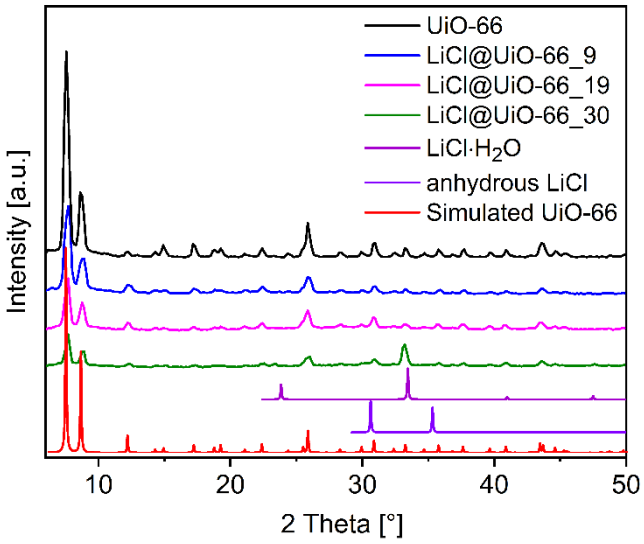


**Fig. 1** PXRD patterns of UiO-66, LiCl@UiO-66_x, x = 9, 19, 30, anhydrous LiCl (COD number:1011314), $LiCl \cdot H_2O$ (COD number:101495) and simulated diffractogram of UiO-66 (CCDC number: 1018045).[40]

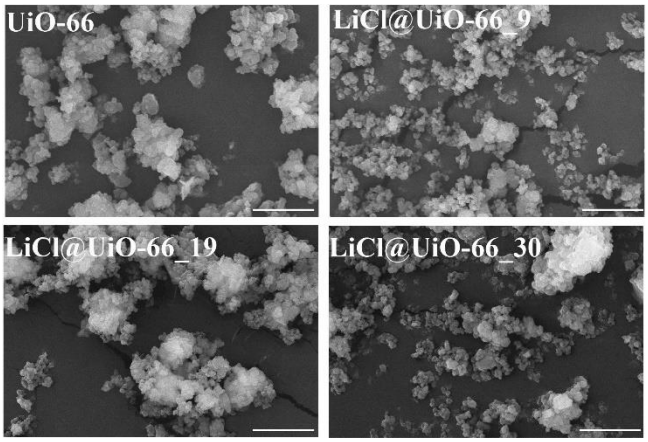


**Fig. 2** SEM images of UiO-66 and LiCl@UiO-66_x, x = 9, 19, 30. Scale bar 5 µm.

Lithium cannot be detected by energy dispersive X-ray (EDX) detector because as a light element it has a low X-ray (emission) yield due to the competing and predominant Auger electron emission.[40] The co-existence of Zr and Cl in the CSPM samples was confirmed by SEM-EDX elemental mapping (Fig. S3, ESI†) and demonstrates that LiCl was homogeneously distributed.

UiO-66 and other Zr-MOFs are known for and prone to missing-linker defects.[42] Zirconium-based MOFs can tolerate a detectable and significant defect amount without losing their structural stabilities.[41] The calculation of linker defects was carried out by

the quantitative analysis of thermogravimetric analysis (TGA) data (Fig. S4, ESI†) and followed the determination of linker defects by Shearer.[42] From TGA the number of missing-linker defects of UiO-66 was derived as 1.4 and the corresponding simplified formula unit then should be $[Zr_6O_{7.4}(BDC)_{4.6}]$ (compared to $[Zr_6O_6(BDC)_6]$).

Nitrogen physisorption measurements on neat UiO-66 and CSPMs exhibit Type I isotherms, which are indicative of microporous materials.[40] As shown in Fig. 3a, the nitrogen adsorption and desorption isotherms showed almost no hysteresis. Brunauer-Emmett-Teller (BET) surface area, total and micropore volume in the CSPMs exhibited a significant decrease, compared to neat UiO-66 (Table 2). This is attributed to the fact that the micropores of UiO-66 are filled with the incorporated LiCl. This pore filling by LiCl in an otherwise unchanged UiO-66 structure was verified through the removal of LiCl and the re-establishing of the original porosity. To remove LiCl, LiCl@UiO-66_30 was immersed in methanol for 12 h at room temperature (see Exp. section for details). The regained UiO-66 had a BET surface area of 1324 $m^2/g$ and a total pore volume of 0.53 $cm^3/g$, which is similar to pristine UiO-66 (1360 $m^2/g$ and 0.55 $cm^3/g$) (Table 2). The PXRD of the regained UiO-66 from LiCl@UiO-66_30 exhibits similar peak intensities to pristine UiO-66 under identical measurement conditions and, thereby, confirmed the interpretation of decreasing peak intensity being due to the LiCl content (Fig. S5, ESI†).

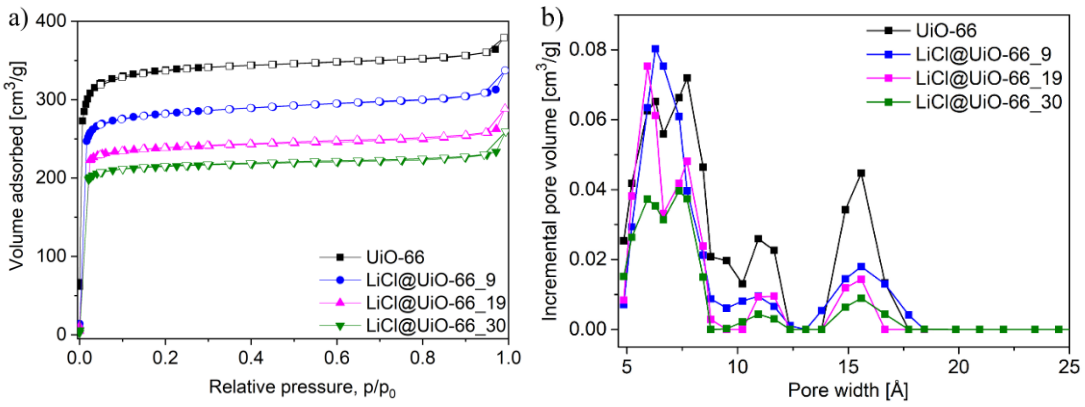


**Fig. 3** a) $N_2$ sorption isotherms of UiO-66 and LiCl@UiO-66_x (x=9, 19, 30). Filled symbols, adsorption; empty symbols, desorption. b) Pore size distribution of UiO-66

and LiCl@UiO-66_x. Pore size distributions were derived using the NLDFT method at 77 K.

The neat UiO-66 framework features pores of 8 and 11 Å (Fig. 3b), which are attributed to the tetrahedral and octahedral cages,[45,46] with the cages connected by triangular windows with an aperture width of 6 Å. The pore diameter range between ~14 to 18 Å is due to missing cluster (reo-type) defects.[47-49] CSPMs exhibit similar pore size distributions from UiO-66, however, the pores with 6 and 8 Å width are slightly shifted to smaller diameters, while the relative number of pores centered at 11 and 16 Å of UiO-66 decreased with the increase of impregnated salt in the CSPMs.

**Table 2** Porosity characteristics of neat UiO-66 and LiCl@UiO-66_x, x = 9, 19, 30

| | $S_{BET}$ [$m^2/g$][a] | $V_{total}$ [$cm^3/g$][b] | $V_{micro}$ [$cm^3/g$][c] | $V_{micro}/V_{total}$ |
|---|---|---|---|---|
| **UiO-66** | 1360 | 0.55 | 0.42 | 0.76 |
| **LiCl@UiO-66_9** | 1148 | 0.47 | 0.37 | 0.79 |
| **LiCl@UiO-66_19** | 966 | 0.39 | 0.31 | 0.79 |
| **LiCl@UiO-66_30** | 874 | 0.35 | 0.28 | 0.80 |
| **recycled UiO-66 from LiCl@UiO-66_30** | 1324 | 0.55 | 0.43 | 0.78 |

[a] Brunauer-Emmett-Teller (BET) surface areas SBET were obtained from five adsorption points in the pressure range p/p0 = 0.01 - 0.05. [b] Total pore volume $V_{total}$ calculated from $N^2$ sorption isotherm at 77 K ($p/p_0$ = 0.90) for pores ≤ 20 nm diameter. [c] Micropore volume obtained using the t-plot method from five adsorption points in the pressure range p/p0 = 0.05 – 0.18.

## Water sorption properties

Water vapor sorption isotherms of neat UiO-66, the pure LiCl salt and the three CSPMs were volumetrically measured to examine the effect of the incorporated inorganic salt (Fig. 4a).

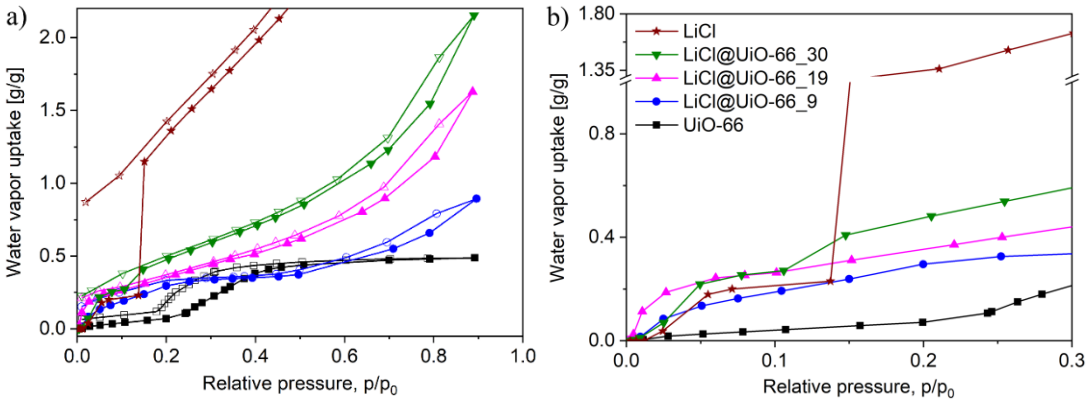


**Fig. 4** a) Water sorption isotherms of neat LiCl, UiO-66 and LiCl@UiO-66_x, x=9, 19, 30. Closed and open symbols refer to adsorption and desorption. The LiCl water uptake extends up to 5.46 g/g (Fig. S6, ESI†). b) Expanded uptake for clarity in the range of 0 < $p/p_0$ < 0.30. From repeated and reproducible volumetric water vapor sorption isotherms the variance of the water uptake values is around 5%.

The isotherm of UiO-66 shows an S shape curve (Type V isotherm).[44] Three CSPMs mainly exhibit an already increased water uptake over UiO-66 in the low-pressure region, in line with the first uptake step of LiCl at 0.05 $p/p_0$. The isotherm of the bulk salt shows the step-wise formation of the lithium chloride hydrates. This first uptake step of LiCl of 0.21 g/g below 0.1 $p/p_0$ can be ascribed to the formation of $LiCl{\cdot}0.5H_2O$. The large uptake jump for LiCl at ~0.15 $p/p_0$ or the second uptake step leading to about 1.25 g of $H_2O$/g(LiCl) is due to the formation of $LiCl{\cdot}3H_2O$ hydrate. LiCl@UiO-66_30 also displays the second step related to the hydration of LiCl. Noteworthy, the LiCl@UiO-66_19 and -30 surpass and LiCl@UiO-66_9 matches the LiCl water uptake up to ~0.14 $p/p_0$ (Table 3, values at $p/p_0 = 0.1$). This is remarkable in view of their lower LiCl content and the only very small uptake contribution from UiO-66.

Concerning the relative uptake pressure, a higher water uptake at low relative pressure over neat LiCl may be viewed as disadvantage for low-temperature regeneration. However, regeneration is never to be seen as an isolated process, since what matters is the exchanged amount of water per cycle. In general, it is correct that, in absolute terms, an uptake at a relative pressure as low as possible at a given desorption temperature is

favorable. However, when it comes to the application, the water exchange per cycle becomes more important.

If the water uptake of the three composites at $p/p_0$ = 0.1 (deducting the UiO contribution) is related to their LiCl wt%, we have 156/0.09, 228/0.19 and 235/0.30 mg($H_2O$)/g(LiCl). This translates into a hydration state of LiCl·4$H_2O$ for LiCl@UiO-66_9, of LiCl·3$H_2O$ for LiCl@UiO-66_19 and of LiCl·2$H_2O$ for LiCl@UiO-66_30 at $p/p_0$ = 0.1 which is much higher than for neat LiCl. This increased hydration is traced to the nanodispersion of LiCl in the MOF matrix in connection with the surface energy of these LiCl nanoclusters. The smaller nanoclusters in LiCl@UiO-66_9 will have a higher surface energy and thereby adsorb relatively more water on a mg($H_2O$)/g(LiCl) basis at the low $p/p_0$ values. This data is not to be confused with the data in Table 3 which is on a mg($H_2O$)/g(CSPM) for LiCl@UiO-66_x. Hence, it can be concluded that the properties of a "salt" in a porous matrix vary from those of the neat or bulk salt, due to the interactions between the salt and the matrix, the dispersion of a small particle size and its hydration behavior from the higher salt cluster-surface energy.[50]

**Table 3** Water vapor uptake for neat and CSPMs at the specific relative pressure

| | **Volumetric water uptake [mg/g] [a,b] at $p/p_0$ =** | | | **Gravimetric water uptake [mg/g] [a] (at $p/p_0$ = 0.9)** |
|---|---|---|---|---|
| | 0.1 | 0.3 | 0.9 | |
| **UiO-66** | 36 | 179 | 393 | 384 |
| **LiCl** | 216 | 1646 | 5460 | — |
| **LiCl@UiO-66_9** | 192 | 338 | 894 | 887 |
| **LiCl@UiO-66_19** | 264 | 455 | 1628 | 1682 |
| **LiCl@UiO-66_30** | 271 | 595 | 2153 | 2191 |

[a] The data means mg($H_2O$)/g(CSPM) for LiCl@UiO-66_x. [b] From repeated and reproducible volumetric water vapor sorption isotherms the variance of the water uptake values is around 5%.

The CSPMs LiCl@UiO-66_19 and -30 continue to steadily adsorb water in a Type III isotherm branch above 0.2 $p/p_0$ again in line with the continuing strong increase in water uptake for LiCl after the second step. For LiCl@UiO-66_9 the water uptake reaches a plateau between $0.25 < p/p_0 < 0.45$ and the increase in uptake is assumed above 0.5 $p/p_0$. Evidently, the water uptake of UiO-66-based CSPMs is greatly enhanced over the

whole relative pressure ($p/p_0$) range in comparison with neat UiO-66, demonstrating that LiCl is very effective in increasing the water uptake. In addition, it is known that the inorganic salts could be deposited on the external surface area of the matrix after the pores were completely filled. We have also prepared samples with a higher than 30 wt% amount of LiCl in the CSPM composites LiCl@UiO-66_36 (see Exp. section for details). However, this sample showed the deliquescence phenomenon after water sorption measurement, which is not desirable for AHT applications. Hence, we did not include a detailed analysis of these samples in the present work. Our samples with up to~30 wt% amount of LiCl in the CSPM did not show a deliquescence phenomenon even after repeated water sorption measurements, which was supported by the optical microscopy images of LiCl@UiO-66_30 (Fig. S7, ESI†). It could be expected that the pore structure of the metal-organic framework could efficiently prevent the confined inorganic salt from leaching out, due to the limited ability of water uptake to achieve dissolution.

To visualize the water vapor uptake in detail, only the adsorption isotherm parts in the range $0 < p/p_0 < 0.3$ were plotted (Fig. 4b). The three LiCl@UiO-66_x (x=9, 19, 30) CSPMs are more hydrophilic than neat UiO-66 at the initial relative pressure. LiCl@UiO-66_30 assumes the character of pure LiCl and has a slightly weaker uptake of water molecules than LiCl@UiO-66_19 in the low-pressure region up to $p/p_0 < 0.05$. This may be due to a faster uptake in the less congested pores of LiCl@UiO-66_19 while the higher loaded LiCl@UiO-66_30 would need more time to reach the equilibrium pore filling especially at low pressure. The thermodynamic equilibrium is not necessarily reached in the volumetric adsorption measurement if the set pressure difference criteria (albeit set to the lowest possible value) advance the measurement to the next data point. Above $p/p_0 = 0.15$ the higher amount of LiCl incorporated in the micropores of UiO-66 also leads to an increased water vapor uptake. The water amounts adsorbed at $p/p_0 = 0.3$ reached 0.34 g/g, 0.45 g/g, 0.60 g/g, respectively, which is much

higher than for neat UiO-66 (0.18 g/g) (Table 3, Fig. 5). Remarkably the LiCl incorporation increases the water uptake capacity of UiO-66 from 0.18 to 0.60 at $p/p_0$ = 0.3. The water vapor uptakes measured volumetrically for UiO-66 and the three LiCl@UiO-66_x composites are consistent with the results from the gravimetric measurement (at 0.9 $p/p_0$, Table 3).

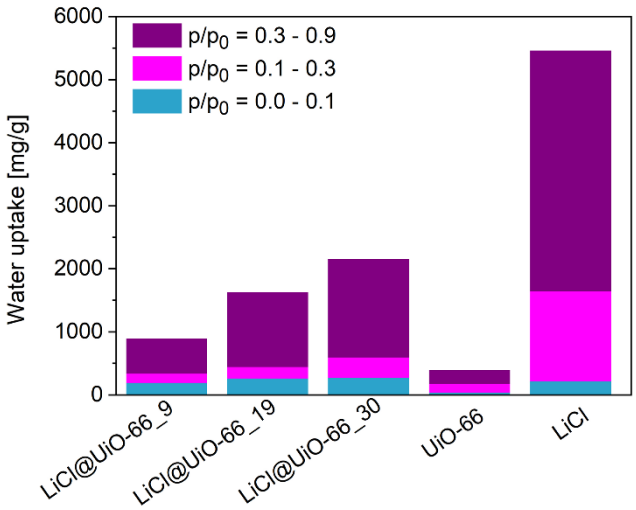


**Fig. 5** The water capacity of neat UiO-66, the pure LiCl and the three composites LiCl@UiO-66_x (x=9, 19, 30). From repeated and reproducible volumetric water vapor sorption isotherms the variance of the water uptake values is around 5%.

In order to evaluate the cycling stability of the CSPMs, the samples were tested gravimetrically by alternatingly exposing the samples to a relative humidity of 90% and 0% (Fig. 6). Like UiO-66, none of the LiCl@UiO-66_x CSPMs shows a visible loss in water uptake. The deviation is –3%, –1% and –4% only (for x = 9, 19, 30, respectively) after 10 adsorption-desorption cycles compared to the first cycle, which is still within experimental error and the variation seen over the 10 cycles. More cycling experiments were performed under a relative humidity of 80% and 20% (Fig. S8, ESI†) to confirm the stability under practical engineering applications, as a relative humidity of 0% is hardly achieved in a practical device. Over 40 cycles only a slight fluctuation around the equilibrium uptake was observed, which is within the experimental error and caused of the balance drift, but there was no decrease in uptake. In conclusion, the CSPM materials can be viewed as stable towards cyclic water adsorption and desorption within

the test procedure and should also be stable under application related conditions. Thus, the superior stability and higher uptake capacity of UiO-66-based CSPMs provides a practical value towards adsorption heat pump application.

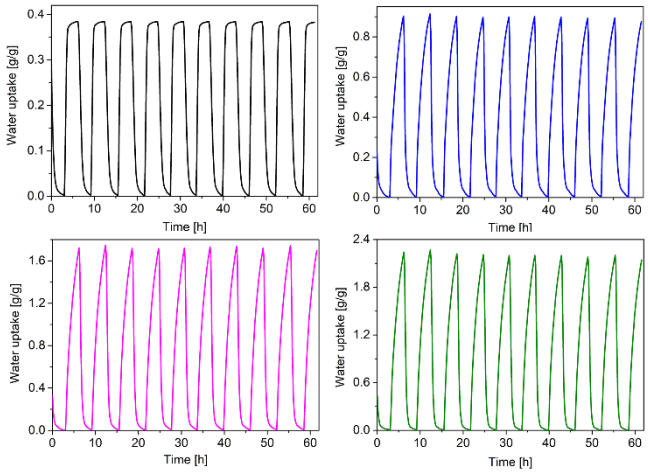


**Fig. 6** Gravimetric adsorption and desorption cycles of UiO-66 (black) and the CSPMs LiCl@UiO-66_x, x= 9 (blue), 19 (pink), 30 (green) curve. The gravimetric multi-cycle tests were carried out between a relative humidity of 90% and 0% under a maximum equilibration time of 3 hours.

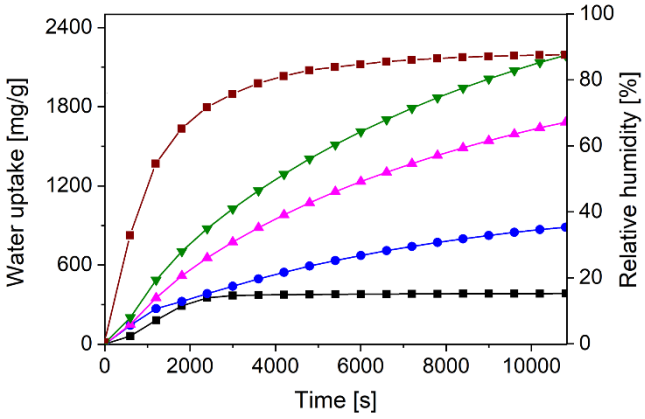


**Fig. 7** Gravimetric water sorption measurements of UiO-66 (black) and the CSPMs LiCl@UiO-66_x, x= 9 (blue), 19 (pink), 30 (green) curve at 20 °C in comparison to the kinetics curve to reach a set target relative humidity of 90% in the chamber (wine red).

## Kinetic study

While for adsorption heat pump applications the specific vapor uptake is of primary importance, adsorption kinetics has also to be taken into consideration and is often overlooked. Fig. 7 shows that dynamic water sorption of uptake over time has a short

induction period of ~500 s, followed by a fast uptake section and a slow-down as the amount of adsorbed water vapor gradually reaches saturation. The induction period can be best seen for the pristine MOF and the two _19 and _30 composites in the range from 0 to ~500 seconds. The slope in this time period is not as steep as that of the curves between ~500 to ~1500 seconds. The induction period is mainly caused by the still low relative humidity in the device chamber. The increase in adsorbed water quantity is intimately related to the amount of impregnated salt. The gravimetric water uptake over time of the pristine UiO-66 and three LiCl@UiO-66_x composites were fitted well with a pseudo-first order model (Eq. (1), Table 4, Fig. S9, ESI†).

$$q_t = q_e(1 - e^{-kt}) \qquad (1)$$

Here, $q_e$ stands for the equilibrium water sorption quantity (mg/g), $q_t$ stands for the dynamic water sorption quantity (mg/g), $k$ stands for the rate coefficient ($s^{-1}$) and $t$ for time (s). It can be seen from Table 4 that the kinetics of water sorption for the host matrix UiO-66 is faster than that for CSPM adsorbents. UiO-66 reaches saturation, that is, the equilibrium water uptake much faster (after about 3000 s) than the CSPMs which need over 10000 s. This is caused by the increased diffusion resistance due to the hygroscopic salt incorporated into the matrix pores.[51] The CSPMs adsorb a larger amount of water vapor compared to UiO-66 due to the added affinity of LiCl. Yet, the amount of larger pores which enable a faster diffusion has decreased in the composites (cf. Fig. 3b). Therefore, a longer time is required to reach a saturated or equilibrium adsorption amount, which leads to a lower adsorption rate coefficient of the composite salt compared to the pristine material. Similarly, Teo et al. showed that the adsorption rate coefficient of 5% Li(Na) incorporated MIL-101(Cr) is slower than that of pristine MIL-101(Cr).[21]

**Table 4** Kinetic parameters from gravimetric water sorption over time.[a]

| | $q_e$ (mg/g) | k (1/s) | $R^2$ |
|---|---|---|---|
| UiO-66 | 390(8) | $6.7(6) \times 10^{-4}$ | 0.9620 |
| LiCl@UiO-66_9 | 985(24) | $2.0(1) \times 10^{-4}$ | 0.9905 |
| LiCl@UiO-66_19 | 2056(23) | $1.54(3) \times 10^{-4}$ | 0.9994 |
| LiCl@UiO-66_30 | 2619(36) | $1.62(4) \times 10^{-4}$ | 0.9990 |

[a] Obtained from fitting the gravimetric measurement with Eq. (1) (cf. Fig. 7 and Fig. S9, ESI†). Standard deviations are given in parentheses.

For CSPM, the adsorption rate coefficient decreased from LiCl@UiO-66_9 with the increasing incorporated amount of LiCl to LiCl@UiO-66_19 and 30, which have a similar rate coefficient. Still, the adsorption rate coefficient of CSPM in this work is higher than for silica gel impregnated with LiCl, LiBr and $CaCl_2$, where $k$ ranges from $9.03 \times 10^{-5}$ $s^{-1}$ to $1.49 \times 10^{-4}$ $s^{-1}$.[52] From Eq. (1), the calculated equilibrium (saturation) water sorption quantity $q_e$ (for an infinite time at 90% rel. humidity) for pristine UiO-66 and three CSPMs is 390 mg/g, 985 mg/g, 2056 mg/g and 2619 mg/g (Table 4). For neat UiO-66 this $q_e$ value compares well with the volumetric water uptake of 393 mg/g at $p/p_0 = 0.9$ (Table 3) but $q_e$ is increasingly higher than the volumetric water uptake at $p/p_0 = 0.9$ with higher salt content. For LiCl@UiO-66_30 $q_e$ is 2619 mg/g while the volumetric water uptake at $p/p_0 = 0.9$ was only 2153 mg/g (Table 3). This can indicate that the volumetric uptake was not in full equilibrium. For very slow uptakes with decreasingly small pressure differences over time, the set measurement boundary conditions will advance the automatic sorption analyzer to the next data point before full equilibrium was reached.

## Coefficient of performance (COP)

COP is a commonly adopted indicator of the thermodynamic efficiency of the cycling process and depends strongly on the operating conditions. COP is determined as useful energy output divided by the required energy as input,[1] which for the heating model ($COP_H$) is given by Eq. (2) with heat from condensation ($Q_{cond}$) and heat of adsorption ($Q_{ads}$).

$$COP_H = \frac{-(Q_{con} + Q_{ads})}{Q_{regen}} \qquad (2)$$

The $COP_H$ values can range from 1 to 2.[1] The higher the $COP_H$ values, the better the energetic efficiency for the heating mode. The volumetric adsorption data were fitted using with the Dubinin-Astakhov approach, which is quite common for water@zeolite-systems.[36,37,53] As conditions for a heat pump an evaporator (cold) temperature of 10 °C, a heating or adsorption temperature of 40°C and a driving (desorption) temperature of 90 °C was used. This leads to a $COP_H$ of 1.64 for LiCl@UiO-66_30 (see details, in ESI†).

In other work, the coefficient of performance (given in parentheses) for CAU-10 (1.15-1.3) and SAPO-34 (1.35-1.6) under the desorption temperature ranging from 80 °C-120°C was lower than 1.64, and only MIL-160 showed a slightly higher COP value of 1.67 than LiCl@UiO-66_30 (1.64) when a desorption temperature higher than 100 °C was applied (Table 5).[54] Also, the COP value was lower for MOF-801(Zr) (1-1.58) and benchmark AQSOA-Z02 (1.35-1.6) with water as working pair, MIL-53(Cr) (1-1.52), $Zn(BDC)(DABCO)_{0.5}$ (1-1.55) and activated carbon (1-1.51) with methanol as working pair under desorption temperatures ranging from 80 °C-120 °C.[1] For the adsorbent-adsorbate pairs such as MIL-101-methanol, SG/LiBr-methanol, CAU-3-ethanol, Maxsorb III-ethanol, and AX-21-ammonia, the $COP_H$ ranged only from1.0 to 1.2.[55] For salt@silica gel SWS composites, the COP value for SWS-1S (1.1-1.4) was lower than 1.64, and the highest COP value for SWS-2L(57) (1.2-1.65) was close to LiCl@UiO-66_30 (1.64), however, the desorption temperature was in the range of 125-150 °C (Table 5).[56] Thus, LiCl@UiO-66_30 (1.64) is promising for its high COP value and a relatively low desorption temperature for regeneration.

**Table 5** Coefficients of performance ($COP_H$) for comparative materials.

| Compound | adsorbate | Working condition, °C ($T_{evap.}/T_{ads.}/T_{des.}$) | $COP_H$ | Ref. |
|---|---|---|---|---|
| LiCl@UiO-66_30 | water | 10/40/90 | 1.64 | This work |
| CAU-10 | water | 15/45/80-120 | 1.15-1.3 | 54 |
| SAPO-34 | water | 15/45/80-120 | 1.35-1.6 | 54 |
| MIL-160 | water | 15/45/80-120 | 1.2-1.67 | 54 |
| MOF-801(Zr) | water | 15/45/80-120 | 1-1.58 | 1 |
| benchmark AQSOA-Z02 | water | 15/45/80-120 | 1.35-1.6 | 1 |
| MIL-53(Cr) | methanol | 15/45/80-120 | 1-1.52 | 1 |
| $Zn(BDC)(DABCO)_{0.5}$ | methanol | 15/45/80-120 | 1-1.55 | 1 |
| activated carbon | methanol | 15/45/80-120 | 1-1.51 | 1 |
| MIL-101 | methanol | -23/50/140-190 | 1-1.21 | 55 |
| Silica/LiBr | methanol | -23/50/140-190 | 1-1.11 | 55 |
| CAU-3 | ethanol | -23/50/140-180 | 1-1.07 | 55 |
| Maxsorb III | ethanol | -23/50/140-180 | 1-1.11 | 55 |
| AX-21(active carbon) | ammonia | -23/50/140-190 | 1-1.18 | 55 |
| SWS-1S [a] | water | 7/55/100-135 | 1.1-1.4 | 56 |
| SWS-2L(57) [b] | water | 7/55/125-150 | 1.2-1.65 | 56 |

[a] SWS-1S refers to a silica gel with average pore radius of 1.8 nm filled with 21.7% $CaCl_2$. [b] SWS-2L(57) refers to a silica gel with average pore radius of 7.5 nm filled with 57% LiBr.

## Thermal batteries applications

Adsorption-based thermal batteries (ATBs) have been recently introduced as an alternative storage device to improve the usability of discontinuously supplied low-grade energy for heating and cooling. The process is based on cyclic adsorption and desorption of a working fluid on a porous material (Scheme 1). ATBs make use of heat on different temperature levels such as thermal solar energy or industrial waste heat as the regeneration energy instead of electricity or fossil fuels.[57,58]

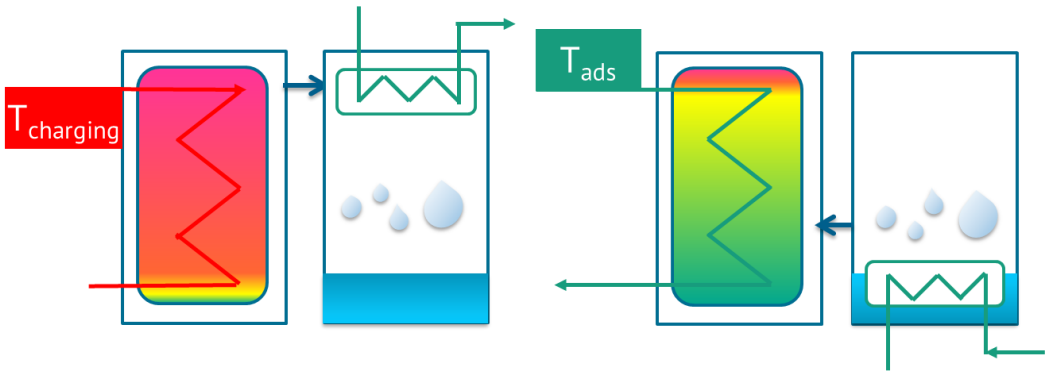

(a) Charging (b) Discharging

**Scheme 1** Schematic working principle of an adsorption-based thermal battery (ATB). To charge the thermal battery (a), heat on a high temperature level has to be applied and the working fluid (e.g., water) has to be collected in a storage using a condenser. The battery can then be discharged (b) by evaporating the working fluid leading to its adsorption. Thereby the ATB can be used for heating by making use of the heat of adsorption as well as for cooling by using the heat of evaporation drawn from the environment.

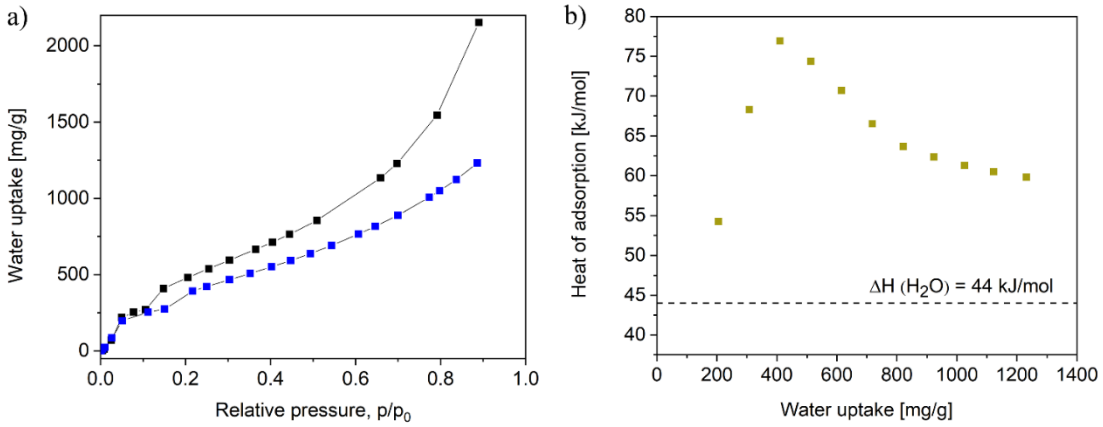


**Fig. 8** a) Water sorption isotherms of LiCl@UiO-66_30 at 293 K (black) and 303 K (blue). b) Heat of adsorption LiCl@UiO-66_30. Straight dashed line is the heat of evaporation of water with 44 kJ/mol at 298 K.

Following the work of Garzón-Tovar and co-workers,[29] we chose the working capacity at low relative pressures ($p/p_0 = 0 – 0.1$) being desirable to diminish the requirement of a compressor. Thus, the efficiency of a thermal battery is directly proportional to the working capacity at $p/p_0 = 0.1$ (Table 3, Fig. 5). LiCl@UiO-66_30 has a high-water capacity of 271 mg/g at $p/p_0 = 0.1$. The isosteric heat of adsorption for LiCl@UiO-66_30 was calculated using water sorption isotherms (Fig. 8a) from two different temperatures (293 K and 303 K) by applying the Clausius-Clapeyron equation (Eq. 3). The heat of adsorption rises initially, goes through a maximum at a water uptake of 0.4 g/g, which coincides with the inflection point in the second uptake step in the volumetric adsorption isotherm (Fig. 4b, Fig. 8a) and then declines gradually with increasing water loading (Fig. 8b). It was found that $\Delta H_{ads}$ for a working capacity ($\Delta w$)

of 271 mg/g (at $p/p_0 = 0.1$) was about 60 kJ/mol. The heat storage capacity ($C_{HS}$) was estimated according to Eq. 4.

$$\Delta H_{ads} = -R \cdot ln\left(\frac{P_2}{P_1}\right)\frac{T_1 \cdot T_2}{T_2 - T_1} \qquad (3)$$

$$C_{HS} = \frac{\Delta H_{ads} \cdot \Delta\omega}{M_W} \qquad (4)$$

Where $M_w$ is the molecular mass of water. The heat storage capacity ($C_{HS}$) for LiCl@UiO-66_30 was calculated to 900 kJ/kg (= 0.25 kWh/kg), which outperforms $CaCl_2$@UiO-66_38 with a $C_{HS}$ value of 367 kJ/kg.[29] According to the U.S. Department of Energy (DOE),[59] the minimum heat storage capacity for ATBs should be 2.5 kWh with the condition of the maximum weight of the heat exchanger system of 35 kg. To achieve the targeted minimum heat storage capacity, only 10 kg of LiCl@UiO-66_30 would be needed. This makes LiCl@UiO-66_30 a promising candidate applicable in adsorption-based thermal batteries.

## Conclusions

MOF-based composites of 'salt inside porous matrix' with LiCl@UiO-66 were fabricated by a facile post-modification wet-impregnation method. Thorough characterization by AAS, ICP-OES, PXRD, $N_2$ sorption with BET analysis and SEM/EDX in comparison to neat UiO-66 confirm the incorporation of LiCl inside the MOF. Not only the water uptake capacity of LiCl@UiO-66 significantly increased over neat UiO-66, but an analysis of the water vapor sorption isotherms also shows at $p/p_0 = 0.1$ a hydration state of LiCl inside the MOF which is much higher than for neat LiCl. This is traced to the dispersion of small LiCl clusters with their high surface energy in the porous matrix. A kinetic analysis of the water uptake from a gravimetric

measurement over time reveals the expected slower adsorption in LiCl@UiO-66 over neat UiO-66 due to pore blocking effects. More importantly, this kinetic analysis also suggests that the volumetric water sorption measurements have not reached full equilibrium, lacking for example an uptake of over 400 mg/g for LiCl@UiO-66_30 at $p/p_0 = 0.9$ due to instrument artefacts. The high-water adsorption amount of LiCl@UiO-66_30 of 271 mg/g at $p/p_0 = 0.1$ coincides with a heat storage capacity of 900 kJ $kg^{-1}$, which makes this hydrothermally stable composite readily applicable in thermal batteries and adsorption heat pumps. As a vision for future work, we believe that a matrix with a larger pore size could not only increase the loading of inorganic salts but also the uptake kinetics. On the premise of ensuring no deliquescence, we plan to test if the optimal loading of inorganic salts inside matrix possessing a larger pore size could then yield promote a better performance in practical applications.

## Conflicts of interest

There are no conflicts to declare.

## Acknowledgements

The authors thank Dr. Jun Liang for helpful discussion. We thank China Scholarship Council (CSC) for funding a PhD fellowship to Y.Y.S.

## References

1 M. F. de Lange, K. J. Verouden, T. J. Vlugt, J. Gascon and F. Kapteijn, *Chem. Rev.*, 2015, **115**, 12205-12250.

2 E. Hastürk, S.-J. Ernst and C. Janiak, *Curr. Opin. Chem. Eng.*, 2019, **24**, 26-36.

3 F. Jeremias, D. Fröhlich, C. Janiak and S. K. Henninger, New J. Chem., 2014, **38**, 1846-1852.

4 Y. I. Aristov, *Appl. Therm. Eng.*, 2013, **50**, 1610-1618.

5 K. C. Ng, H. T. Chua, C. Y. Chung, C. H. Loke, T. Kashiwagi, A. Akisawa and B. B. Saha, *Appl. Therm. Eng.*, 2001, **21**, 1631-1642.

6 T. Kawano, M. Kubota, M. S. Onyango, F. Watanabe and H. Matsuda, *Appl. Therm. Eng*., 2008, **28**, 865-871.

7 M. Kubota, T. Ito, F. Watanabe and H. Matsuda, *Appl. Therm. Eng.,* 2011, **31**, 1495-1498.

8 J.-P. Zhang, A.-X. Zhu, R.-B. Lin, X.-L. Qi and X.-M. Chen, *Adv. Mater.*, 2011, **23**, 1268-1271.

9 Ristić, N. Z. Logar, S. K. Henninger and V. Kaučič, *Adv. Funct.* Mater., 2012, **22**, 1952-1957.

10 Krajnc, J. Varlec, M. Mazaj, A. Ristić, N. Z. Logar and G. Mali, *Adv. Energy Mater.*, 2017, **7**, 1601815.

11 S. K. Henninger, F. Jeremias, H. Kummer and C. Janiak, *Eur. J. Inorg. Chem.*, 2012, **2012**, 2625-2634.

12 M. J. Kalmutzki, C. S. Diercks and O. M. Yaghi, *Adv. Mater.*, 2018, **30**, 1704304.

13 S. Kayal, A. Chakraborty and H. W. B. Teo, *Mater. Lett.*, 2018, **221**, 165-167.

14 N. Tannert, S.-J. Ernst, C. Jansen, H.-J. Bart, S. K. Henninger and C. Janiak, *J. Mater. Chem. A*, 2018, **6**, 17706-17712.

15 F. Jeremias, A. Khutia, S. K. Henninger and C. Janiak, *J. Mater. Chem.*, 2012, **22**, 10148-10151.

16 J. Canivet, A. Fateeva, Y. Guo, B. Coasne and D. Farrusseng, *Chem. Soc. Rev*., 2014, **43**, 5594-5617.

17 D. Lenzen, J. Zhao, S. J. Ernst, M. Wahiduzzaman, A. Ken Inge, D. Frohlich, H. Xu, H. J. Bart, C. Janiak, S. Henninger, G. Maurin, X. Zou and N. Stock, *Nat. Commun.*, 2019, **10**, 3025-3034.

18 Schlüsener, M. Xhinovci, S.-J. Ernst, A. Schmitz, N. Tannert and C. Janiak, *Chem. Mater.*, 2019, **31**, 4051-4062.

19 N. Ko, P. G. Choi, J. Hong, M. Yeo, S. Sung, K. E. Cordova, H. J. Park, J. K. Yang and J. Kim, *J. Mater. Chem. A*, 2015, **3**, 2057-2064.

20 M. Wickenheisser, F. Jeremias, S. K. Henninger and C. Janiak, *Inorg. Chim. Acta*, 2013, **407**, 145-152.

21 H. W. B. Teo, A. Chakraborty and S. Kayal, *Appl. Therm. Eng.*, 2017, **120**, 453-462.

22 X. Zheng and R. Wang, *Int. J. Refrig.*, 2019, **98**, 452-458.

23 J. Xu, T. Li, J. Chao, S. Wu, T. Yan, W. Li, B. Cao and R. Wang, *Angew. Chem. Int. Ed.,* 2020, **59**, 5202-5210.

24 L. G. Gordeeva and Y. I. Aristov, *Int. J. Low-Carbon Technol.*, 2012, **7**, 288-302.

25 Yu. I. Aristov, An optimal sorbent for adsorption heat pumps: thermodynamic requirements and molecular design in *Proc. VI Minsk International Seminar 'Heat Pipes, Heat Pumps, Refrigerators'*, Minsk, 12–15 September, 2005, 342–353.

26 Yu. I. Aristov, M. M. Tokarev, G. Cacciola and G. Restuccia, *React. Kinet. Cat. Lett.*, 1996, **59**, 325–334.

27 Y. N. Zhang, R. Z. Wang and T. X. Li, *Energy*, 2018, **156**, 240-249.

28 K. Bourikas, C. Kordulis and A. Lycourghiotis, *Catal. Rev.*, 2006, **48**, 363-444.

29 L. Garzón-Tovar, J. Pérez-Carvajal, I. Imaz and D. Maspoch, *Adv. Funct. Mater.*, 2017, **27**, 1606424.

30 Permyakova, S. Wang, E. Courbon, F. Nouar, N. Heymans, P. D'Ans, N. Barrier, P. Billemont, G. De Weireld, N. Steunou, M. Frère and C. Serre, *J. Mater. Chem. A*, 2017, **5**, 12889-12898.

31 Tan, Y. Luo, X. Liang, S. Wang, X. Gao, Z. Zhang and Y. Fang, *Micropor. Mesopor. Mat.*, 2019, **286**, 141-148.

32 K. Leus, T. Bogaerts, J. De Decker, H. Depauw, K. Hendrickx, H. Vrielinck, V. Van Speybroeck, and P. Van Der Voort, *Micropor. Mesopor. Mater.*, 2016, **226**, 110-116.

33 L. Hu, T. Ge, Y. Jiang and R. Wang. *Int. J. Refrig.*, 2014, **35**, 69-75.

34 J. H. Cavka, S. Jakobsen, U. Olsbye, N. Guillou, C. Lamberti, S. Bordiga and K. P. Lillerud, *J. Am. Chem. Soc.*, 2008, **130**, 13850-13851.

35 N. Truong, J. Park, O. K. Kwon and I. Park, *Mater. Lett.*, 2018, **215**, 137-139.

36 L. X. Gong, R. Z. Wang, Z. Z. Xia and C. J. Chen, *J. Chem. Eng. Data*, 2010, **55**, 2920-2923.

37 K. Daou, R. Z. Wang and Z. Z. Xia, *Appl. Therm. Eng.*, 2006, **26**, 56-65.

38 Y. Ban, Z. Li, Y. Li, Y. Peng, H. Jin, W. Jiao, A. Guo, P. Wang, Q. Yang, C. Zhong and W. Yang, *Angew. Chem. Int. Ed.*, 2015, **54**, 15483-15487

39 G. Férey, C. Mellot-Draznieks, C. Serre, F. Millange, J. Dutour, S. Surblé and I. Margiolaki, *Science*, 2005, **309**, 2040-2042.

40 S. Øien, D. Wragg, H. Reinsch, S. Svelle, S. Bordiga, C. Lamberti and K. P. Lillerud, *Cryst. Growth Des.*, 2014, **14**, 5370-5372.

41 S. Muto and K. Tatsumi, *Microscopy*, 2016, **66**, 39-49.

42 G. C. Shearer, S. Chavan, S. Bordiga, S. Svelle, U. Olsbye and K. P. Lillerud, *Chem. Mater.*, 2016, **28**, 3749-3761.

43 S. Yuan, J. S. Qin, C. T. Lollar and H. C. Zhou, *ACS Cent. Sci.*, 2018, **4**, 440-450.

44 M. Thommes, K. Kaneko, A. V. Neimark, J. P. Olivier, F. Rodriguez-Reinoso, J. Rouquerol and K. S. W. Sing, *Pure Appl. Chem.*, 2015, **87**, 1051-1069.

45 M. Kim and S. M. Cohen, *CrystEngComm*, 2012, **14**, 4096-4104.

46 Q. Yang, A. D. Wiersum, P. L. Llewellyn, V. Guillerm, C. Serre and G. Maurin, *Chem. Commun.*, 2011, **47**, 9603-9605.

47 M. Taddei, *Coord. Chem. Rev.*, 2017, **343**, 1-24.

48 A. Clark, K. N. Heck, C. D. Powell and M. S. Wong, *ACS Sust. Chem. Eng.*, 2019, **7**, 6619-6628.

49 B. Bueken, N. Van Velthoven, A. Krajnc, S. Smolders, F. Taulelle, C. Mellot-Draznieks, G. Mali, T. D. Bennett and D. De Vos, *Chem. Mater.*, 2017, **29**, 10478-10486.

50 Kuznik, Energy Storage by Adsorption Technology for Building. In: R. Wang and X. Zhai (eds) Handbook of Energy Systems in Green Buildings. Springer, Berlin, Heidelberg. 2018, DOI: 10.1007/978-3-662-49120-1_42, pp. 1025-1051.

51 B. Dawoud and Y. Aristov, *Int. J. Heat Mass Transfer*, 2003, **46**, 273-281.

52 X. Zheng, T. S. Ge, R. Z. Wang and L. M. Hu, *Chem. Eng. Sci.*, 2014, **120**, 1-9.

53 S.-J. Ernst, F. Jeremias, H.-J. Bart and S. K. Henninger, *Ind. Eng. Chem. Res.*, 2016, **55**, 13094-13101.

54 Cadiau, J. S. Lee, D. Damasceno Borges, P. Fabry, T. Devic, M. T. Wharmby, C. Martineau, D. Foucher, F. Taulelle, C.-H. Jun, Y. K. Hwang, N. Stock, M. F. De Lange, F. Kapteijn, J. Gascon, G. Maurin, J.-S. Chang and C. Serre, *Adv. Mater.*, 2015, **27**, 4775-4780.

55 D. B. Boman, D. C. Hoysall, D. G. Pahinkar, M. J. Ponkala and S. Garimella, *Appl. Therm. Eng.*, 2017, **123**, 422-434.

56 Y. I. Aristov, G. Restuccia, G. Cacciola and V. N. Parmon, *Appl. Therm. Eng.*, 2002, **22**, 191-204.

57 T. X. Li, R. Z. Wang and T. Yan, *Energy*, 2015, **84**, 745-758.

58 S. Girnik, A. D. Grekova, T. X. Li, R. Z. Wang, P. Dutta, S. S. Murthy and Y. I. Aristov, *Renew. Sustain. Energy Rev.*, 2020, **123**, 109748.

59 Advanced Research Projects Agency-DOE, HEATS Program Overview.https://arpa-e.energy.gov/sites/default/files/documents/files/HEATS_ProgramOverview.pdf (accessed Oct, 2016).

**Electronic Supporting Information (ESI)**

# Tunable LiCl@UiO-66 composites for water sorption-based heat transformation applications

Yangyang Sun,[a] Alex Spieß,[a] Christian Jansen,[a] Alexander Nuhnen,[a] Serkan Gökpinar,[a] Raphael Wiedey,[b] Sebastian-Johannes Ernst,[c] Christoph Janiak[a] *

[a] Institut für Anorganische Chemie und Strukturchemie, Heinrich-Heine-Universität Düsseldorf, 40204 Düsseldorf, Germany.

[b] Institut für Pharmazeutische Technologie und Biopharmazie, Heinrich-Heine-Universität Düsseldorf, 40204 Düsseldorf, Germany.

[c] Fraunhofer Institute for Solar Energy Systems (ISE), Heidenhofstr. 2, 79110 Freiburg, Germany.

Corresponding author: E-mail: janiak@uni-duesseldorf.de; Fax: + 49-211-81-12287; Tel: +49-211-81-12286

Additional email addresses:

Yangyang.Sun@uni-duesseldorf.de; alex.spiess@hhu.de; christian.jansen@hhu.de; alexander.nuhnen@uni-duesseldorf.de; serkan.goekpinar@uni-duesseldorf.de; mailto:raphael.wiedey@uni-duesseldorf.de; sebastian-johannes.ernst@ise.fraunhofer.de;

**Principle of heat transformation processes**

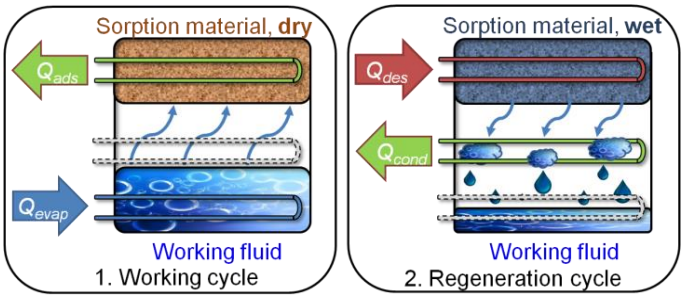


**Fig. S1** In the working cycle, a working fluid (favorably water due to its high evaporation enthalpy and nontoxicity) is evaporated at a low pressure, taking up evaporation heat $Q_{evap}$. During incorporation into a porous material, heat of adsorption $Q_{ads}$ is released. In the regeneration cycle, driving heat $Q_{des}$ for desorption is applied, and further condensation takes place at a medium temperature level and releases condensation heat $Q_{cond}$. Depending on the operation direction, the device can be used as a chiller or a heat pump. Adapted from ref.[1] with permission from The Royal Society of Chemistry, copyright 2012.

**Mechanism of water sorption for a CSPM**

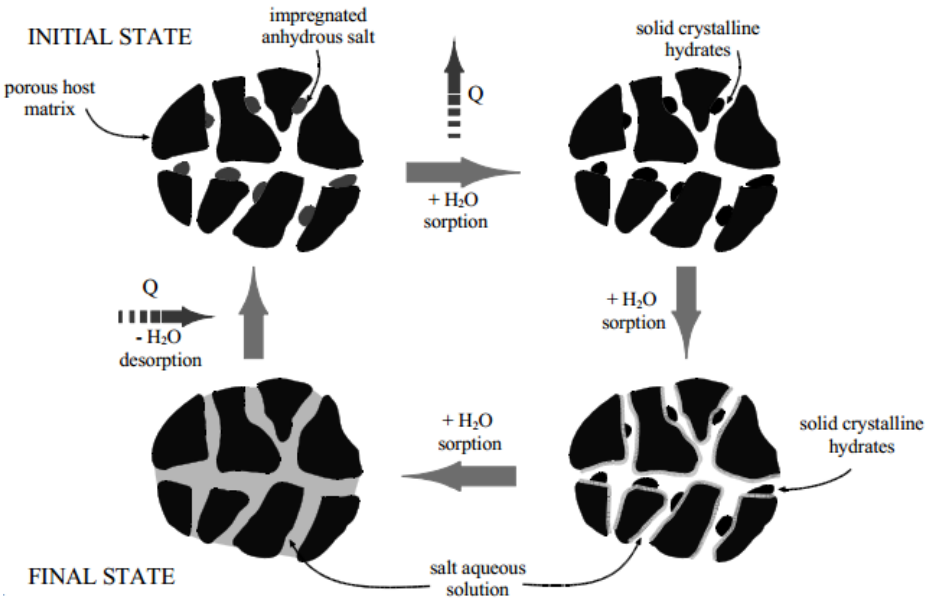


**Fig. S2** Schematic presentation of the mechanistic aspects of water sorption of composite salts inside porous matrix (CSPM). Reprinted from ref.[2]. Copyright *Proc. VI Minsk International Seminar 'Heat Pipes, Heat Pumps, Refrigerators'*, 2005.

**Experimental scheme**

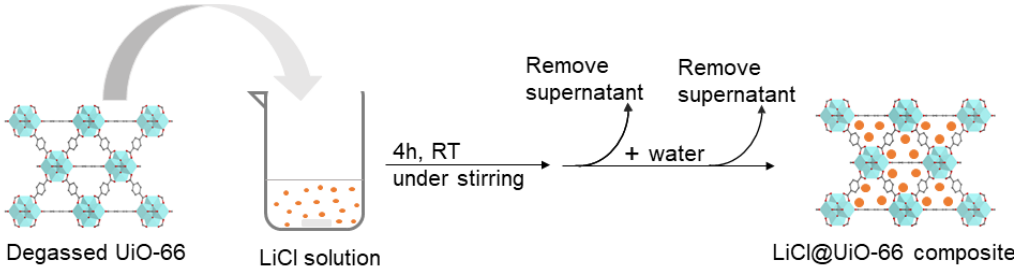


**Scheme S1** Pictorial presentation of the work-flow to prepare LiCl@UiO-66 composite (CSPM) samples.

**Solution preparation for atomic absorption spectroscopy (AAS)**

The composites were outgassed at 150 °C under vacuum (0.05 mbar) for 2 h. Then a chosen amount (around 5 mg) of each composite was weighed with high accuracy into a 1.5 mL centrifuge tube (Eppendorf tube) and around 20 mg of CsF was added. Then two drops (0.1 mL) of 12 mol/L HCl and 1 mL of water were added. The dispersions were left standing overnight to achieve complete degradation. At last, the solutions were transferred to a 50 mL volumetric flask and water was added to the mark.

The mass fraction of $m_{LiCl}/m_{CSPM}$ was calculated by Equations S1 and S2:

$$\mathbf{wt\%}(\boldsymbol{m_{LiCl}/m_{CSPM}}) = \frac{\boldsymbol{m_{LiCl}}}{\boldsymbol{m_{CSPM}}} = \frac{\boldsymbol{n_{LiCl}} \times \boldsymbol{M_{LiCl}}}{\boldsymbol{m_{CSPM}}} \qquad \text{S1}$$

$$\boldsymbol{n_{LiCl}} = \frac{\boldsymbol{c_{Li}} \times \boldsymbol{V}}{\boldsymbol{M_{Li}}} \qquad \text{S2}$$

where:

$m_{CSPM}$ refers to the used chosen mass of the CSPM composites. $c_{Li}$ refers to the concentration of Li (mg/L), which was obtained from AAS analysis. V is the volume of the measured solution (50 mL). $M_{Li}$ refers to the atomic mass of Li (6.941 g/mol). $M_{LiCl}$ refers to the molar mass of LiCl (42.394 g/mol).

**Scanning electron microscopy (SEM) and energy-dispersive X-ray spectroscopic (EDX) elemental mapping of CSPMs**

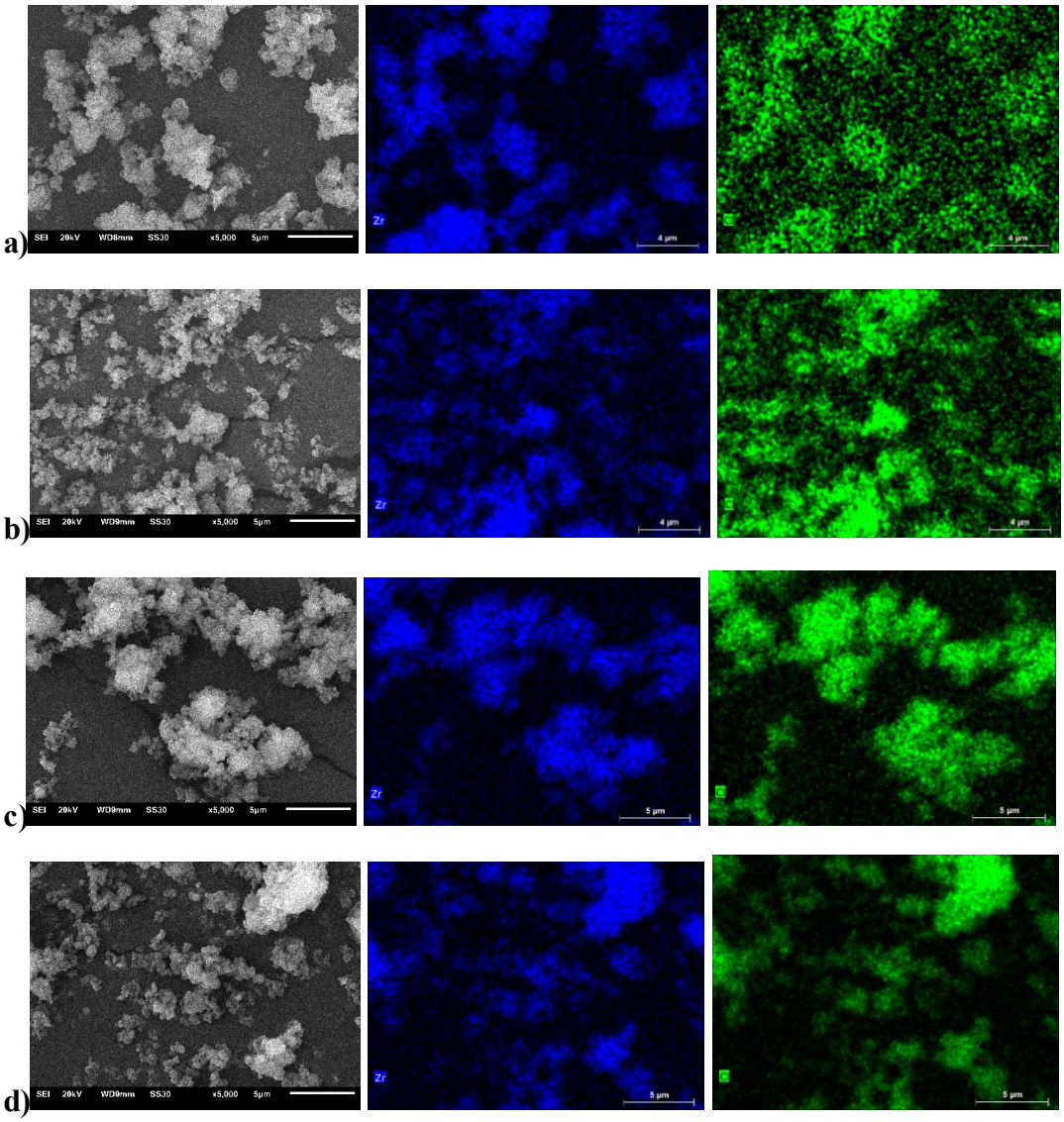


**Fig. S3** SEM and EDX elemental mapping of zirconium (blue) and chloride (green) in (a) UiO-66 and (b-d) LiCl@UiO-66_x (x = 9, 19, 30) (top to bottom).

**Determination of defects from thermogravimetric analysis (TGA)**

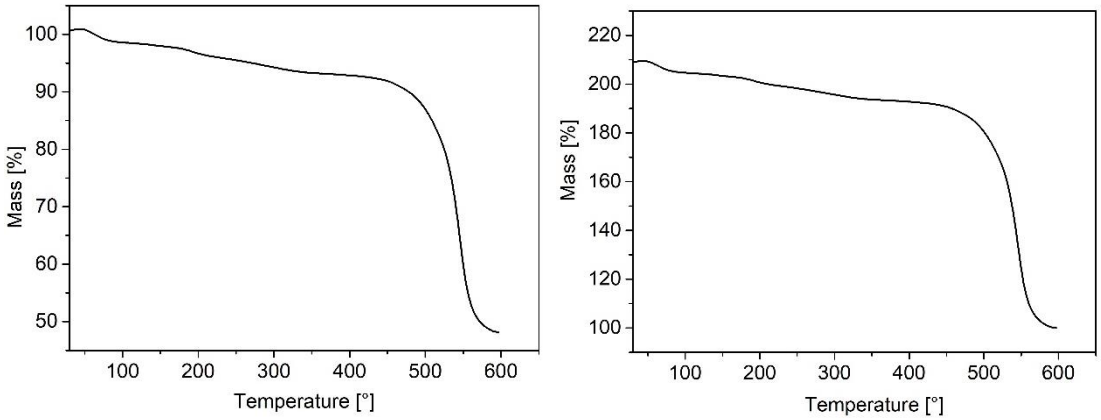


**Fig. S4** TGA of UiO-66: normalized such that the initial weight = 100% (left) and normalized such that the final weight = 100% (right).

The solvent residues are removed under temperatures of 100 ℃. The dehydroxylation of the $\{Zr_6O_4(OH)_4\}$ secondary building units (SBUs) appears in the temperature interval between 100 °C and 435 °C to yield $Zr_6O_6(BDC)_6$, followed by framework decomposition above 435 °C.

Determination of defects per SBU of UiO-66 was calculated with the assumption that the residue in TGA is pure $ZrO_2$ following the work of Shearer *et. al.*[3] The dehydroxylated ideal (defect-free) UiO-66 $Zr_6O_6(BDC)_6$ and its decomposition reaction would then be as follows:

$$Zr_6O_6(BDC)_6 + 45O_2 \rightarrow 6ZrO_2 + 48CO_2 + 12H_2O$$

The needed theoretical TGA plateau weight $W_{Theo.Plat.}$ and the theoretical weight contribution per BDC linker $Wt.PL_{Theo}$ was determined by Equation S3 and S4, respectively:

$$\boldsymbol{W_{Theo.Plat} = \left(\frac{M_{Comp.}}{M_{6\times ZrO2}}\right) \times W_{End}} \qquad \text{S3}$$

$$Wt.PL_{Theo} = \left(\frac{W_{Theo.Plat} - W_{End}}{NL_{Ideal}}\right) \qquad \text{S4}$$

where

$\mathbf{M_{Comp}}$ is the molar mass of dehydroxylated, defect-free UiO-66 [$Zr_6(\mu_3\text{-}O)(\mu_3\text{-}OH)_4(BDC)_6$] (1628.03 g/mol).

$\mathbf{M_{6xZrO2}}$ is the molar mass of 6 moles of zirconium oxide (739.34 g/mol)

$\mathbf{W_{End}}$ is the end weight of the TGA run (100 % as normalized in the right part of Figure S2).

$\mathbf{NL_{Ideal}}$ is the number of linkers (6) in the ***ideal*** $Zr_6$ formula unit.

As a result,

$\mathbf{W_{Theo.Plat}}$ for dehydroxylated UiO-66: $\mathbf{W_{Theo.Plat}}$ (UiO-66) = 220.20 %

$\mathbf{Wt.PL_{Theo}}$ (UiO-66) = (220.20 – 100)/6 = 20.03 %

The experimental number of linkers per ***defective*** $Zr_6$-SBU, $\mathbf{NL_{Exp}}$ can be determined by Eq. S5:

$$NL_{Exp.} = (6 - x) = \frac{(W_{Exp.Plat} - W_{End})}{Wt.PL_{Thero}} \qquad \text{S5}$$

where

$\mathbf{W_{Exp.Plat}}$ is the experimental TGA plateau and can be taken from the right part of Figure S2 ($\mathbf{W_{Exp.Plat}}$ = 192%).

**x** is the number of linker deficiencies per $Zr_6$ formula unit and can be determined by following equation:

$\mathbf{x = 6 - NL_{Exp} = 6 - [(W_{Exp.Plat} - W_{End})/Wt.PL_{Theo}]}$ = 6 – (192% – 100%)/20.03%

**x** = 1.4.

With **x** we obtain the experimental molecular weight Mw by using $\mathbf{Zr_6O_{6+x}(BDC)_{6-x}}$

Mw (UiO-66) = 1427.10 g/mol

**PXRD of recycled UiO-66 from LiCl@UiO-66_30**

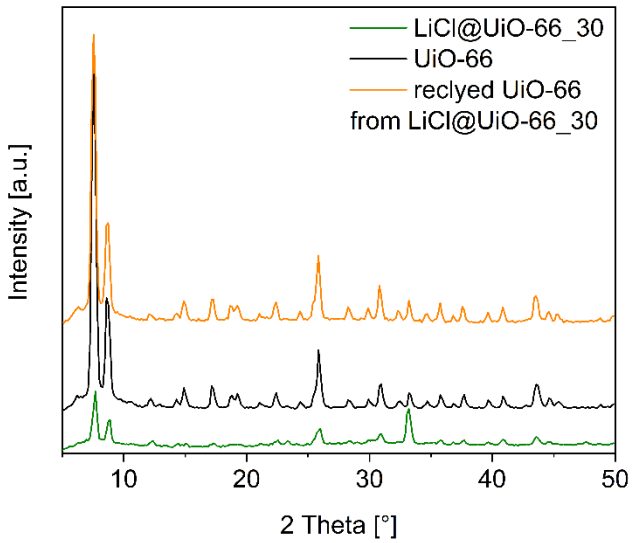


**Fig. S5** PXRD patterns of UiO-66, LiCl@UiO-66_30 and recycled UiO-66 from LiCl@UiO-66_30. Recycled UiO-66 was regained by immersing LiCl@UiO-66_30 into methanol for 12 hours.

**Water sorption isotherms**

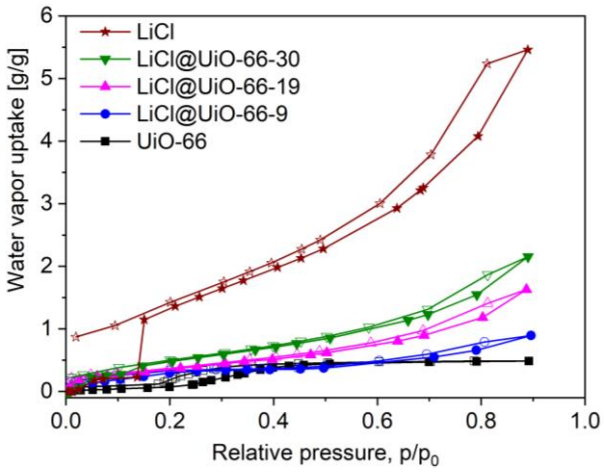


**Fig. S6** Water sorption isotherms of neat LiCl, UiO-66 and LiCl@UiO-66_x, x = 9, 19, 30.

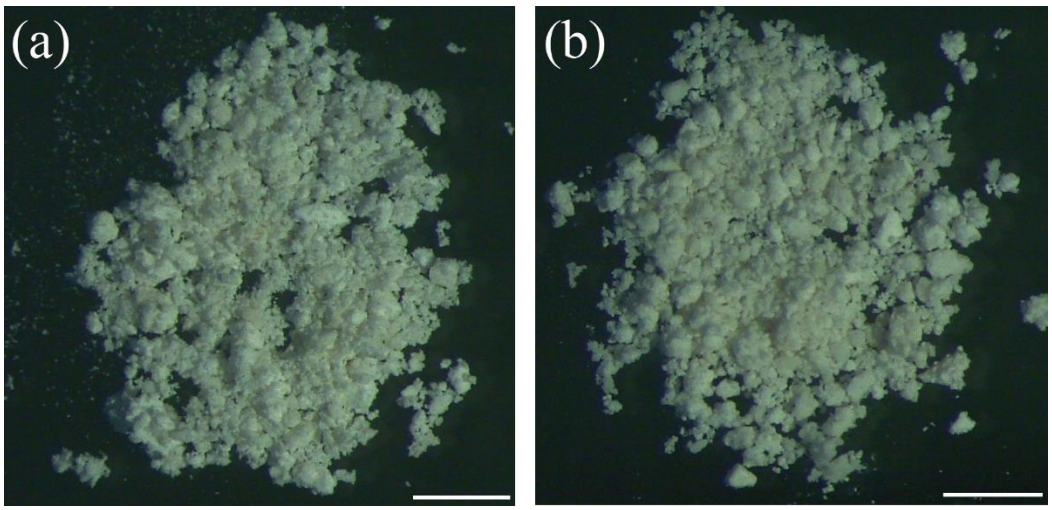


**Fig. S7** Optical microscopy images of LiCl@UiO-66_30 (a) before and (b) after repeated water sorption with no drying procedure. The scale bar in both images is 0.5 mm.

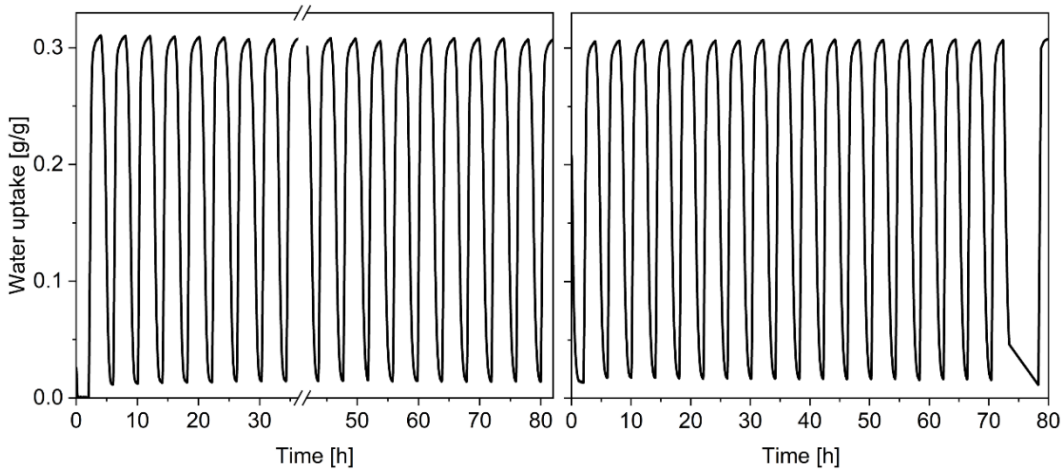
Water uptake [g/g]
0.0
0.1
0.2
0.3
0 10 20 30 50 60 70 80
Time [h]
0 10 20 30 40 50 60 70 80
Time [h]

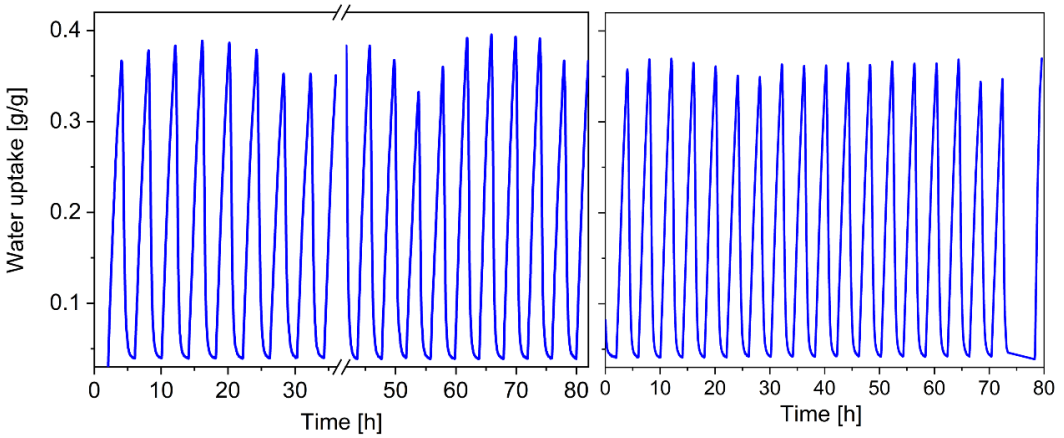
Water uptake [g/g]
0.1
0.2
0.3
0.4
0 10 20 30 50 60 70 80
Time [h]
0 10 20 30 40 50 60 70 80
Time [h]

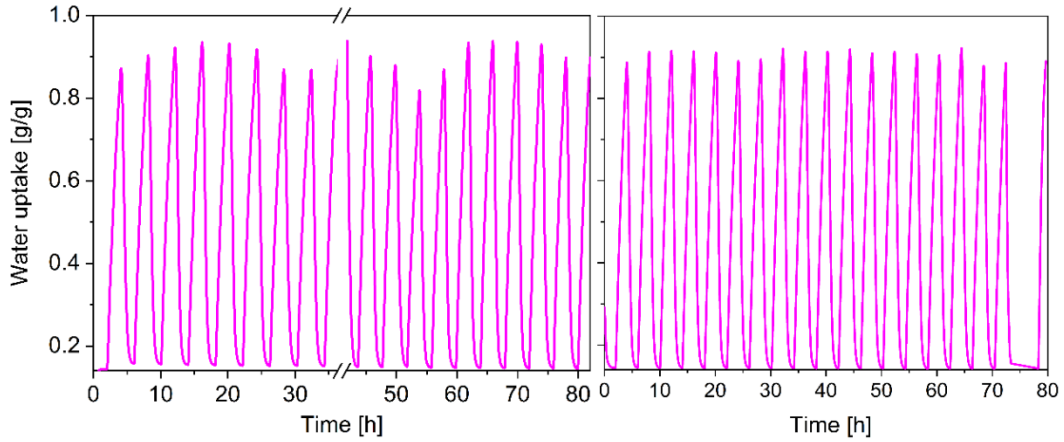
Water uptake [g/g]
0.2
0.4
0.6
0.8
1.0
0 10 20 30 50 60 70 80
Time [h]
0 10 20 30 40 50 60 70 80
Time [h]

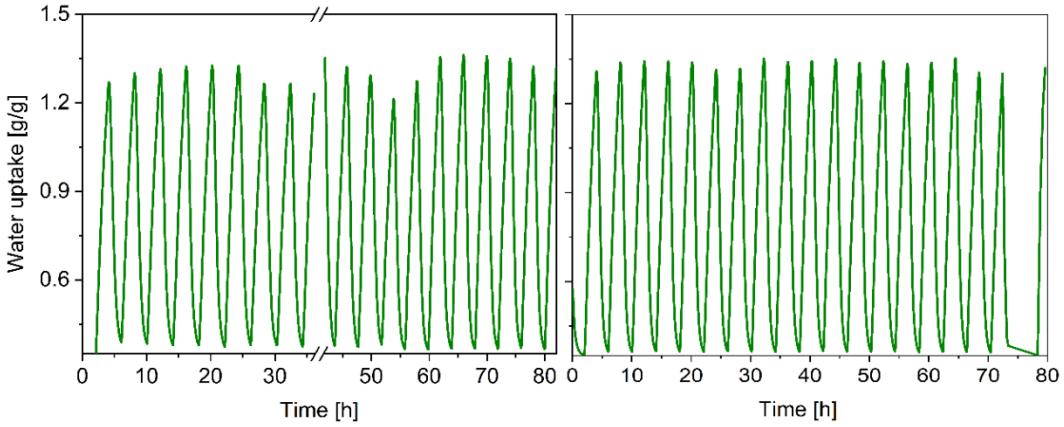
Water uptake [g/g]
0.6
0.9
1.2
1.5
0 10 20 30 50 60 70 80
Time [h]
0 10 20 30 40 50 60 70 80
Time [h]

**Fig S8** Gravimetric adsorption and desorption cycles of UiO-66 (black) and the CSPMs LiCl@UiO-66_x, x= 9 (blue), 19 (pink), 30 (green) curve for first (left) and second (right) 20 cycles. The gravimetric multi-cycle tests were carried out between a relative humidity of 80% and 20% under a maximum equilibration time of 2 hours. The maximal number of cycles for the device is 20. When the first 20 cycles were finished, the instrument was restarted for the second 20 cycles with the sample remaining in the instrument. The data from 36 h to 42 h was excluded, as the sorption analyzer did not reach the targeted relative humidity during these hours.

**Fitting curves for gravimetric water uptake over time**

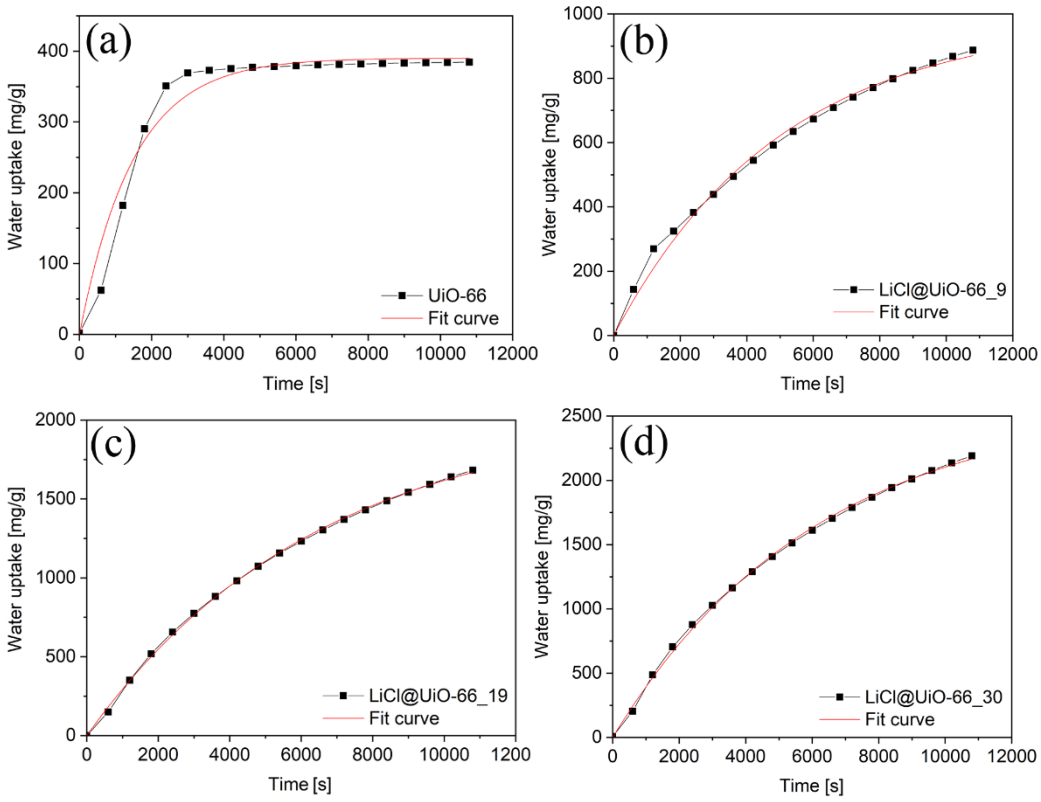


**Fig. S9** Gravimetric water sorption measurements of UiO-66 and the CSPMs LiCl@UiO-66_x, x = 9, 19, 30 at 20 °C with corresponding fit curves using the BoxLucas1 model in Origin.

**Coefficient of performance, COP calculation**

To assess the potential of the "salt@MOF" adsorbent in adsorption heat transformation, the measured water adsorption data were transformed to the following equation according to the Dubinin-Astakhov approach, which is quite common for water@zeolite-systems.[4,5]

$$W(A) = W_0 \exp[-(bA)^n] \qquad \text{S6}$$

This approach defines an adsorbed volume W as $W = X/\rho_{H2O(liquid)}$ and an adsorption potential A as $A = -RT\ln\frac{p}{p_S(T)}$. The coefficients $W_0$, b, and n were fitted to experimental data.[6]

The coefficient of performance (COP) can be defined as the ratio of usable heat to spent heat:

$$\mathrm{COP} = \frac{Q_{ads} + Q_{cond} + Q_{IC}}{Q_{des} + Q_{IH}} \qquad \text{S7}$$

Herein in the numerator the usable heat is summed up (heat of adsorption ($Q_{ads}$), heat from condensation ($Q_{cond}$) and the heat from isosteric cooling ($Q_{IC}$)). In the denominator the amounts of heat to apply for desorption ($Q_{des}$) and isosteric heating ($Q_{IH}$) of the adsorbent are summarized.

$$\mathrm{d}Q_{IH} = m_{ads}\left(c_{p,ads} + X_{max}c_{p,fl}\right)dT \qquad \text{S8}$$

$$\mathrm{d}Q_{des} = m_{ads}\left(c_{p,ads} + W(A)c_{p,fl}\right)dT - m_{ads}q_{st}(T)dX \qquad \text{S9}$$

$$\mathrm{d}Q_{IC} = m_{ads}\left(c_{p,ads} + X_{min}c_{p,fl}\right)dT \qquad \text{S10}$$

$$\mathrm{d}Q_{ads} = m_{ads}\left(c_{p,ads} + W(A)c_{p,fl}\right)dT - m_{ads}q_{st}(T)dX \qquad \text{S11}$$

$$Q_{cond} = m_{ads}\left(\Delta h_{cond}(T_{evap}) - c_{p,g}\left(\overline{T} - T_{cond}\right)\right)(X_{max} - X_{min}) \qquad \text{S12}$$

Herein $m_{ads}$ refers to the adsorbent mass, $c_{p,ads}$, $c_{p,fl}$ and $c_{p,g}$ to the isobaric heat capacities of adsorbent, water and water vapor, $\overline{T}$ to the arithmetic mean temperature during desorption.

$$\overline{T} = 0.5\left(T_{des,max} + T_{des,min}\right) \qquad \text{S13}$$

Using these set of equations, the COP for a heat pump cycle was calculated for a heating temperature of 40 °C, a cold temperature of 10 °C and a driving temperature of 90 °C. The capacity of the adsorbent $c_{p,ads}$ was assumed to 1 J/(g·K).

## References


1 F. Jeremias, A. Khutia, S. K. Henninger and C. Janiak, *J. Mater. Chem.,* 2012, **22**, 10148-10151.

2 Yu. I. Aristov, An optimal sorbent for adsorption heat pumps: thermodynamic requirements and molecular design in *Proc. VI Minsk International Seminar 'Heat Pipes, Heat Pumps, Refrigerators',* Minsk, 12–15 September, 2005, 342-353.

3 G. C. Shearer, S. Chavan, S. Bordiga, S. Svelle, U. Olsbye and K. P. Lillerud, *Chem. Mater.*, 2016, **28**, 3749-3761.

4 L. X. Gong, R. Z. Wang, Z. Z. Xia and C. J. Chen, *J. Chem. Eng. Data*, 2010, **55**, 2920-2923.

X. Zheng, T. S. Ge, R. Z. Wang and L. M. Hu, *Chem. Eng. Sci.*, 2014, **120**, 1-9

5 S.-J. Ernst, F. Jeremias, H.-J. Bart and S. K. Henninger, *Ind. Eng. Chem. Res.*, 2016, **55**, 13094-13101.

## 3.2 Cucurbit[6]uril@MIL-101-Cl: loading polar porous cages in mesoporous stable host for enhanced $SO_2$ adsorption at low pressures†

Yangyang Sun, Jun Liang, Philipp Brandt, Alex Spieß, Secil Öztürk and Christoph Janiak

Nanoscale. DOI: 10.1039/D1NR04432J

Impact factor 2020: 7.790

**Graphical abstract**

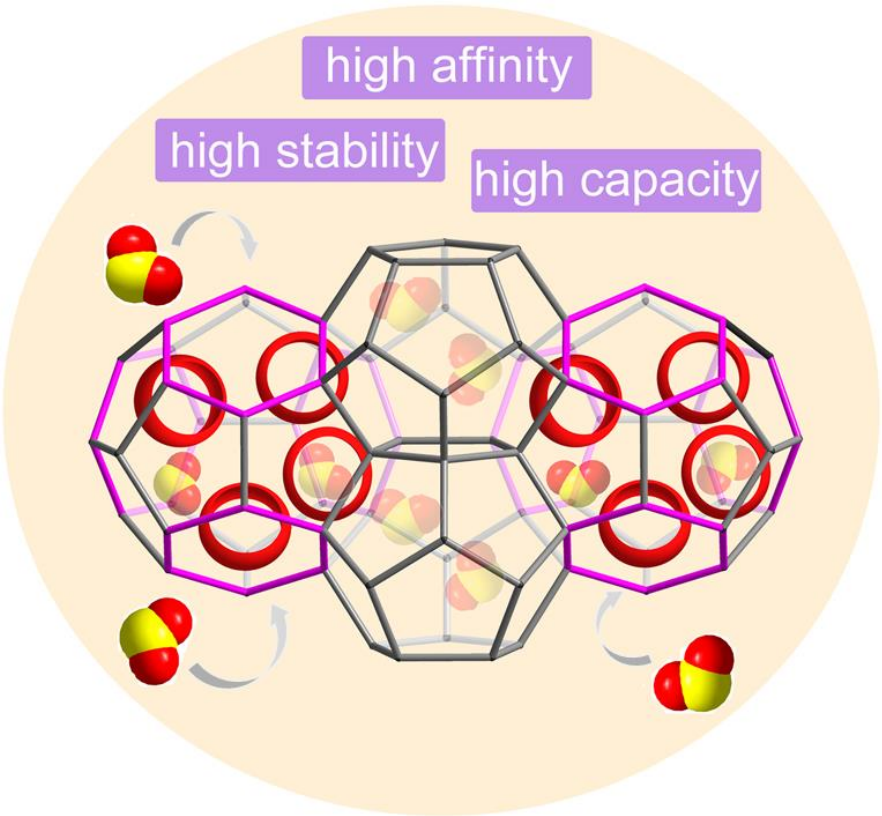


Keywords: Metal-organic frameworks (MOFs); cucurbituril; composite; sulfur dioxide; trace adsorption

## Highlights:

Here we report a CB6-cage@MIL-101 composite with

- improved stability via an unexpected in-situ hydroxide-to-chlorido exchange at the {Cr($\mu_3$-O)($H_2O$)X} SBU;
- higher affinity for $SO_2$ compared to the parent MIL-101 at a low pressure due to the incorporated polar molecules of cucurbit[6]uril (CB6);
- three times higher $SO_2$ capacity than parent MIL-101 at 0.01 bar;
- a high uptake at 1 bar and 293K exceeding those of many other MOFs,
- proven 10-cycle stability for dry $SO_2$ sorption;
- good stability after exposure to humid $SO_2$.

Author's contribution to the work:

My contributions:

- Experimental work and analysis
- Writing the manuscript

- the humid $SO_2$ experimental setup and learning was processed with the help from Philipp Brandt
- SEM images were measured by Alex Spieß
- XPS survey spectra and high-resolution spectra were drawn by Secil Öztürk
- pre-viewed and pre-corrected by Jun Liang

Corrections of the manuscript and responses to reviewers during the review process were made by Prof. Christoph Janiak

The work presented in this chapter has been online published:

## Cucurbit[6]uril@MIL-101-Cl: loading polar porous cages in mesoporous stable host for enhanced $SO_2$ adsorption at low pressures†

Yangyang Sun,[a] Jun Liang,[a,b] Philipp Brandt,[a] Alex Spieß,[a] Secil Öztürk[a] and Christoph Janiak*[a,b]

## Abstract

The robust cucurbituril-MOF composite CB6@MIL-101-Cl was synthesized by a wet impregnation method and a concomitant OH-to-Cl ligand exchange {CB6 = cucurbit[6]uril, 31wt% content in the composite, MIL-101-Cl = $[Cr_3(O)Cl(H_2O)_2(BDC)_3]$, BDC = benzene-1,4-dicarboxylate}. MIL-101-Cl was formed postsynthetically from standard fluorine-free MIL-101 where Cr-OH ligands were substituted by Cl during treatment with HCl. CB6@MIL-101-Cl combines the strong $SO_2$ affinity of the rigid CB6 macrocycles and the high $SO_2$ uptake capacity of MIL-101, and shows a high $SO_2$ uptake of 438 $cm^3\ g^{-1}$ (19.5 mmol $g^{-1}$) at 1 bar and 293K (380 $cm^3\ g^{-1}$, 17.0 mmol $g^{-1}$ at 1 bar and 298 K). The captured $SO_2$ amount is 2.1 mmol $g^{-1}$ for CB6@MIL-101-Cl at 0.01 bar and 293 K (2.0 mmol $g^{-1}$ at 298 K), which is three times higher than that of the parent MIL-101 (0.7 mmol $g^{-1}$) under the same conditions. The near zero-coverage $SO_2$ adsorption enthalpies of MIL-101 and CB6@MIL-101-Cl are –35 kJ $mol^{-1}$ and –50 kJ $mol^{-1}$, respectively, reflecting the impact of the incorporated CB6 macrocycles, having higher affinity towards $SO_2$. FT-IR spectroscopy confirms the interactions of the $SO_2$ with the cucurbit[6]uril moieties of the CB6@MIL-101-Cl composite and $SO_2$ retention for a few minutes under ambient air. Comparative experiments demonstrated loss of crystallinity and porosity after dry $SO_2$ adsorption for MIL-101, while CB6@MIL-101-Cl exhibits nearly complete retention of crystallinity and porosity under the exposure to both dry and wet $SO_2$. Thus,

CB6@MIL-101-Cl can be an attractive adsorbent for $SO_2$ capture because of its excellent recycling stability, high capacity and strong affinity toward $SO_2$ at low pressure.

Keywords: Metal-organic frameworks (MOFs); cucurbituril; composite; sulfur dioxide; trace adsorption

## Introduction

The large-scale emissions of flue gases containing toxic $SO_2$ arouses increasing worldwide concerns. As of 2010, global energy sector emissions of $SO_2$ were estimated to be about 40 Tg.[1] The majority of anthropogenic $SO_2$ emissions originated from coal- and oil-burning for electricity generation.[2] $SO_2$ is responsible for human respiratory diseases including bronchitis, asthma as well as to cardiovascular diseases,[3,4] and $SO_2$ along with $NO_X$ emissions lead to the formation of 'acid rains' that poses significant danger to the health of ecosystems, particularly by inhibiting plant growth and poisoning aquatic life.[5] In addition, $SO_2$ can react with other air pollutants to produce sulphate particles, which are a main component of fine particular matter ($PM_{2.5}$).[6,7] Thus, developing new materials and technologies for $SO_2$ removal is imperative.

Limestone scrubbing, ammonia scrubbing and absorptive removal by organic solvents like monoethanol-amine (MEA) represent the majority of conventional technologies of $SO_2$ removal from flue gases. A capture of more than 95 % $SO_2$ from the gas mixtures could be achieved via use of these traditional approaches.[8-10] Improvements in energy efficiency and decrease of wastes suggest physisorption by solid adsorbents as the most promising alternatives, particularly due to the possibility to minimize energy requirements. It is worth noting that because of the corrosive nature of $SO_2$, its complete as possible removal as the first step of flue gas processing allows broader possibilities for subsequent purification/sequestration steps.[11,12] Therefore, the development of chemically resistant porous materials for adsorptive $SO_2$ removal, especially with high

uptake and selectivity at industrially relevant low partial pressures of $SO_2$, is of great interest.

Metal-organic frameworks (MOFs) have drawn intensive attention in the context of gas storage and separation.[13-15] Due to their high surface area, high pore volume and tunable surface functionality, MOFs can be designed for sorption of toxic chemicals including $SO_2$,[16-19] and the capture of $CO_2$.[20] The stability of MOFs against water vapors should not be overlooked during evaluation of potential MOF adsorbents for $SO_2$ capture.[21] Although some MOFs have been reported to be promising for $SO_2$ adsorption and $SO_2/CO_2$ separation,[22-30] the efficient MOF-based adsorbents with both high stability and high-capacity are still very limited.

MIL-101(Cr), which possesses excellent water stability, high surface area and micro/mesoporosity (29 and 34 Å inner diameter), is a particularly interesting adsorbent for practical applications (the guest-free form corresponds to $[Cr_3(\mu_3\text{-}O)(X)(H_2O)_2(BDC)_3]$, X = F, OH, BDC = benzene-1,4-dicarboxylate). In 2020, Ibarra et al. reported that MIL-101(Cr)-4F(1%) (-4F = fully fluorinated BDC) shows a high $SO_2$ uptake capacity of 18.4 mmol $g^{-1}$ at 1 bar and 298 K and is chemically stable towards dry and humid $SO_2$.[31] The large pore volume, beneficial at higher pressures, is the primary reason for the superior performance of MIL-101(Cr) at 1 bar compared to other microporous MOFs. However, MIL-101(Cr) shows mediocre uptake at low pressure due to the lower density of strongly adsorbing sites, such as open-metal sites,[31] and polar $OH^-$ and $H_2O$ ligands. MIL-101(Cr) has also no polar ligand substituents, such as $-NH_2$ or -OH groups and lacks small micropores in the 4-8 Å region, both of which are advantageous for a low-pressure uptake of $SO_2$.[25,33-35] Importantly, it was also shown that the MIL-101(Cr) (formed by standard fluorine-free conditions), would gradually lose its crystallinity and, therefore the accessible surface area after $SO_2$ sorption at 298 K even under nearly anhydrous conditions.[31]

One effective method to modulate the pore size of a host framework is to introduce functional molecules to obtain composite materials, which may exhibit synergetic performances towards certain adsorbates.[36-40] However, MOF-based composites are not yet reported for $SO_2$ sorption and separation until now to the best of our knowledge. Recently, our group studied the outstanding $SO_2$ sorption and separation performance of a cucurbit[6]uril microporous hydrogen-bonded organic framework (HOF),[41] nanoCB6-H (H stands for the solid-state honeycomb-like structure).[42,43] It was found that the CB6 cages ("barrels") have strong interactions with dry $SO_2$ molecules by forming interactions both on the outer surfaces and in its intrinsic pores at a low pressure.[41] However, the exposure of this CB6 HOF material to humid $SO_2$ conditions led to a phase change and major loss of porosity (particularly its extrinsic pores) due to its weak hydrogen bonds. We propose that the shortcomings of CB6 HOF frameworks can be circumvented by dispersing CB6 molecules in a MOF matrix such as MIL-101 to obtain CB6@MIL-101 (**Scheme 1**).[44] Herein, we report the preparation and characterizations of the targeted CB6@MIL-101-Cl material, which show enhanced $SO_2$ sorption behavior due to the combined merits of high host surface area, optimized pore sizes, CB6 molecules with high $SO_2$ affinity and increased stability toward $SO_2$ molecules. Since CB6 molecules are confined in the pores of MIL-101 frameworks, the performance is less affected by moisture or humid $SO_2$. Further, we discovered that hydrochloride could modify the MIL-101 framework and enhance the stability of the resultant CB6@MIL-101-Cl material toward corrosive $SO_2$ molecules. This work demonstrates for the first time the potential of cage@MOF composite materials for enhanced $SO_2$ removal and storage at low pressures.

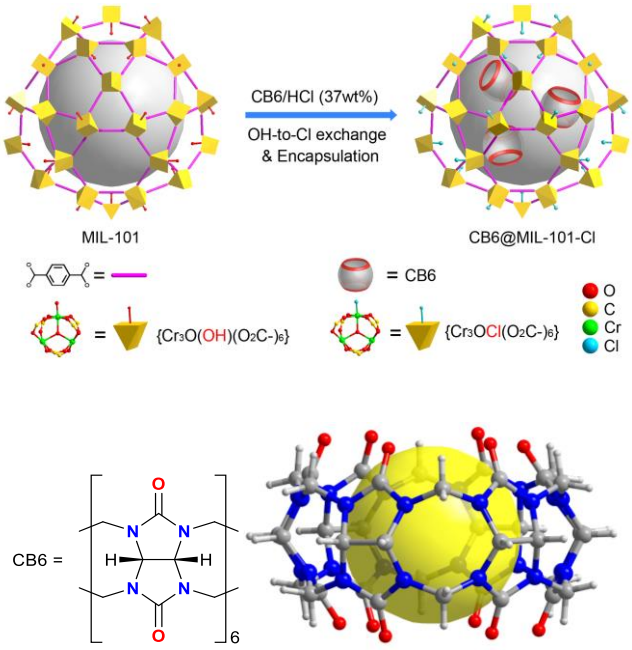


**Scheme 1** Top: Schematic representation of the encapsulation of CB6 molecules in MIL-101 with the formation of the CB6@MIL-101-Cl composite. The two coordinated aqua ligands on the trinuclear chromium SBU are not indicated for clarity. Bottom: Formula and structure of CB6 = cucurbit[6]uril. The yellow sphere represents the intrinsic pore.

## Experimental

### Materials

All starting materials and solvents were obtained from commercial sources and used as delivered (Table S1). CB6 was synthesized according to the literature.[44]

### Characterization methods

Powder X–ray diffraction (PXRD) data were collected at room temperature on *Rigaku Miniflex 600* powder diffractometer using a low background silicon sample holder and Cu-Kα radiation (λ = 1.5418 Å). The measurements were performed over a 2θ=2-50° range with a scan speed of 1.5 deg·min$^{-1}$ (600 W, 40 kV, 15 mA). The diffractograms were analysed using the software Match!.[45]

Elemental analysis (CHNS) was carried out using an *Elementar Analysensysteme vario MICRO cube* instrument. The samples were dried at 150 °C under a vacuum for at least 20 h prior to the measurement.

Fourier transform infrared (FT-IR) spectra were measured on a *Bruker FT-IR Tensor 37* spectrometer at room temperature in the range of 550–4000 $cm^{-1}$ using an attenuated total reflection (ATR) technique (Platinum ATR-QL, diamond). The activated samples were exposed to dry $SO_2$ for 15-30 minutes at room temperature (samples were activated prior to the procedure at 150 °C for 20 h). Then the sealed sample tubes with the MOF in $SO_2$ atmosphere were stored at 77 K for the transfer to the FT-IR instrument room. The tube was allowed to heat up to ~ 273 K and a sample was quickly transferred onto the crystal of the ATR unit, and the stamp of the ATR-unit was immediately closed afterwards. The change of the $SO_2$ amount in the sample was monitored during up to 10 minutes (note that the goal of the experiment was to qualitatively monitor the spectral changes). Resolution: 2 $cm^{-1}$; Sampling time: 16 scans; Background measuring time: 16 scans.

Scanning electron microscopy (SEM) was performed using a *Jeol JSM–6510LV QSEM Advanced* electron microscope with a $LaB_6$ cathode operating at 20 keV. The microscope was equipped with a *Bruker Xflash 410* silicon drift detector for energy-dispersive X-ray (EDX) spectroscopy.

The nitrogen adsorption isotherms were collected at 77 K on a *Quantachrome Autosorb-6* automatic adsorption analyzer and evaluated with the AsiQwin V3 software. The samples were degassed in $10^{-2}$ mbar vacuum at 150 °C prior to the measurement. The Brunauer–Emmett–Teller (BET) surface areas were calculated using the data in the $p/p_0$ range of 0.05–0.2. The total pore volumes were calculated from the adsorbed volume corresponding to $p/p_0 = 0.90$. All gas uptake volume for $N_2$ and $SO_2$ is given at standard temperature and pressure, STP, *i.e.* the equivalent volume at 273.15 K and 1.013 bar.

The $SO_2$ sorption isotherms were collected at 273 K and 293 K on a *Quantachrome Autosorb iQ MP* instrument in $1\times10^{-3}$ – 1 bar pressure range. All samples were activated for at least 12 hours at 150 °C and <0.01 mbar vacuum prior to each experiment.

The cyclic $SO_2$ sorption experiments were carried out on a *Quantachrome Autosorb iQ MP* at 293 K. For the three-cycle ad/desorption measurements, full isotherms (with 17 points for ads. and 12 points for des.) were collected for MIL-101, MIL-101-Cl and CB6@MIL-101-Cl. Between each individual isotherm sorption experiment the samples were activated at 150 °C under vacuum ($1\times10^{-3}$ mbar) for 12 hours. For the 10-cycle adsorption measurements for CB6@MIL-101-Cl, three points (at 0.01, 0.5 and 0.96 bar) were set for quick analysis of adsorption and desorption and also with activation at 150 °C under vacuum ($1\times10^{-3}$ mbar) for 30 minutes before the next cycle was started.

X-ray photoelectron spectroscopy (XPS) was conducted on a ULVAC-PHI VersaProbe II microfocus X-ray photoelectron spectrometer. The spectra were recorded using a polychromatic aluminum Kα X-ray source (1486.8 eV) and referenced to the carbon 1s orbital with a binding energy of 284.8 eV. Experimental XP spectra were fitted by the *CasaXPS* Software (version 2.3.19PR1.0).

**Syntheses**

**MIL-101.** The synthesis was carried out according to a literature method.[46] Chromium(III) nitrate nonahydrate ($Cr(NO_3)_3\cdot9H_2O$; 1.920 g, 4.8 mmol), benzene-1,4-dicarboxylic acid, ($H_2BDC$; 0.813 g, 4.9 mmol), deionized water (24 mL) and nitric acid ($HNO_3$; 0.475 g, 4.9 mmol) as modulator were added in the given sequence. The mixture was stirred for half an hour, and the formed slurry was accurately transferred to a PTFE insert of a hydrothermal autoclave. The sealed autoclave was heated at 200 ℃ for 15 h. After cooling, the obtained solid was separated and washed by dimethylformamide (DMF; 2×50 mL) and ethanol (EtOH; 3×50 mL) *via* centrifugation.

The product was dried at 65 °C overnight. The activation of MIL-101 was performed by degassing at 150 ℃ and ≤ 0.01 mbar vacuum for 20 hours.

**CB6@MIL-101-Cl.** The loading of CB6 to MIL-101 was performed *via* impregnation, according to a literature method.[44] 100 mg of MIL-101 was pre-activated and then added to a solution of 50 mg cucurbit[6]uril (CB6) in 2 mL of concentrated HCl (37 wt%), prepared using sonication. The slurry of MIL-101 was stirred for 4 hours using a magnetic stirrer (strong stirring was avoided in order to preserve the morphology of the material). The resultant solid was washed first by 2×6 mL of HCl (37wt%), followed by 2×20 mL of deionized water and finally 2×20 mL of 96% ethanol (all separations were performed *via* centrifugation). The obtained green solid was dried at 65 ℃ in an oven. The composition of the composite was assessed on its elemental analysis data and in line with previous work[44] as $[Cr_3(O)Cl(H_2O)_2(C_8H_4O_4)_3][C_{36}H_{36}N_{24}O_{12}]_{0.33}$ of 31 wt% of CB6 in CB6@MIL-101-Cl (see ESI† for details).

**MIL-101-Cl**. The activated MIL-101 (100 mg) was treated by HCl (37 wt%, 2 mL) exactly like described in the synthesis of CB6@MIL-101-Cl but without the addition of CB6.

**NanoCB6-H**. For comparison in $SO_2$ sorption, the preparation of nanoCB6-H was carried out according to the literature.[41] 250 mg of CB6 was dissolved in diluted HCl (5 mL, 6 mol/L) under sonication (~2 min). The solution was filtered using a syringe filter (0.2 μm) and poured into 25 mL of methanol under stirring. The formed milky solution was centrifuged for 5 minutes, and the precipitate was washed twice with methanol (25 mL each). Finally, the obtained solid was dried at 65 °C in oven and ground slightly for further use. For activation, nanoCB6-H was degassed at 150 °C for 48 hours.

Humid $SO_2$ stability test (performed on MIL-101, nanoCB6-H, and CB6@MIL-101-Cl).

The method closely follows the description in the literature (Scheme S1, ESI†).[25] A pre-dried air stream (2 L $min^{-1}$) was bubbled through an aqueous sodium metabisulfite solution (0.4 g $Na_2S_2O_5$ in 80 mL water) within a Schlenk flask (250 mL). The setup was equipped with a 3-way valve to regulate the outlet of the gas flow. The outlet of the flask was either connected to a desiccator, playing the role of a humidity chamber, or to the exhaust air when the concentration of $SO_2$ in the chamber reached the target value. The diluted $SO_2$ stream flowed through the desiccator and escaped through a vent. The desiccator contained a crystallizing dish filled with saturated sodium chloride solution (80 mL) ensuring a relative humidity (RH) near 75%. The RH value was monitored with a VWR TH300 hygrometer and the $SO_2$ content with Dräger Pac 6000 electrochemical sensor.

50 mg of each MIL-101, nanoCB6-H and CB6@MIL-101-Cl were pre-activated (≤0.01 mbar, 150 °C overnight) and exposed to humid $SO_2$ (35 ± 5 ppm content in the gas stream) by placing them in the desiccator at 75% relative humidity in open broad-necked glass vials for 6 hours at room temperature. Afterwards, the samples were dried at 65 °C in the oven and activated (≤0.01 mbar, 150 °C overnight) for further measurements.

## Results and discussion

MIL-101, chromium(III) terephthalate, is built of trinuclear $\{Cr_3(\mu_3\text{-}O)X(H_2O)_2(O_2C\text{-})_6\}$, X = F, OH secondary building units (SBUs), which are bridged by the terephthalate linkers ($BDC^{2-}$), forming a porous zeotypic framework with two types of mesocages with diameters of 29 and 34 Å.[47,48] The small cages have pentagonal windows with a diameter of 12 Å, and the large cages have hexagonal windows with diameters of 15 Å in addition to the pentagonal windows (Scheme S2, ESI†). The molecular size of CB6 is 14.4 Å with a height of 9.1 Å.[44] Depending on the synthetic conditions the trinuclear unit has either a charge-compensating fluorido or a hydroxido ligand coordinated by one of the chromium atoms of the SBU.

MIL-101, $[Cr_3(\mu_3\text{-}O)(OH)(H_2O)_2(BDC)_3]$ was prepared according to the literature,[43] and was used as a host to load CB6, which was performed *via* stirring of the MIL-101 in a CB6 solution in conc. HCl (37 wt%) (Scheme 1). We refer to this process as "wet impregnation". It should be noted that cucurbit[6]uril was dissolved in conc. HCl (37 wt%) before being treated with MIL-101. A composite material designated as CB6@MIL-101-Cl was the result of the loading of CB6 into MIL-101. The treatment of the MIL-101 host with the HCl solution caused the simultaneous exchange of the charge-balancing hydroxido ligand by chlorido ligand, transforming the host framework to MIL-101-Cl, $[Cr_3(\mu_3\text{-}O)Cl(H_2O)_2(BDC)_3]$ during the loading (Scheme 1). Thus, the formation of CB6@MIL-101-Cl, containing 31 wt% of CB6 according to the elemental analysis, and the conversion of the framework by exchange of the terminal anionic ligand, were performed as a concomitant "one-pot" process.

Powder X-ray diffraction (PXRD) confirmed the phase purity of MIL-101 and the retention of the MIL-101 framework structure in CB6@MIL-101-Cl (Fig. S1, ESI†). The nearly identical PXRD patterns confirmed that neither the hydroxido-to-chlorido exchange nor the encapsulation of CB6 into the pores influences the structure of the framework significantly. Compared with the Fourier transform infrared (FT-IR) spectroscopy of MIL-101, CB6@MIL-101-Cl shows additional peaks at 1740 $cm^{-1}$ and at 1465 $cm^{-1}$ due to the carbonyl and methylene groups of CB6 (Fig. S2, ESI†).[44]

The extent of the hydroxido-to-chlorido ligand exchange was quantified by energy dispersive X-Ray analysis (EDX) and X-ray photoelectron spectroscopy (XPS) measurements. For MIL-101 a negligible Cl content was confirmed by both EDX and XPS. EDX data (Fig. S3, Table S3, ESI†) suggests a $[Cr_3(\mu_3\text{-}O)Cl_x(OH)_{1-x}(H_2O)_2(BDC)_3]$ framework formula with $x = 0.78$ in the CB6@MIL-101-Cl composite. The $Cl/Cr_3$ ratio was checked also after one-cycle of $SO_2$ adsorption-desorption. As a result, the value $x = 0.69$ was found for CB6@MIL-101-Cl (Fig. S3, Table S3, ESI†),

which are slightly lower compared to the initial materials, *i.e.,* prior to the $SO_2$ adsorption-desorption cycle, but still within experimental error.

XPS measurements were carried out after one-cycle of $SO_2$ adsorption-desorption (Fig. S4 – S5, ESI†). The $Cl/Cr_3$ ratio or x in $[Cr_3(\mu_3\text{-}O)Cl_x(OH)_{1-x}(H_2O)_2(BDC)_3]$ was 1.08 in CB6@MIL-101-Cl (Table S4, ESI†). The XPS survey spectra show Cr and S for MIL-101, and Cr and Cl but no S for CB6@MIL-101-Cl (Fig. S4, ESI†). The S content in CB6@MIL-101-Cl was not detectable. The high-resolution Cl 2p spectrum for CB6@MIL-101-Cl features the Cl $2p_{1/2}$ and Cl $2p_{3/2}$ pair of peaks at 199.2 eV and 197.5 eV binding energies (Fig. S5, ESI†), which corresponds to a chloride ion,[49-51] in line with the spin-orbit splitting value of 1.6 eV. The high-resolution Cr 2p XPS spectrum exhibits peaks at 587.3 eV and 577.8 eV for MIL-101, and 586.7 eV and 577.3 eV for CB6@MIL-101-Cl (Fig. S5, ESI†). These values correspond well to typical 587.4 eV and 577.8 eV binding energies for $Cr^{III}$ 2p (two Cr 2p peaks are observed due to spin-orbit splitting, which matches the expected value of 9.3 eV).[52-54] The 0.5 – 0.6 eV shift to lower binding energy of Cr 2p for CB6@MIL-101-Cl compared with MIL-101 derives from the slight change of the average Cr environment due to the hydroxido-to-chlorido exchange.

The high-resolution S 2p spectrum for MIL-101 (Fig. S5, ESI†) exhibits the S $2p_{1/2}$ and S $2p_{3/2}$ pair of peaks at 170 eV and 168.8 eV binding energies with a peak separation of 1.2 eV, which verified the chemical oxidation state of S(IV).[55] The $S/Cr_3$ ratio is 4.23 in MIL-101 after one-cycle of $SO_2$ adsorption-desorption (Table S4, ESI†). In contrast, sulfur could not be detected in CB6@MIL-101-Cl after $SO_2$ sorption. Since XPS operates under high vacuum we suggest putatively an initial reaction of Cr-OH in MIL-101 with $SO_2$ under formation of Cr-hydrogensulfite, $Cr\text{-}OSO_2H$ or -disulfite, $Cr\text{-}OS_2O_4H$ leading to an opening up of Cr coordination sites for further $SO_2$ chemisorption. The S 2p XPS spectrum of MIL-101 matches with metal(Ce, Ti)-sulfite/hydrogensulfite.[21,56,57]

Scanning electron microscopy (SEM) images further confirmed the retention of the morphology, thereby supporting the expected stability of the material also on the macroscopic level under mild adsorptive loading conditions. The synthesized MIL-101 and CB6@MIL-101-Cl phases have similar particle sizes (0.5–2.0 μm) and feature octahedral crystals typical for MIL-101[58,59] (Fig. S6, ESI†). The absence of other significant crystal forms or coverage of the octahedral surfaces indicates that CB6 is not crystallizing separately on the outer surface of the MIL-101 crystallites.

The porosity of the samples was assessed by analysis of the $N_2$ adsorption-desorption isotherms measured at 77 K. The isotherm types of both MIL-101 and CB6@MIL-101-Cl are similar and retain the characteristic two-step shape (corresponds to IUPAC type Ib isotherms)[60] (Fig. 1). As expected, the uptake decreases after the encapsulation of CB6 in MIL-101. The Brunauer–Emmett–Teller (BET) surface areas for MIL-101 and CB6@MIL-101-Cl were found to be 3217 $m^2\ g^{-1}$and 2077 $m^2\ g^{-1}$, respectively, their pore volumes 1.54 $cm^3\ g^{-1}$ and 1.00 $cm^3\ g^{-1}$ (assessed at $p/p_0 = 0.9$; Table S2, ESI†). The BET surface area for nanoCB6-H was 435 $m^2\ g^{-1}$.

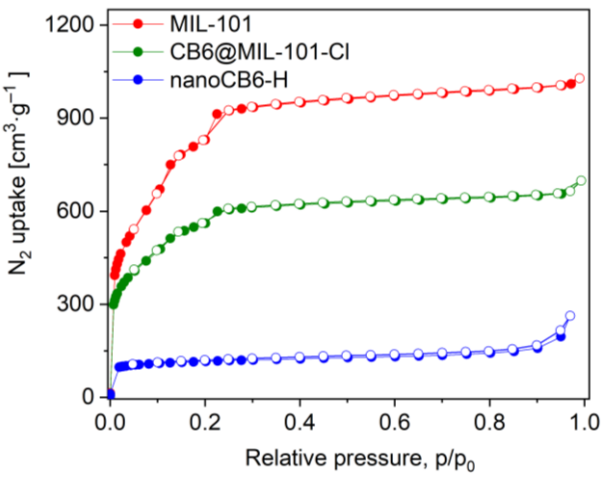


**Fig. 1** Nitrogen adsorption-desorption isotherms at 77 K of MIL-101, CB6@MIL-101-Cl and nanoCB6-H. Filled symbols, adsorption; empty symbols, desorption.

The $SO_2$ adsorption-desorption isotherms were measured for MIL-101, CB6@MIL-101-Cl, and nanoCB6-H at 293 K (Fig. 2a). All three materials feature a relatively narrow hysteresis for the whole measured range. MIL-101 has an almost linear $SO_2$ uptake reaching 620 $cm^3\ g^{-1}$ and 584 $cm^3\ g^{-1}$ (27.7 mmol $g^{-1}$ and 24.4 mmol $g^{-1}$) at 293 K and 298 K, respectively, and 1 bar. Expectedly, as the temperature increases, the amount of gas adsorbed decreases. On the other hand, the uptake for the nanoCB6-H is 6.5 mmol $g^{-1}$ (145 $cm^3\ g^{-1}$) at 1 bar and 293 K, in line with its comparatively low total pore volume (Table S2, ESI†). However, about 43% of the total uptake of nanoCB6-H occurs in the low-pressure range of 0–0.01 bar, which reflects the strong affinity of CB6 toward $SO_2$ (Fig. 2b, Fig. S7, Table S5, ESI†). "Nano" in nanoB6-H refers to a particle size of 100–500 nm. NanoCB6-H shows a higher $SO_2$ uptake (63 $cm^3\ g^{-1}$, 145 $cm^3\ g^{-1}$) than micro-size crystallites of CB6 (43 $cm^3\ g^{-1}$, 98 $cm^3\ g^{-1}$) at both 0.01 bar and 0.97 bar and 293K, due to the faster diffusion of $SO_2$ molecules in nanoCB6-H with smaller CB6 particle size.[41]

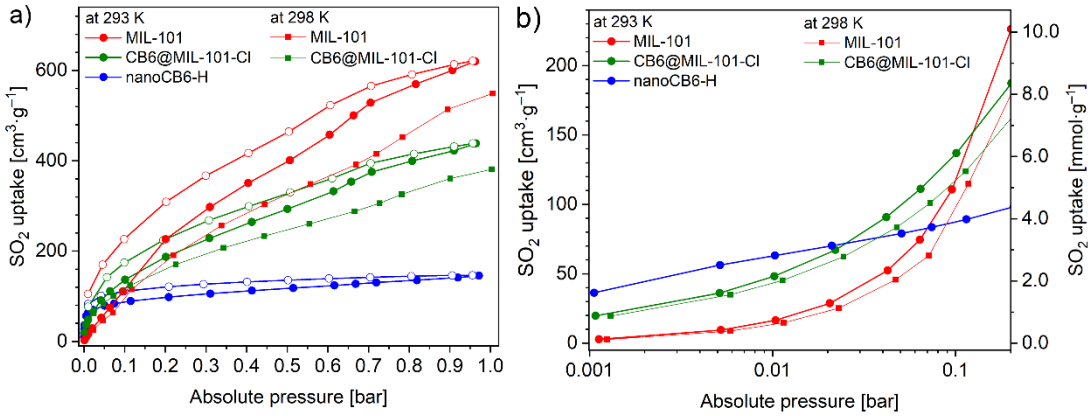


**Fig. 2** $SO_2$ sorption isotherms for MIL-101 and CB6@MIL-101-Cl at 293 K (normal lines) and 298 K (thin lines, adsorption branch only), and for nanoCB6-H at 293 K: a) 0-1 bar range. b) 0.001-0.2 range, logarithmic scale (In b the desorption isotherms are omitted for clarity).

The CB6@MIL-101-Cl composite combined the merits of the two materials for $SO_2$ adsorption. It merges the strong affinity of the CB6 cages at low pressure and the high capacity of MIL-101. At 1 bar, a high $SO_2$ uptake of 438 $cm^3\ g^{-1}$ or 380 $cm^3\ g^{-1}$ (19.5

mmol $g^{-1}$, 17.0 mmol $g^{-1}$) at 293 K or 298 K, respectively, is reached, which is better than for most other $SO_2$-stable MOF materials (Table S6, ESI†), except of MIL-101 (27.7 mmol $g^{-1}$ at 293 K) and MOF-177 (25.7 mmol $g^{-1}$ at 293 K).[29] However, MOF-177 and MIL-101are unstable after $SO_2$ exposure, while the composite CB6@MIL-101-Cl is stable after $SO_2$ exposure. Understandably, the maximum uptake decreases somewhat in the CB6@MIL-101-Cl composite compared to the MIL-101 host, due to a lower total pore volume (Table S2, ESI†). The $SO_2$ adsorption isotherms of MIL-101 and CB6@MIL-101-Cl at 1 bar did not reach saturation as they still have a high positive slope and are far from levelling off. Saturation will require a pressure above 1 bar.

At 0.01 bar and 293 K the captured $SO_2$ amount was 2.2 mmol $g^{-1}$ (2.0 mmol $g^{-1}$ at 298 K) for CB6@MIL-101-Cl compared to 0.7 mmol $g^{-1}$ (0.6 mmol $g^{-1}$ at 298 K) for MIL-101, *i.e.,* a remarkable improvement by a factor of three (Fig. 2b). For comparison, the $SO_2$ uptake of nanoCB6-H was found to be 2.8 mmol $g^{-1}$ at 0.01 bar. The important steep increase in the uptake of $SO_2$ by CB6@MIL-101-Cl in the low-pressure zone demonstrates the desirable efficiency for $SO_2$ removal at low partial pressure. The calculated mass-weighted $SO_2$ uptake for a physical mixture of CB6 and MIL-101 would be only 1.3 mmol $g^{-1}$ at 0.01 bar, indicating a synergistic effect in the composite CB6@MIL-101-Cl. At 293 K and 0.01 bar, the $SO_2$ uptake of CB6@MIL-101-Cl (2.2 mmol $g^{-1}$ at 293 K and (2.0 mmol $g^{-1}$ at 298 K) is significantly higher than that of most MOF sorbents in the literature (Fig. S8, Table S6, ESI†), and only lower than that of SIFSIX-2-Cu-i and MIL-160 (4.2 mmol $g^{-1}$),[28,29] SIFSIX-1-Cu (3.4 mmol $g^{-1}$),[28] DMOF-TM (3.8 mmol $g^{-1}$),[35] MFM-305 (3.3 mmol $g^{-1}$),[27] MFM-305-$CH_3$, $NH_2$-MIL-125(Ti) and mmen-MIL-101(Cr) (3.0 mmol $g^{-1}$),[27,29,61] as well as SIFSIX-3-Ni (2.4 mmol $g^{-1}$).[28] However, those materials show a lower uptake at 1 bar compared to CB6@MIL-101-Cl (Table S6, ESI†).

The isosteric enthalpy of adsorption ($\Delta H_{ads}$) for $SO_2$ adsorption on CB6@MIL-101-Cl and MIL-101 was calculated from the adsorption isotherms measured at 273 K and 293

K using the virial method (Fig. 3, Fig. S9 – S10, ESI†).[61] The near zero-coverage adsorption enthalpy of $SO_2$ ($\Delta H_{ads}^0$) for CB6@MIL-101-Cl is ~–50 kJ·mol$^{-1}$, while for MIL-101 it is ~–35 kJ·mol$^{-1}$. The higher negative $\Delta H_{ads}^0$ of $SO_2$ for CB6@MIL-101-Cl proves that the incorporation of CB6 cages can indeed increase the affinity of materials towards $SO_2$, probably by narrowing the pores towards multiple optimal gas-adsorbent interactions[25,33,35,63] and providing intra/outer surfaces of the relatively polar CB6 for $SO_2$ adsorption, even if the loading may block some of the external sites.

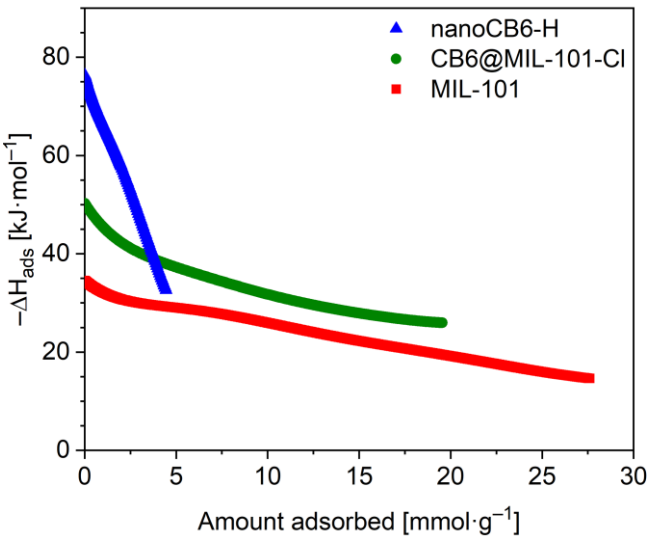


**Fig. 3** Isosteric enthalpy of adsorption dependence on the amount of $SO_2$ adsorbed for MIL-101, CB6@MIL-101-Cl and nanoCB6-H.

It should be noted that the $\Delta H_{ads}^0$ value of $SO_2$ for nanoCB6-H was ~–76 kJ mol$^{-1}$ when the material was activated at 150 °C, at the same temperature as CB6@MIL-101-Cl and MIL-101 (in previous work,[41] where nanoCB6-H was only activated at 100 °C, $\Delta H_{ads}^0$ = –65 kJ mol$^{-1}$ was given). From DFT-D3 (dispersion-corrected DFT) calculations on the possible binding sites for $SO_2$ at CB6 macrocycles the cavity of the CB6 cage was the highest-energy binding site with a calculated binding energy of –82 kJ·mol$^{-1}$. There, $SO_2$ molecules are primarily adsorbed through two electrostatic $O_2S^{\delta+}\cdots\ ^{\delta-}O{=}C(CB6)$ interactions at an S···O distance of 3.04 Å. The intrinsic pore of CB6 is large enough (5.8 Å center diameter, 3.9 Å window diameters, 9.1 Å height) to encapsulate two $SO_2$ molecules, which can enter in these $O_2S^{\delta+}\cdots\ ^{\delta-}O{=}C(CB6)$ interactions in the confined

space. The second highest-energy binding site with calculated –50 kJ·mol$^{-1}$ has $SO_2$ located around the outer surface and involves electrostatic $O_2S^{\delta+}\cdots{}^{\delta-}O{=}C$(CB6), $O_2S^{\delta+}\cdots{}^{\delta-}N$(CB6) and $OSO^{\delta-}\cdots{}^{\delta+}H$-C(CB6) interactions.[41]

With regard to $\Delta H^0_{ads}$, the composite is closer to MIL-101 than to nanoCB6-H, while in the case of a non-interacting, physical mixture, $\Delta H^0_{ads}$ should be equal to the latter. The decrease could be interpreted as a blockage of active sites, *e.g. via* MIL-host···CB6-guest interactions. Also, the state of the CB6 guests in the MIL pores will be rather amorphous; thereby, the high values for the CB6-H crystalline state, could barely be expected. With increased loading of $SO_2$, the isosteric enthalpy of adsorption ($-\Delta H_{ads}$) of all three materials is decreased (Fig. 3), according to the occupation of binding sites in the order of decreasing binding energies, also indicating adsorbents with different sites.

Comparative FT-IR spectroscopy was employed to assess the possible $SO_2$ adsorption sites in CB6@MIL-101-Cl and MIL-101. A series of spectra of the $SO_2$ loaded compounds with gradually decreasing $SO_2$ content, as a result of contact with ambient atmosphere (0 to 10 min), were collected as described in the experimental section, and compared with the spectrum of the activated compound (Fig. 4). The new bands, appearing as a result of adsorption, at 1328 and 1144 cm$^{-1}$ in CB6@MIL-101-Cl and at 1332 and 1146 cm$^{-1}$ in MIL-101 are assigned to the asymmetric and symmetric stretching vibrations of the physisorbed $SO_2$ molecules.[64,65] The new bands are slightly shifted compared to the bands at 1330 and 1149 cm$^{-1}$ for free $SO_2$ molecules, thereby indicating the interaction with the surface of the materials. The intensity of the bands assigned to the adsorbed $SO_2$ gradually decreases with time. The bands are traceable for around 2 minutes for MIL-101 and around 5 minutes for CB6@MIL-101-Cl under the same experimental conditions (Fig. 4, Fig. S11, ESI†). This can be seen in line with the difference in isosteric adsorption enthalpy since the adsorption kinetics are judged

as similar from the similar hysteresis widths of the desorption isotherms for MIL-101 and CB6@MIL-101-Cl.

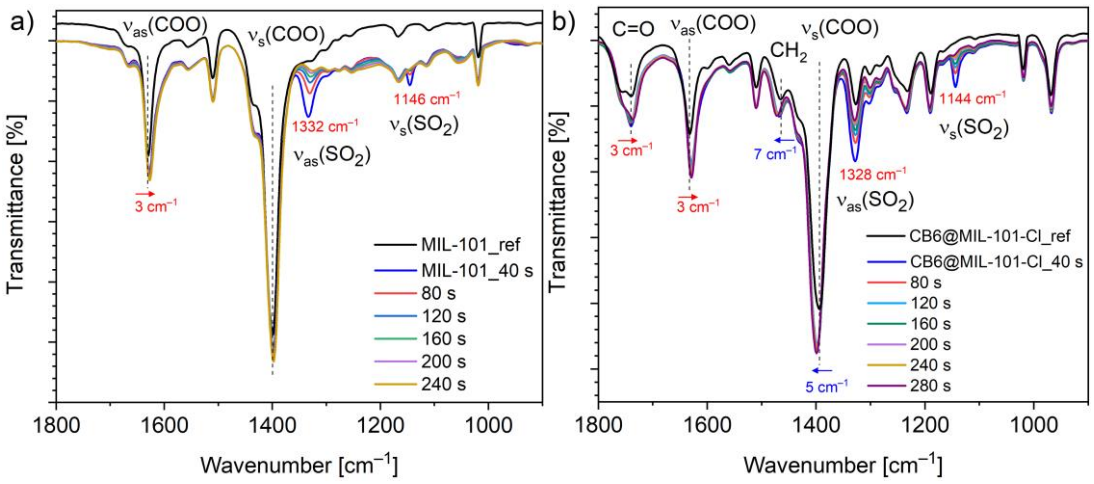


**Fig. 4** FT-IR spectra of a) MIL-101 and b) CB6@MIL-101-Cl before and after single exposure and loading with $SO_2$ (see Exp. Section for details).

The comparison of the FT-IR spectra of the activated materials and the materials with variable $SO_2$ contents also show vibrational changes of functional groups of the frameworks. The bands at 1630 cm$^{-1}$ and 1398 cm$^{-1}$ in MIL-101 and at 1632 cm$^{-1}$ and 1394 cm$^{-1}$ in CB6@MIL-101-Cl are attributed to the asymmetric $\nu_{as}$ and symmetric $\nu_s$ carboxylate (COO) stretching vibrations.[61,66] In both materials, after exposed once to $SO_2$, the carboxylate $\nu_{as}$(COO) band is red-shifted ($\Delta = -3$ cm$^{-1}$), and the $\nu_s$(COO) band is blue-shifted ($\Delta = 5$ cm$^{-1}$ for CB6@MIL-101-Cl and invariant within experimental error of ±2 cm$^{-1}$ for MIL-101).

It is worth nothing that the carboxylate frequency shifts observed for CB6@MIL-101-Cl tend to be more pronounced compared to MIL-101. Additionally, the IR spectral response of CB6 in CB6@MIL-101-Cl upon $SO_2$ exposure is also clearly traceable. Thus, the carbonyl stretching vibration $\nu$(CO) = 1740 cm$^{-1}$ of CB6 demonstrates a red shift ($\Delta = -3$ cm$^{-1}$) upon $SO_2$ adsorption and the methylene bending vibration $\nu(CH_2)$ = 1465 cm$^{-1}$ a blue shift ($\Delta = 7$ cm$^{-1}$) indicating interactions between $SO_2$ and CB6. In comparison, nanoCB6-H under the same conditions on the same instrument features a

slightly stronger red shift of ν(CO) ($\Delta$ = –6 cm$^{-1}$) and a slightly weaker blue shift of ν(CH$_2$) ($\Delta$ = 4 cm$^{-1}$).[41]

The FT-IR spectra (Fig. S12, ESI†) of MIL-101 andCB6@MIL-101-Cl after one full $SO_2$ ad/desorption cycle followed by degassing at 150°C and 1 × 10$^{-3}$ mbar for 12 h were also measured. It was found that the spectrum of CB6@MIL-101-Cl was essentially unchanged within experimental error which supports the stability of CB6@MIL-101-Cl towards dry $SO_2$ sorption. In MIL-101, the broad $\nu_{as}$(COO) band in MIL-101, initially at ~1630 cm$^{-1}$, is remarkably red-shifted ($\Delta$ = –10 cm$^{-1}$). The shift is comparable to the one observed in $SO_2$ loaded MFM-170 carboxylate MOF ($\Delta$ = –10 cm$^{-1}$), suggesting the interaction between $SO_2$ and carboxylate groups in the framework.[23] More importantly, new bands at 1100 cm$^{-1}$ and 1049 cm$^{-1}$ and a broad band at 900 – 1200 cm$^{-1}$ appeared, which were attributed to the presence of sulfite and hygrogensulfite species.[63,66,67] This is in line with the observation from XPS (Fig. S5, Table S4, ESI†). The broadening of the $\nu_{as}$(COO) band indicates the partial collapse and decrease of the local uniformity in the MIL-101 framework.

To further investigate the stability of these materials against dry $SO_2$, we performed cyclic adsorption-desorption at 293 K up to 0.96 bar for three runs for MIL-101, MIL-101-Cl and CB6@MIL-101-Cl and also for 10 runs for CB6@MIL-101-Cl (see the experimental section). The uptake by MIL-101 gradually decreased to 40% from 620 to 245 cm$^3$ g$^{-1}$ (Fig. S13, ESI†), as expected from earlier reports,[61,69] while CB6@MIL-101-Cl maintained 95% of the initial uptake amount also over 10 cycles (Fig. 5). It is worth noting here that statements about the limited stability of MIL-101 against dry $SO_2$ can be found in a few publications.[31,61] Ibarra et al. had noted that not only the chromium-hydroxide-containing MIL-101, i.e. [$Cr_3(O)(OH)(H_2O)_2(BDC)_3$], but also the more crystalline chromium-fluoride-containing MIL-101 compound, i.e. [$Cr_3(O)F(H_2O)_2(BDC)_3$], were unstable (cf. sample MIL-101(Cr)-HF, Fig. S22-S24 in ref. 31). A MIL-101 with stability towards dry and humid $SO_2$ could only be obtained

with partial incorporation of a fully fluorinated BDC ligand, giving the sample MIL-101(Cr)-4F(1%) which then showed a high $SO_2$ uptake capacity of 18.4 mmol $g^{-1}$ at 1 bar and 298 K.[31] There is an ambiguity regarding the scattered literature data on the stability of Cr(III)-MOFs, but the instability against dry $SO_2$ is the more surprising as Cr(III)-MOFs are in general considered to be highly kinetically inert.

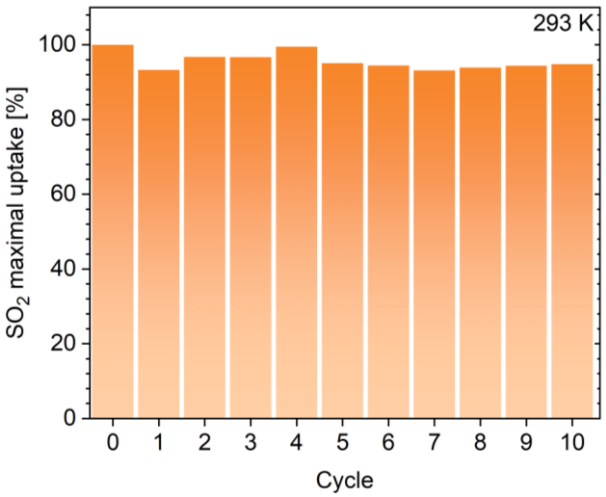


**Fig. 5** $SO_2$ adsorption capacity of CB6@MIL-101-Cl at 293 K and 0.96 bar, measured over 10 repetitive adsorption-desorption cycles.

The enhanced stability of the CB6@MIL-101-Cl composite towards dry $SO_2$ could be explained by the hydroxido-to-chlorido ligand exchange, that is the substitution of the terminal Cr-OH ligand in the $[Cr_3(O)X(H_2O)_2(BDC)_3]$ coordination framework of MIL-101 by Cr-Cl in CB6@MIL-101-Cl. To check the hypothesis a sample of MIL-101-Cl was prepared from MIL-101 in the absence of CB6 but otherwise under the same conditions as CB6@MIL-101-Cl, and submitted to $SO_2$ adsorption-desorption cycling for three runs (Fig. S13, ESI†). The textural properties of MIL-101-Cl are listed in Table S7, ESI†. The BET surface area of MIL-101-Cl is somewhat higher than that of the parent MIL-101, which we reason with the decomposition of pore-filling residual coordination species by HCl and the subsequent removal through the washing processes.[70] MIL-101-Cl have kept 97 % adsorption capacity of the initial uptake after three adsorption-desorption runs at 293 K (Fig. S13, ESI†). The $N_2$ sorption-based

BET-surface area and total pore volume of MIL-101, CB6@MIL-101-Cl and MIL-101-Cl before and after multi-cycle $SO_2$ sorption confirmed the above conclusions from the cyclic $SO_2$ sorption experiments. The BET surface area decreased by 45% (1768 $m^2 g^{-1}$ vs 3217 $m^2 g^{-1}$) for MIL-101, but was retained within experimental error (2036 $m^2 g^{-1}$ vs 2077 $m^2 g^{-1}$) for CB6@MIL-101-Cl and even slightly increased (3541 $m^2 g^{-1}$ vs 3408 $m^2 g^{-1}$) for MIL-101-Cl after SO exposure to $SO_2$ at 293 K (Table S7, ESI†). The comparison of the PXRD patterns before and after cyclic $SO_2$ sorption for MIL-101, CB6@MIL-101-Cl and MIL-101-Cl verified the preservation of the crystallinity in the two later cases compared to the deterioration of the parent material MIL-101 (Fig. S14, ESI†). Thereby, the combined $N_2$ adsorption and PXRD data confirm the enhanced stability of CB6@MIL-101-Cl and MIL-101-Cl against $SO_2$ compared to the instability of the parent MIL-101. Further, the comparative experiments with MIL-101-Cl suggest that its increased stability is due to the facile one-step hydroxido-to-chlorido ligand exchange in the framework.

In this work we are focusing on the enhanced $SO_2$ uptake and stability of CB6@MIL-101-Cl. The interesting and counterintuitive instability of the parent MIL-101 will be thoroughly addressed in a follow-up study.

Considering the inevitable moisture presence for any possible real-world applications, the stability of materials towards humid $SO_2$ was also investigated by PXRD diffraction and $N_2$ sorption analyses. The PXRD patterns of MIL-101 and CB6@MIL-101-Cl after humid $SO_2$ treatment were retained, indicating their intact frameworks. In contrast, nanoCB6-H lost most of its crystallinity under acidic humid $SO_2$ atmosphere condition. (Fig. S15, ESI†). $N_2$ adsorption-desorption isotherms (Fig. 6) showed that MIL-101 and CB6@MIL-101-Cl kept the BET surface areas unchanged after exposure to humid $SO_2$ (35 ppm) for 6 h.

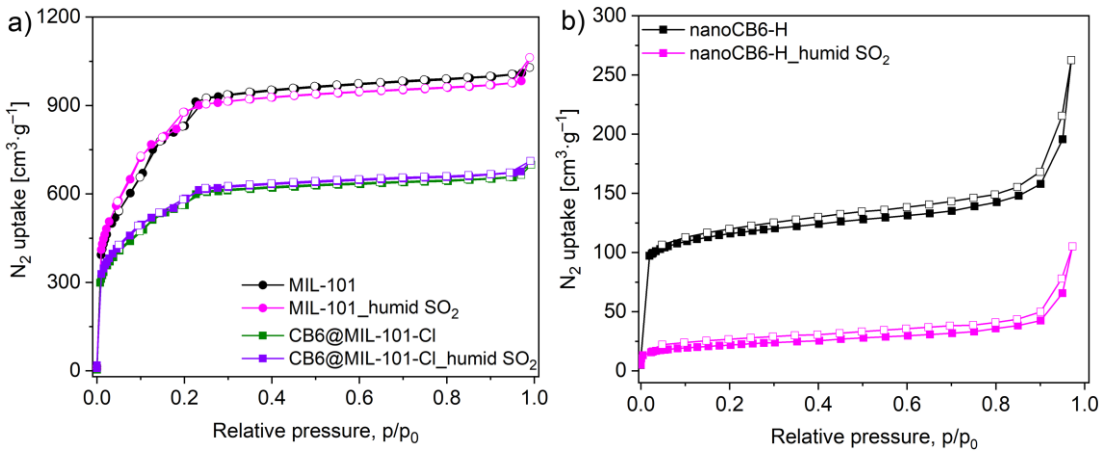


**Fig. 6** $N_2$ adsorption isotherms (77 K) for (a) MIL-101 and CB6@MIL-101-Cl; (b) nanoCB6-H after exposure to humid $SO_2$ for 6 h.

The BET surface area of nanoCB6-H significantly decreased and only 18% of the initial BET surface area was retained (Table S7, ESI†). This result confirmed again that the hydrogen-bonded organic framework nanoCB6-H is unstable in humid conditions, which is in line with our previous study.[41] The fact that MIL-101 was unstable in dry $SO_2$ but stable in humid $SO_2$ conditions could be related to the role of water vapor. We propose that under dry conditions, the Cr-OH site of MIL-101 is well accessible for the reaction with $SO_2$ molecules, while under humid conditions this site (and possibly other reactive sites) is blocked and protected by water clusters. Note that MIL-101 has a medium hydrophilic surface and good stability in acidic solution.[71-73] A similar counterintuitive observation was made in Zeolite Y, which exhibited a better stability performance under humid $SO_2$ exposure conditions than toward dry $SO_2$. Also for Zeolite Y the pre-adsorbed water in this highly hydrophilic framework may block the accessibility of $SO_2$.[25]

In addition, the full $SO_2$ sorption isotherms of these three samples (MIL-101, CB6@MIL-101-Cl and nanoCB6-H) after exposure to humid $SO_2$ (35 ppm) for 6 h were measured (Fig. S16, ESI†). The $SO_2$ uptake capacity of nanoCB6-H after exposure to humid $SO_2$ decreased due to its decreased porosity (Fig. 7). Both MIL-101 and CB6@MIL-101-Cl showed unchanged or even slightly increased $SO_2$ uptakes at 0.01

bar together with around 20% loss of total uptake capacity at 1 bar when compared to dry $SO_2$ sorption (Fig. 7, Table S8, ESI†). Therefore, CB6@MIL-101-Cl exhibits enhanced stability and $SO_2$ removal capability over MIL-101 under lower pressures in both dry $SO_2$ and humid conditions. This stability under humid conditions is a necessity for realistic applications in view of the ubiquitous presence of water.

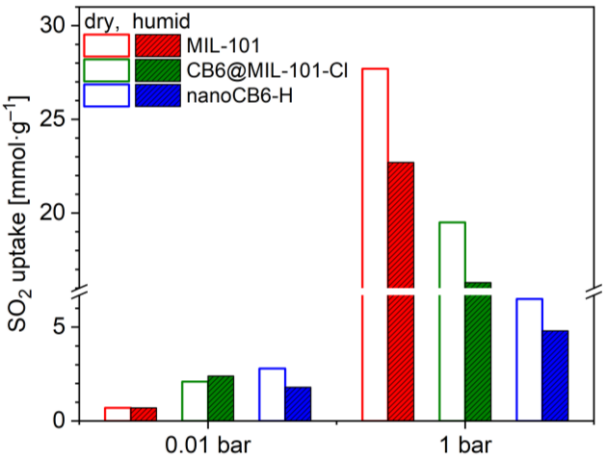


**Fig. 7** $SO_2$ adsorption uptake (293 K) for MIL-101, CB6@MIL-101-Cl and nanoCB6-H after exposure to humid $SO_2$ for 6 h compared to the behavior under dry conditions (Table S8, ESI†).

## Conclusions

We have systematically investigated a cage/MOF composite, named CB6@MIL-101-Cl, obtained by wet impregnation of cucurbituril, CB6 cages into the pores of MIL-101 for potential $SO_2$ gas removal. It is found that CB6@MIL-101-Cl shows enhanced performance in the removal of $SO_2$ gas under low pressure due to the combined merits of CB6 cages with high affinity towards $SO_2$ and MIL-101 with hierarchical pores. The relatively strong interactions between $SO_2$ molecules and CB6@MIL-101-Cl surfaces were supported by time-dependent FT-IR (ATR) spectra. MIL-101 was again confirmed to be unstable towards dry $SO_2$. The stability of CB6@MIL-101-Cl was enhanced when compared with MIL-101 due to the unexpected hydroxido-to-chloride exchange in the $\{Cr_3(O)X(BDC)_3\}$ metal node of MIL-101. This unexpected postsynthetic modification was supported by EDX and XPS analysis of

related materials. The targeted CB6@MIL-101-Cl shows a high $SO_2$ uptake of 19.5 mmol $g^{-1}$ at 293 K and 1 bar and high chemical stability even under humid $SO_2$ conditions. The counterintuitive instability of the parent MIL-101 and the observed enhanced stability of MIL-101-Cl is an unexpected finding, which will be thoroughly addressed in a follow-up study and for which the technological importance might be very high. The investigation of the comparable stabilities of different MIL-101-X materials, where X is a terminal counter-anion, is a task, which we are targeting in the near future.

## Conflicts of interest

There are no conflicts to declare.

## Author Contributions

All the authors have significantly contributed to the paper and have given approval to the final version of the manuscript.

## Acknowledgements

We thank the China Scholarship Council (CSC) for granting a PhD fellowship to Y.Y.S. J.L. acknowledges financial support of NSFC (22001178) and support from the Hoffmann Institute of Advanced Materials (HIAM), Shenzhen Polytechnic. The authors thank Dr. István Boldog, Dr. Shanghua Xing, Mr. Dennis Woschko and Mrs. Stefanie Bügel for helpful assistance and discussion.

## References


1 Z. Klimont, S. Smith and J. Cofala, *Environ. Res. Lett.* 2013, **8**, 014003.

2 X. Xu, C. Chen, H. Qi, R. He, C. You and G. Xiang, *Fuel Process. Technol.*, 2000, **62**, 153-160.

3 P. Amoatey, H. Omidvarborna, M. S. Baawain and A. Al-Mamun, *Process Saf. Environ. Prot.*, 2019, **123**, 215-228.

4 M. Matooane and R. Diab, *Arch. Environ. Health*, 2003, **58**, 763-770.

5 F. C. Menz and H. M. Seip, *Environ. Sci. Policy*, 2004, **7**, 253-265.

6 J. Yang, L. Li, S. Wang, H. Li, J. S. Francisco, X. C. Zeng and Y. Gao, *J. Am. Chem. Soc.*, 2019, **141**, 19312-19320.

7 B. Wu, H. Tian, Y. Hao, S. Liu, X. Liu, W. Liu, X. Bai, W. Liang, S. Lin, Y. Wu, P. Shao, H. Liu and C. Zhu, *Environ. Sci. Technol.*, 2018, **52**, 14015-14026.

8 R. K. Srivastava and W. Jozewicz, *J. Air Waste Manag. Assoc.*, 2001, **51**, 1676-1688.

9 J.-Y. Lee, T. C. Keener and Y. J. Yang, *J. Air Waste Manag. Assoc.*, 2009, **59**, 725-732.

10 R. K. Srivastava, W. Jozewicz and C. Singer, *Environ. Prog.*, 2001, **20**, 219-228.

11 B. Rao and E. S. Rubin, *Environ. Sci. Technol.*, 2002, **36**, 4467-4475.

12 R. Pacciani, J. Torres, P. Solsona, C. Coe, R. Quinn, J. Hufton, T. Golden and L. F. Vega, *Environ. Sci. Technol.*, 2011, **45**, 7083-7088.

13 M. P. Suh, H. J. Park, T. K. Prasad and D.-W. Lim, *Chem. Rev.*, 2012, **112**, 782-835.

14 J.-R. Li, R. J. Kuppler and H.-C. Zhou, *Chem. Soc. Rev.*, 2009, **38**, 1477-1504.

15 J.-R. Li, J. Sculley and H.-C. Zhou, *Chem. Rev.*, 2012, **112**, 869-932.

16 J. B. DeCoste and G. W. Peterson, *Chem. Rev.*, 2014, **114**, 5695-5727.

17 H. Wang, W. P. Lustig and J. Li, *Chem. Soc. Rev.*, 2018, **47**, 4729-4756.

18 E. Martínez-Ahumada, M. L. Díaz-Ramírez, M. d. J. VelásquezHernández, V. Jancik and I. A. Ibarra, *Chem. Sci.*, 2021, **12**, 6772-6799.

19 T. Islamoglu, Z. Chen, M. C. Wasson, C. T. Buru, K. O. Kirlikovali, U. Afrin, M. R. Mian and O. K. Farha, *Chem. Rev.*, 2020, **120**, 8130-8160.

20 K. Sumida, D. L. Rogow, J. A. Mason, T. M. McDonald, E. D. Bloch, Z. R. Herm, T.-H. Bae and J. R. Long, *Chem. Rev.*, 2012, **112**, 724-781.

21 W. P. Mounfield, C. Han, S. H. Pang, U. Tumuluri, Y. Jiao, S. Bhattacharyya, M. R. Dutzer, S. Nair, Z. Wu, R. P. Lively, D. S. Sholl and K. S. Walton, *J. Phys. Chem. C*, 2016, **120**, 27230-27240.

22 M. R. Tchalala, P. M. Bhatt, K. N. Chappanda, S. R. Tavares, K. Adil, Y. Belmabkhout, A. Shkurenko, A. Cadiau, N. Heymans, G. Weireld, G. Maurin. K. N. Salama, and M. Eddaoudi. *Nat. Commun.*, 2019, **10**, 1328.

23 J. H. Carter, X. Han, F. Y. Moreau, I. da Silva, A. Nevin, H. G. W. Godfrey, C. C. Tang, S. Yang and M. Schröder, *J. Am. Chem. Soc.*, 2018, **140**, 15564-15567.

24 G. L. Smith, J. E. Eyley, X. Han, X. Zhang, J. Li, N. M. Jacques, H. G. W. Godfrey, S. P. Argent, L. J. McCormick McPherson, S. J. Teat, Y. Cheng, M. D. Frogley, G. Cinque, S. J. Day, C. C. Tang, T. L. Easun, S. Rudić, A. J. Ramirez-Cuesta, S. Yang and M. Schröder, *Nat. Mater.*, 2019, **18**, 1358-1365.

25 P. Brandt, A. Nuhnen, S. Öztürk, G. Kurt, J. Liang and C. Janiak, *Adv. Sustain. Syst.*, 2021, **5**, 2000285.

26 Y. Zhang, P. Zhang, W. Yu, J. Zhang, J. Huang, J. Wang, M. Xu, Q. Deng, Z. Zeng and S. Deng, *ACS Appl. Mater. Interfaces*, 2019, **11**, 10680-10688.

27 L. Li, I. da Silva, D. I. Kolokolov, X. Han, J. Li, G. Smith, Y. Cheng, L. L. Daemen, C. G. Morris, H. G. W. Godfrey, N. M. Jacques, X. Zhang, P. Manuel, M. D. Frogley, C. A. Murray, A. J. Ramirez-Cuesta, G. Cinque, C. C. Tang, A. G. Stepanov, S. Yang and M. Schröder, *Chem. Sci.*, 2019, **10**, 1472-1482.

28 X. Cui, Q. Yang, L. Yang, R. Krishna, Z. Zhang, Z. Bao, H. Wu, Q. Ren, W. Zhou, B. Chen and H. Xing, *Adv. Mater.*, 2017, **29**, 1606929.

29 P. Brandt, A. Nuhnen, M. Lange, J. Möllmer, O. Weingart and C. Janiak, *ACS Appl. Mater. Interfaces*, 2019, **11**, 17350-17358.

30 M. Savage, Y. Cheng, T. L. Easun, J. E. Eyley, S. P. Argent, M. R. Warren, W. Lewis, C. Murray, C. C. Tang, M. D. Frogley, G. Cinque, J. Sun, S. Rudić, R. T. Murden, M. J. Benham, A. N. Fitch, A. J. Blake, A. J. Ramirez-Cuesta, S. Yang and M. Schröder, *Adv. Mater.*, 2016, **28**, 8705-8711.

31 E. Martínez-Ahumada, M. L. Díaz-Ramírez, H. A. Lara-García, D. R. Williams, V. Martis, V. Jancik, E. Lima and I. A. Ibarra, *J. Mater. Chem. A*, 2020, **8**, 11515-11520.

32 Ü. Kökçam-Demir, A. Goldman, L. Esrafili, M. Gharib, A. Morsali, O. Weingart and C. Janiak, *Chem. Soc. Rev.*, 2020, **49**, 2751-2798.

33 P. Brandt, S.-H. Xing, J. Liang, G. Kurt, A. Nuhnen, O. Weingart and C. Janiak, *ACS Appl. Mater. Interfaces*, 2021, **13**, 29137-29149.

34 F. Chen, D. Lai, L. Guo, J. Wang, P. Zhang, K. Wu, Z. Zhang, Q. Yang, Y. Yang, B. Chen, Q. Ren and Z. Bao, *J. Am. Chem. Soc.*, 2021, **143**, 9040-9047.

35 S. Xing, J. Liang, P. Brandt, F. Schäfer, A. Nuhnen, T. Heinen, I. Boldog, J. Möllmer, M. Lange, O. Weingart and C. Janiak, *Angew. Chem. Int. Ed.*, 2021, **60**, 17998-18005.

36 Y. Lin, H. Lin, H. Wang, Y. Suo, B. Li, C. Kong and L. Chen, *J. Mater. Chem. A*, 2014, **2**, 14658-14665.

37 F. P. Kinik, A. Uzun and S. Keskin, *ChemSusChem*, 2017, **10**, 2842-2863.

38 Cota and F. Fernandez Martinez, *Coord. Chem. Rev.*, 2017, **351**, 189-204.

39 D. K. Yoo, N. Abedin Khan and S. H. Jhung, *J. CO2 Util.*, 2018, **28**, 319-325.

40 Q.-X. Luo, B.-W. An, M. Ji and J. Zhang, *Mater. Chem. Front.*, 2018, **2**, 219-234.

41 J. Liang, S. Xing, P. Brandt, A. Nuhnen, C. Schlüsener, Y. Sun and C. Janiak, *J. Mater. Chem. A*, 2020, **8**, 19799-19804.

42 S. Lim, H. Kim, N. Selvapalam, K.-J. Kim, S. J. Cho, G. Seo and K. Kim, *Angew. Chem. Int. Ed.*, 2008, **47**, 3352-3355.

43 J. Tian, J. Liu, J. Liu and P. K. Thallapally, *CrystEngComm*, 2013, **15**, 1528-1531.

44 J. Liang, A. Nuhnen, S. Millan, H. Breitzke, V. Gvilava, G. Buntkowsky and C. Janiak, *Angew. Chem. Int. Ed.*, 2020, **59**, 6068-6073.

45 Match! – phase analysis using powder diffraction, 2019 (v.3.5.3.109), H. Putz – Crystal Impact GbR, 53227 Bonn, Germany.

46 T. Zhao, F. Jeremias, I. Boldog, B. Nguyen, S. K. Henninger and C. Janiak, *Dalton Trans.*, 2015, **44**, 16791-16801.

47 G. Férey, C. Mellot-Draznieks, C. Serre, F. Millange, J. Dutour, S. Surblé and I. Margiolaki, *Science*, 2005, 309, 2040.

48 G. Férey, C. Mellot-Draznieks, C. Serre and F. Millange, *Acc. Chem. Res.*, 2005, **38**, 217-225.

49 J. Liang, Y.-Q. Xie, X.-S. Wang, Q. Wang, T.-T. Liu, Y.-B. Huang and R. Cao, *Chem. Commun.*, 2018, **54**, 342-345.

50 Buyukcakir, S. H. Je, S. N. Talapaneni, D. Kim and A. Coskun, *ACS Appl. Mater. Interfaces*, 2017, **9**, 7209-7216.

51 S. M. Towsif Abtab, D. Alezi, P. M. Bhatt, A. Shkurenko, Y. Belmabkhout, H. Aggarwal, Ł. J. Weseliński, N. Alsadun, U. Samin, M. N. Hedhili and M. Eddaoudi, *Chem*, 2018, **4**, 94-105.

52 Y. Shen, T. Pan, P. Wu, J. Huang, H. Li, E. Khalil Islam, S. Li, B. Zheng, J. Wu, Q. Wang, W. Zhang, D. Wei Wei and F. Huo, *CCS Chem.*, 2020, **2**, 1607–1614.

53 X. Huang, Q. Hu, L. Gao, Q. Hao, P. Wang and D. Qin, *RSC Adv.*, 2018, **8**, 27623-27630.

54 M. Saikia and L. Saikia, *RSC Adv.*, 2016, **6**, 14937-14947.

55 F. Zhang, Y. Jin, Y. Fu, Y. Zhong, W. Zhu, A. A. Ibrahim and M. S. El-Shall, *J. Mater. Chem. A*, 2015, **3**, 17008-17015.

56 S. H. Overbury, D. R. Mullins, D. R. Huntley and L. Kundakovic, *J. Phys. Chem. B*, 1999, **103**, 11308-11317.

57 E. J. Romano and K. H. Schulz, *Appl. Surf. Sci.*, 2005, **246**, 262-270.

58 H. C. Yoon, P. B. S. Rallapalli, H. T. Beum, S. S. Han and J.-N. Kim, *Energy Fuels*, 2018, **32**, 1365-1373.

59 H. B. Tanh Jeazet, C. Staudt and C. Janiak, *Chem. Commun.*, 2012, **48**, 2140-2142.

60 M. Thommes, K. Kaneko, V. Neimark Alexander, P. Olivier James, F. Rodriguez-Reinoso, J. Rouquerol and S. W. Sing, *Pure Appl. Chem.*, 2015, **87**, 1051-1069.

61 Z. Zhang, B. Yang and H. Ma, *Sep. Purif. Technol.*, 2021, **259**, 118164.

62 Nuhnen and C. Janiak, *Dalton Trans.*, 2020, **49**, 10295-10307.

63 M. Ebrahim, B. Levasseur and T. J. Bandosz, *Langmuir*, 2013, **29**, 168-174.

64 L. Goodman, P. Li, C. R. Usher and V. H. Grassian, *J. Phys. Chem. A*, 2001, **105**, 6109-6120.

65 K. Tan, P. Canepa, Q. Gong, J. Liu, D. H. Johnson, A. Dyevoich, P. K. Thallapally, T. Thonhauser, J. Li and Y. J. Chabal, *Chem. Mater.*, 2013, **25**, 4653-4662.

66 Z. Zhou, B. Cheng, C. Ma, F. Xu, J. Xiao, Q. Xia and Z. Li, *RSC Adv.*, 2015, **5**, 94276-94282.

67 M. Waqif, A. M. Saad, M. Bensitel, J. Bachelier, O. Saur and J.-C. Lavalley, *J. Chem. Soc., Faraday Trans.*, 1992, **88**, 2931-2936.

68 W. P. Mounfield, U. Tumuluri, Y. Jiao, M. Li, S. Dai, Z. Wu and K. S. Walton, *Micropor. Mesopor. Mater.*, 2016, **227**, 65-75.

69 N. Tannert, Y. Sun, E. Hastürk, S. Nießing and C. Janiak, *Z. Anorg. Allg. Chem.*, 2021, **647**, 1124–1130.

70 K. Wang, D. Feng, T.-F. Liu, J. Su, S. Yuan, Y.-P. Chen, M. Bosch, X. Zou and H.-C. Zhou, *J. Am. Chem. Soc.*, 2014, **136**, 13983-13986.

71 K. Leus, T. Bogaerts, J. De Decker, H. Depauw, K. Hendrickx, H. Vrielinck, V. Van Speybroeck and P. Van Der Voort, *Micropor.* Mesopor. *Mater.*, 2016, **226**, 110-116.

72 J. Canivet, A. Fateeva, Y. Guo, B. Coasne and D. Farrusseng, *Chem. Soc. Rev.*, 2014, **43**, 5594-5617.

73 Khutia, H. U. Rammelberg, T. Schmidt, S. Henninger and C. Janiak, *Chem. Mater.*, 2013, **25**, 790-798.

Electronic Supplementary Information (ESI)

# Cucurbit[6]uril@MIL-101-Cl: loading polar porous cages in mesoporous stable host for enhanced $SO_2$ adsorption at low pressures

Yangyang Sun,[a] Jun Liang,[a,b] Philipp Brandt,[a] Alex Spieß,[a] Secil Öztürk[a] and Christoph Janiak*[a,b]

[a] Institut für Anorganische Chemie und Strukturchemie, Heinrich-Heine-Universität, 40204 Düsseldorf, Germany.

[b] Hoffmann Institute of Advanced Materials, Shenzhen Polytechnic, 7098 Liuxian Blvd, Nanshan District, Shenzhen 518055, China.

Corresponding author:

E-mail: janiak@uni-duesseldorf.de; Fax: + 49-211-81-12287; Tel: +49-211-81-12286

Additional email addresses:

Yangyang.Sun@uni-duesseldorf.de; liangj956@nenu.edu.cn; p.brandt@hhu.de; alex.spiess@hhu.de; oeztues@uni-duesseldorf.de.

Table of Contents

**Table S1** Sources for starting materials and solvents.

| Items | Manufacturer |
|---|---|
| Chromium (III) nitrate nonahydrate | Acros Organics |
| Benzene-1,4-dicarboxylic acid, $H_2BDC$ | Acros Organics |
| Urea (> 99.5%) | Sigma–Aldrich |
| Paraformaldehyde | Carl Roth |
| Glyoxal (40 wt%) | J&K company |
| *N,N*-dimethylformamide | Fisher Chemicals |
| Nitric acid (65 wt%) | Fisher Chemicals |
| Hydrochloric acid (37 wt%) | Sigma–Aldrich |
| Methanol | Sigma–Aldrich |
| Ethanol | Sigma–Aldrich |
| Natrium metabisulfite ($Na_2S_2O_5$) | Merck |
| Sodium chloride | Fischer Scientific |

**Elemental Analysis:**

As a porous material CB6@MIL-101-Cl will adsorb water (humidity) from ambient air during storage and handling in air. Such water content will not give a meaningful CHN analysis as was seen by too high H wt% values.

Therefore, a small amount of sample was activated at 150 °C overnight under vacuum ($1\times 10^{-2}$ bar), then cooled to room temperature and stored under nitrogen. For CHN analysis the sample was quickly weighed and directly measured.

MIL-101-Cl: $[Cr_3OCl(H_2O)_2(C_8H_4O_4)_3]$ $M_w$ = 735.82 g/mol from which M(C) = is 288.26 g/mol.

CB6: $C_{36}H_{36}N_{24}O_{12}$ $M_w$ = 996.84 g/mol; from which M(N) = is 336.16 g/mol and M(C) = 432.39 g/mol

Found (%) C: 40.35, H: 2.82, N: 10.45

Assuming a formula of the composite as $[Cr_3OCl(H_2O)_2(C_8H_4O_4)_3][C_{36}H_{36}N_{24}O_{12}]_a$ then for the mass fraction of N (w(N) = 0.1045) and C (w(C) = 0.4035), we can establish the two equations:

N: w(N) = 336.16 × a : (735.82 + 996.84 × a) (1)

C: w(C) = (288.26 + 432.39 × a) : (735.82 + 996.84 × a ) (2)

or (1) divided by (2)

w(N)/w(C) = 336.16 × a : (288.26 + 432.39 × a)

336.16 × a = w(N)/w(C) × (288.26 + 432.39 × a)

336.16 × a – w(N)/w(C) × 432.39 × a = w(N)/w(C) × 288.26

a = w(N)/w(C) × 288.26 : (336.16 – w(N)/w(C) × 432.39)

w(N)/w(C) = 0.2590

**giving a = 0. 333**

Then with **a = 0. 333** the total molecular weight of the composite $[Cr_3OCl(H_2O)_2(C_8H_4O_4)_3][C_{36}H_{36}N_{24}O_{12}]_{0.333}$ is 1067.77 g/mol.

For this, the calculated weight-% of H is 2.65; to be compared with found H 2.82%.

Thus, the weight percentage of CB6 in the CB6@MIL-101-Cl then is (0.333 × 996.84 / 1067.77) × 100% = 31 wt%.

The composition of the composite was assessed in previous work based on elemental analysis data and digestion NMR as 29 wt% of CB6 in MIL-101(Cr).[1]


**Scheme S1** Setup for humid $SO_2$ exposure experiments. a) $SO_2$ sensor, b) Hygrometer, c) Flowmeter, d) Natrium metabisulfite solution ($Na_2S_2O_5$), e) Sodium chloride solution, f) $H_2O$.

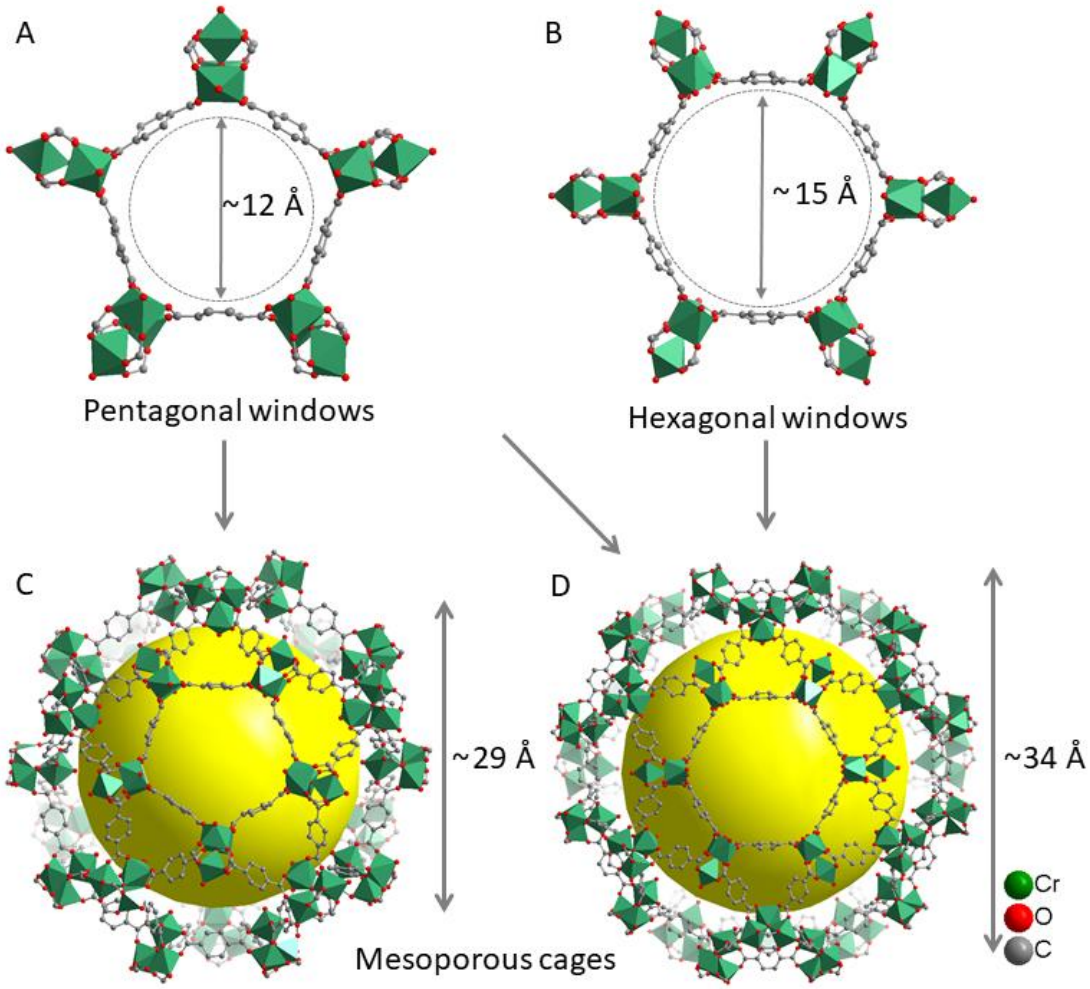


**Scheme S2** Schematic representation of the MIL-101 structure. Graphics have been drawn with the software DIAMOND from the deposited cif-files under CCDC no. 605510, Refcode OCUNAC for MIL-101(Cr).[2]

**Table S2** Textural properties of MIL-101, CB6@MIL-101-Cl and nanoCB6-H.

| | $S_{BET}$[a] [$m^2 g^{-1}$] | $V_{total}$[b] [$cm^3 \cdot g^{-1}$] | $V_{micro}$[c] [$cm^3 g^{-1}$] |
|---|---|---|---|
| MIL-101 | 3217 | 1.54 | 1.17 |
| CB6@MIL-101-Cl | 2077 | 1.00 | 0.81 |
| nanoCB6-H | 435 | 0.24 | 0.11 |

[a] BET surface area was determined over 7 points in the relative pressure range $p/p_0$ = 0.05–0.2 from $N_2$ sorption isotherms at 77 K for MIL-101 and CB6@MIL-101-Cl ($p/p_0$ =0.02–0.08 for nanoCB6-H).

b Total pore volumes ($V_{total}$) were determined from $N_2$ sorption isotherms at 77 K ($p/p_0$ = 0.90).

c Micropore volumes were determined using the t–plot method from five adsorption points in the pressure range $p/p_0$ = 0.2 - 0.4 based on N2 adsorption curves at 77 K.

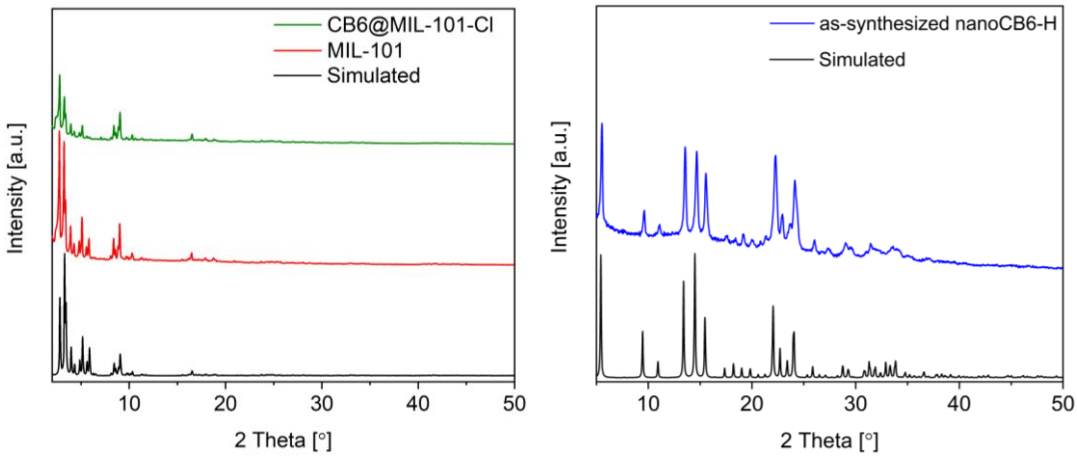


**Fig. S1** PXRD patterns of MIL-101, composite CB6@MIL-101-Cl (left) and nanoCB6-H (right). Simulations from the deposite cif file with CCDC no. 605510, Refcode OCUNAC for MIL-101(Cr)[Error! Bookmark not defined.] and with CCDC no. 676880, Refcode KOBNEV for CB6-H.[3]

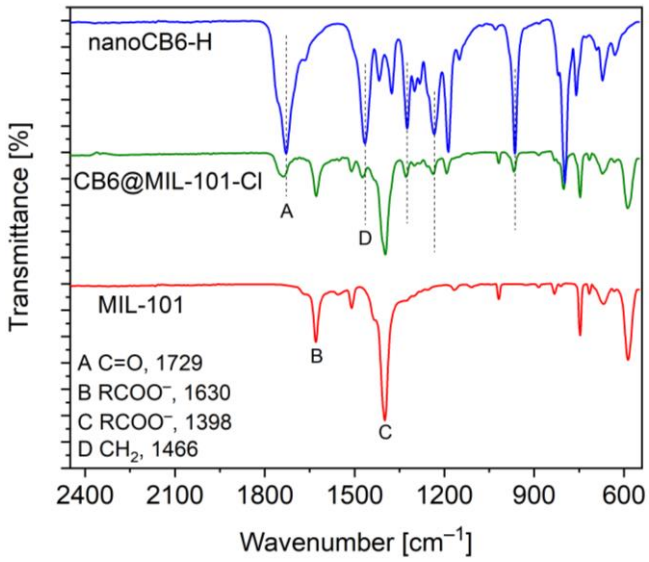


**Fig. S2** FT-IR spectra of nanoCB6-H, MIL-101 and CB6@MIL-101-Cl.

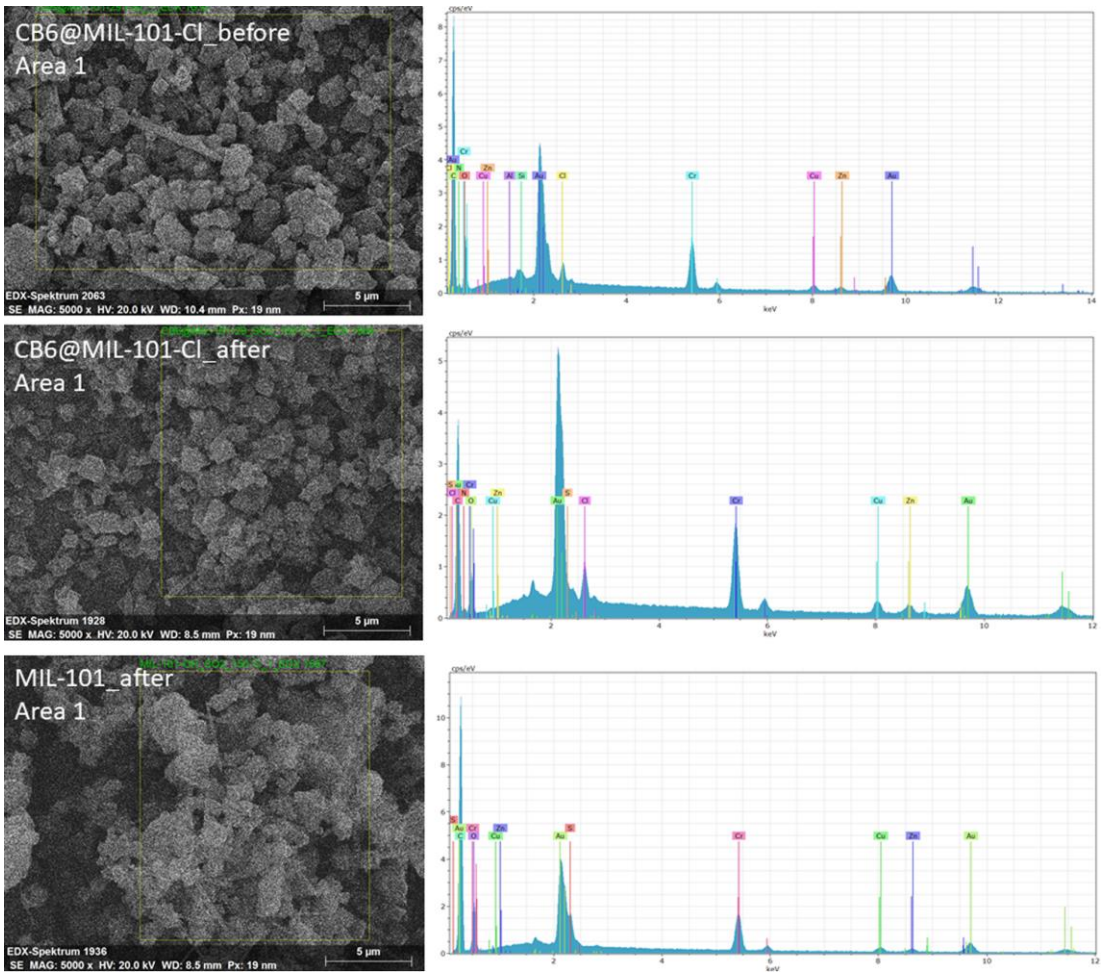


**Fig. S3** SEM images and corresponding EDX spectra of CB6@MIL-101-Cl and MIL-101 before and after one-cycle of $SO_2$ adsorption-desorption. Area 1 (whole region) is shown here as the example for other two areas (part region).

In CB6@MIL-101-Cl, EDX cannot be used for sulfur quantification due to the vicinity/ overlap of the Au and S peak. It is evident that the samples before $SO_2$ sorption also exhibit the same "S shoulder" due to the strong background signal in this energy region.

**Table S3** EDX-based elemental composition of $Cl/Cr_3$ atom-group ratios in CB6@MIL-101-Cl and MIL-101 before and after one-cycle of $SO_2$ adsorption-desorption.[a]

| | | | Cr [At%] | Cl [At%] | Cl/Cr | $Cl/Cr_3$ (Aver.) |
|---|---|---|---|---|---|---|
| **CB6@MIL-101-Cl** | before | Area 1 | 2.46 | 0.55 | 0.22 | 0.78 |
| | | Area 2 | 3.22 | 0.93 | 0.29 | |
| | | Area 3 | 2.71 | 0.74 | 0.27 | |
| | after | Area 1 | 4.78 | 1.15 | 0.24 | 0.69 |
| | | Area 2 | 2.47 | 0.56 | 0.23 | |
| | | Area 3 | 1.05 | 0.23 | 0.22 | |
| **MIL-101** | after | Area 1 | 2.41 | — | — | — |
| | | Area 2 | 3.15 | — | — | |
| | | Area 3 | 3.09 | — | — | |

[a] The concomitant SEM images and EDX spectra are shown in Fig. S3.

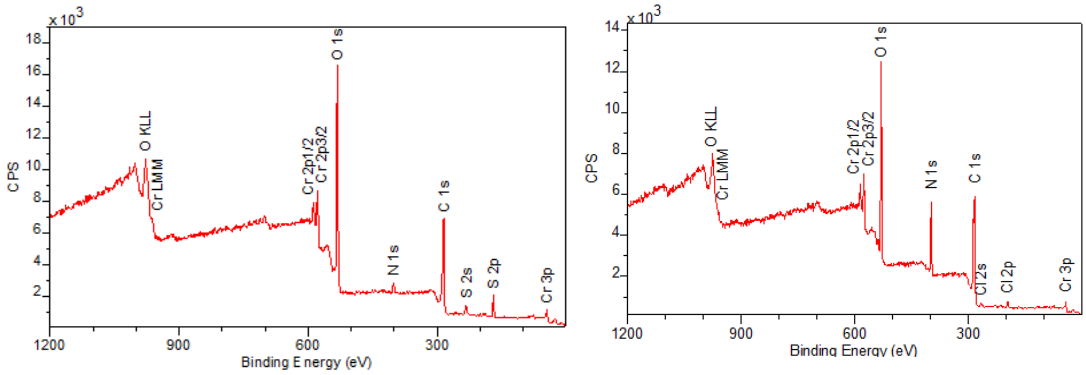


**Fig. S4** XPS survey spectra of MIL-101 (left) and CB6@MIL-101-Cl (right). The trace amount of nitrogen in MIL-101 is due to the residual DMF solvent, which was used for washing the samples.

**Table S4** XPS-based elemental composition of $Cl/Cr_3$ and $S/Cr_3$ atom-group ratios in CB6@MIL-101-Cl and MIL-101 after one-cycle of $SO_2$ adsorption-desorption.

| | Cr | | Cl | | S | | $Cl/Cr_3$ | $S/Cr_3$ |
|---|---|---|---|---|---|---|---|---|
| | **Area** | **At%** | **Area** | **At%** | **Area** | **At%** | | |
| **CB6@MIL-101-Cl** | 123.08 | 2.58 | 44.33 | 0.93 | — | — | 1.08 | — |
| **MIL-101** | 181.88 | 3.56 | — | — | 256.53 | 5.02 | — | 4.23 |

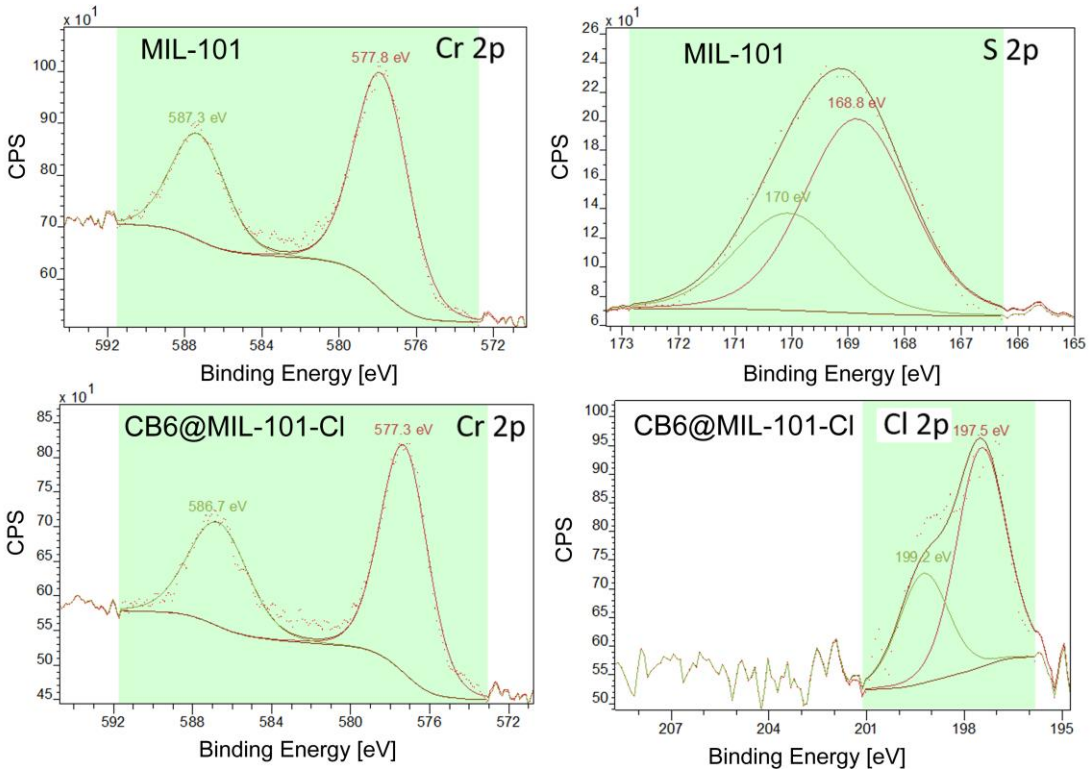


**Fig. S5** High-resolution Cr 2p XPS spectra of MIL-101 and CB6@MIL-101-Cl, high-resolution S 2p spectrum in MIL-101 and high-resolution Cl 2p spectrum in CB6@MIL-101-Cl after one-cycle of $SO_2$ adsorption-desorption followed by activation at 150 °C under vacuum.

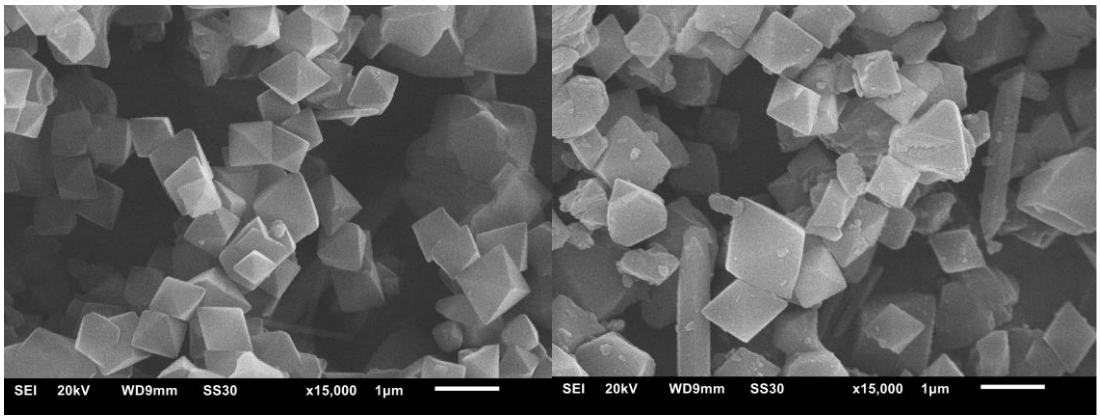


**Fig. S6** Scanning electron microscopy (SEM) images for MIL-101 (left) and CB6@MIL-101-Cl (right). The scale bar in both images is 1μm.

**$SO_2$-sorption isotherm fitting**

The fitting of adsorption isotherms of $SO_2$ yields affinity constants. Fitting-simulations were calculated using the 3P sim software.[4] We applied the dual-site Langmuir (DSL) model (eq. S1) on the isotherm data. Fitting parameters are shown in Table S5.

DSL: $$q_{eq} = q_{max1}\frac{\cdot K_1 \cdot p}{1+K_1 \cdot p} + q_{max2}\frac{\cdot K_2 \cdot p}{1+K_2 \cdot p} \quad \text{(S1)}$$

$q_{eq}$= amount adsorbed [mmol/g]

$q_{max}$ = maximum adsorption capacity [mmol/g]

$K_1$, $K_2$ = affinity constant for adsorption at site 1, 2 [1/bar]

$p$ = pressure [kPa]

**Table S5** Dual-site Langmuir fitting parameters for $SO_2$ at 293 K calculated using 3P sim software.[a,4]

| | Model | $R^2$ | Affinity const. $K_1$ [1/bar] | Max. loading [mmol/g] | Affinity const. $K_2$ [1/bar] | Max. loading 2 [mmol/g] |
|---|---|---|---|---|---|---|
| CB6@MIL-101-Cl | DSL | 0.999 | 78.282 | 4.323 | 0.378 | 57.502 |
| MIL-101 | DSL | 0.999 | 3.083 | 12.335 | 0.302 | 82.750 |
| nanoCB6-H | DSL | 0.998 | 427.341 | 3.488 | 0.522 | 8.694 |

[a] DSL_ Dual-site Langmuir. The number of three decimal digits may be needed for the IAST selectivity calculation. Rounding to one decimal digit leads to significant deviations in the IAST values. The corresponding fitting curves are shown in Fig. S7.

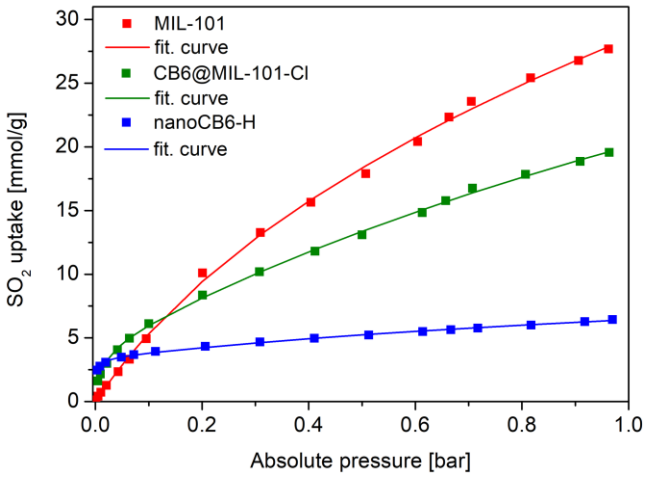


**Fig. S7** Experimental $SO_2$ sorption isotherm and corresponding fitting curves of MIL-101 (red), CB6@MIL-101 (green) and nanoCB6-H (blue).

**Table S6** Comparison of $SO_2$ sorption data for MOFs.

The criteria for the stability and/or durability of MOFs are based on the combination of the unchanged PXRD pattern and a decrease in surface area by less than 10% after dry and humid $SO_2$ compared to the pristine MOF. In addition or alternatively, the maximal $SO_2$ uptake of multiple individual gas adsorption measurements or the cyclic breakthrough measurement decreased by less than 20% at the second run and kept an insignificant uptake change in the following runs.

| Material | BET surface area [$m^2 \cdot g^{-1}$] | $SO_2$ uptake [$mmol \cdot g^{-1}$] | | Temp. [K] | Stability and/or reusability | Reference |
|---|---|---|---|---|---|---|
| | | 0.01 bar | 1 bar | | | |
| CB6@MIL-101-Cl | 2077 | 2.2 | 19.5 | 293 | yes | This work |
| | | 2.0 | 17.0 | 298 | | |
| nanoCB6-H | 435 | 2.8 | 6.5 | 293 | no | This work |
| MIL-101 | 3217 | 0.7 | 27.7 | 293 | no | This work |
| | | 0.6 | 24.4 | 298 | | |
| SIFSIX-2-Cu-i | 630 | 4.2 | 6.9 | 298 | yes [c] | 5 |
| MIL-160 | 1170 | 4.2 | 7.2 | 293 | yes [d] | 6 |
| DMOF-TM | 900 | 3.8 | 9.7 | 293 | yes [e] | 7 |
| SIFSIX-1-Cu | 1337 | 3.4 | 11.01 | 298 | yes [f] | 5 |
| MFM-305 | 779 | 3.3[a] | 7 | 298 | unclear [g] | 8 |
| MFM-305-$CH_3$ | 256 | 3[a] | 5.2 | 298 | unclear [g] | 8 |
| $NH_2$-MIL-125(Ti) | 1560 | 3 | 10.8 | 293 | no [h] | 6 |
| mmen-MIL-101(Cr) | 2377 | 3 | — | 298 | yes [i] | 9 |
| SIFSIX-3-Ni | 223 | 2.4 | 2.7 | 298 | probably no [j] | 5 |
| MOF-808 | 1190 | 2.1 | 14.6 | 293 | no [k] | 10 |
| $NH_2$-MIL-53(Al) | 1120 | 2.0 | 8.0 | 293 | no [l] | 10 |
| HKUST-1 | 1490 | 2.0 | 13.8 | 293 | yes | 11 |
| SIFSIX-3-Zn | 250 | 1.7 | 2.1 | 298 | probably no [j] | 5 |
| MFM-300(In) | 1071 | 1.6[a] | 8.28 | 298 | yes [m] | 12 |
| MFM-601 | 3644 | 1.6[a] | 12.3 | 298 | / | 13 |
| $NH_2$-MIL-101(Al) | 1770 | 1.5 | 17.3 | 293 | no[n] | 10 |
| Mg-MOF-74 | 1206 | 1.4[a] | 8.6 | 298 | / | 14,15 |
| Zr-Fum | 600 | 1.3 | 6.5 | 293 | yes | 10 |
| MIL-101(Cr)-4F(1%) | 2176 | 1.3[a] | 18.4 | 298 | yes | 16 |
| $NH_2$-MIL-101(Cr) | 2290 | 1.2 | 16.7 | 293 | no | 11 |
| CAU-10-H | 600 | 1.2 | 4.8 | 293 | no | 10 |
| MIL-96(Al) | 530 | 1.2 | 6.5 | 293 | no[n] | 10 |
| Al-Fum | 970 | 1.0 | 7.5 | 293 | no | 10 |
| $[Zn_2(L1)_2(bpe)]$ | 275 | 0.7[a] | 6.4 | 293 | yes (only PXRD) | 17 |
| Basolite F300 | 1070 | 0.6 | 9.5 | 293 | no | 11 |
| MFM-170 | 2408 | 0.5[a] | 17.5 | 298 | yes | 18 |
| MFM-202a | 2220 | 0.4[a] | 10.2[b] | 298 | no | 19 |

| Material | BET surface area [$m^2 \cdot g^{-1}$] | $SO_2$ uptake [$mmol \cdot g^{-1}$] | | Temp. [K] | Stability and/or reusability | Reference |
|---|---|---|---|---|---|---|
| | | 0.01 bar | 1 bar | | | |
| $Ni(bdc)(ted)_{0.5}$ | 1738 | 0.3[a] | 10 | 298 | yes (only PXRD) | 15 |
| MOF-177 | 4100 | 0.25 | 25.7 | 293 | no | 6 |

[a] Estimated from isotherm [b] MFM-202a undergoes a distinct irreversible framework phase transition upon $SO_2$ uptake at 268–283 K to give MFM-202b which has enhanced stability.

[c] The breakthrough performance did not decline through cyclic breakthrough tests for 6 cycles, PXRD indicates the stability after breakthrough.

[d] Evaluated by multiple individual $SO_2$ sorption runs. MIL-160 shows stability with insignificant reduction of the gas uptake over 5 runs.

[e] The sample was exposed to dry and humid $SO_2$ for 6 hours, respectively. Its stability was evaluated from PXRD and BET surface area (90%), and from the breakthrough experiments for 3 cycles.

[f] The breakthrough performance did not decline through cyclic breakthrough tests for 4 cycles, PXRD indicates the stability after breakthrough.

[g] For MFM-305 and MFM-305-$CH_3$, no experimental data or graphic for stability is found, only one sentence refers to the stability: "the $SO_2$ uptake is fully reversible in both materials, and no loss of crystallinity or porosity was observed for the regenerated samples."

[h] $NH_2$-MIL-125(Ti) displayed a reduced $SO_2$ uptake in the second run and then stabilized its adsorption capacity at the third run. The surface area of $NH_2$-MIL-125 deceased by about 20% under dry and humid $SO_2$. In the second $SO_2$ run, the maximal $SO_2$ uptake decreased by 22%.

[i] The sample after exposure to pure $SO_2$ was evaluated by PXRD and $N_2$ adsorption, which indicated the crystalline and porosity of the sample were preserved. Cyclic breakthrough experiment displayed a $SO_2$ uptake in the second run (83%) and then kept unchanged during 5 cycles.

[j] In the combined work is mentioned that "SIFSIX-1-Cu and SIFSIX-2-Cu-i fulfill the requirements by FGD technology, natural-gas purification and other $SO_2$-separation processes for both $SO_2$ capacity and selectivity." but there is no experimental stability data of SIXSIF-3-Ni and SIFSIX-3-Zn given.

[k] Under dry $SO_2$ exposure, MOF-808 is stable, but after humid $SO_2$ exposure, the surface area decreased to about 65%.

[l] After humid $SO_2$ exposure, the surface area of NH2-MIL-53(Al) decreased by more than 50%.

[m] MFM-300(In) displays complete retention of the framework structure upon contact with $SO_2$, $H_2SO_3$, and $H_2SO_4$ (verified by PXRD and SEM), demonstrating the excellent stability of this material for $SO_2$ capture in both dry and humid conditions.

n Under dry $SO_2$ exposure, $NH_2$-MIL-100(Al) and MIL-96(Al) had already demonstrated a major loss of porosity, and thus were deemed $SO_2$-unstable.

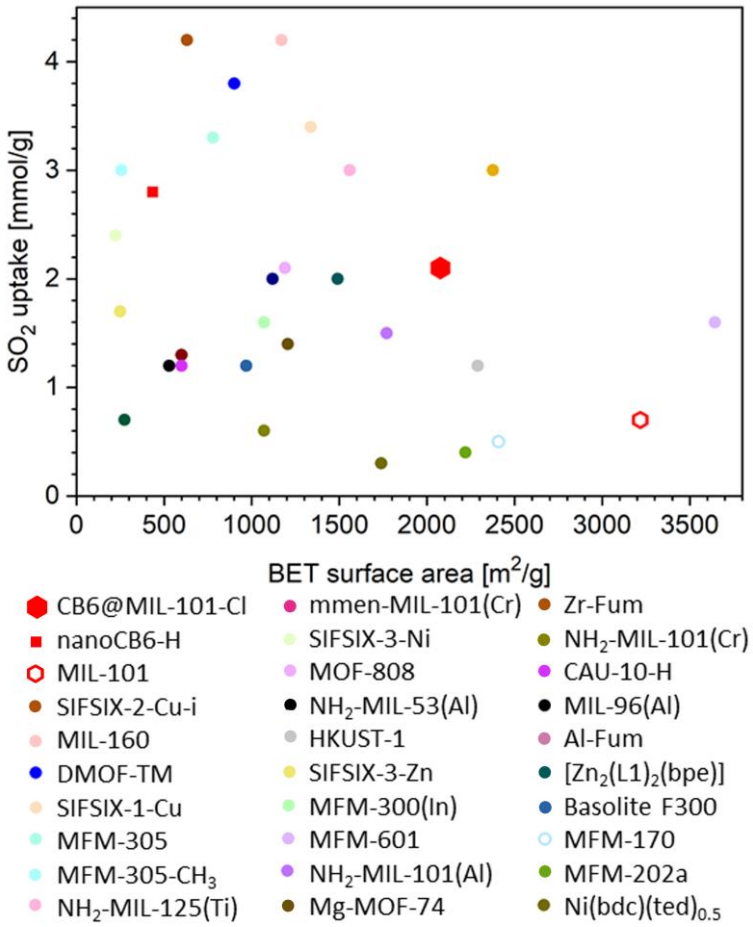


**Fig. S8** Comparison of $SO_2$ uptakes of reported MOFs at 0.01 bar and 293 K or 298 K. Plot of $SO_2$ adsorption against BET surface area (Open symbols denote the possible presence of open metal sites in the MOF).

**Isosteric enthalpy of adsorption**

Virial analysis

To calculate the isosteric enthalpy of adsorption ($\Delta H_{ads}$) for $SO_2$ isotherm data, we applied the virial method to fit the adsorption data simultaneously at 273 K and 293 K in Origin from equation (eq. S2)[20] (Ref. OriginLab Corporation, OriginPro, Version 9.0.0G., OriginLab Corporation 1991-2012.).

$$\ln(P) = \ln(n) + \frac{1}{T}\sum_{i=0}^{m} a_i n^i + \sum_{i=0}^{m} b_i n^i \qquad \text{(S2)}$$

In Eq. (1), $P$ is the pressure in kPa, $n$ is the total amount adsorbed in mmol/g, $T$ is the temperature in K (here 273K, 293K),$a_i$ and $b_i$are virial coefficients, and $m$ stands for the number of coefficients required to adequately fit the isotherms.

Therefore, $\Delta H_{ads}$ can be calculated from equation (eq. S3), where $R$ is the universal gas constant.

$$\Delta H_{ads} = -Q_{st} = R\sum_{i=0}^{m} a_i n^i \qquad \text{(S3)}$$

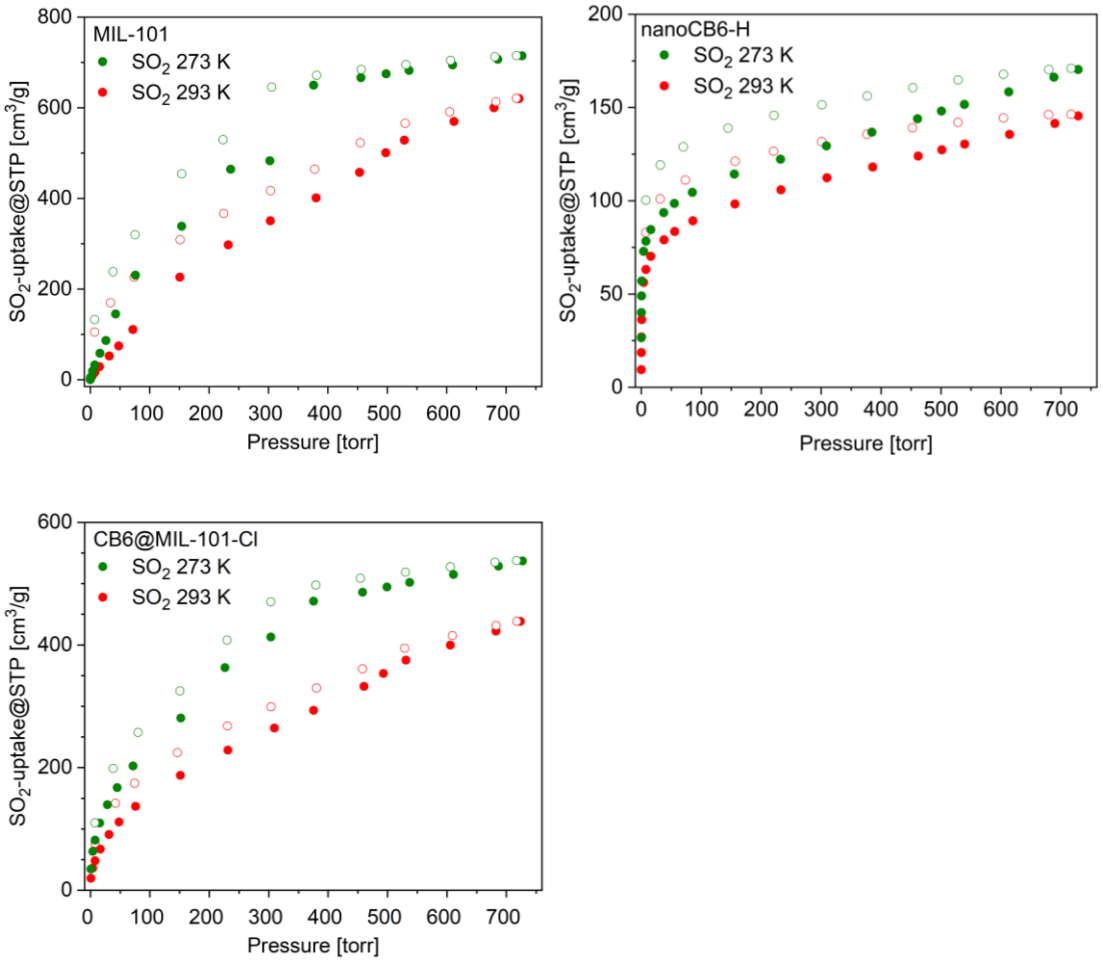


**Fig. S9** $SO_2$ adsorption isotherms of MIL-101, nanoCB6-H and CB6@MIL-101-Cl at 293 K and 273 K.

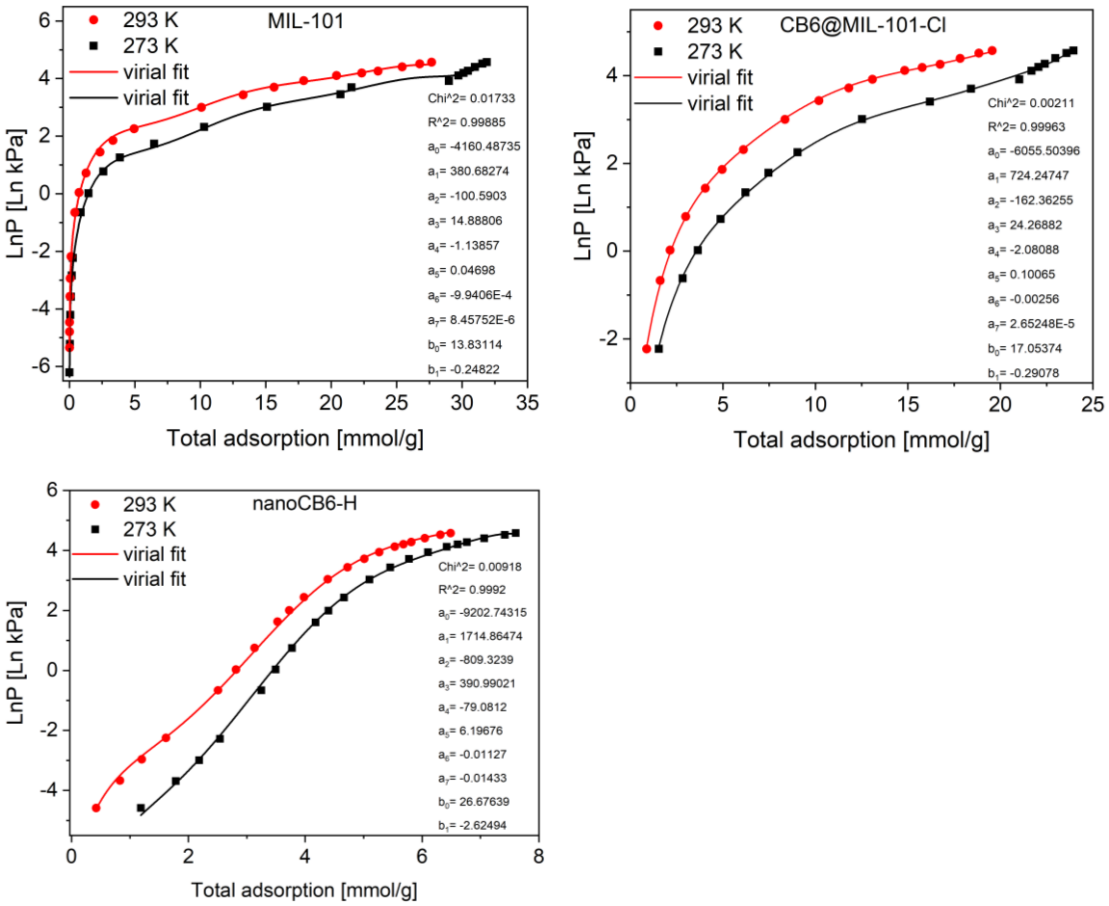


**Fig. S10** Virial analysis for heat of adsorption of MIL-101, CB6@MIL-101-Cl and nanoCB6-H from $SO_2$ adsorption at 273 K and 293 K.

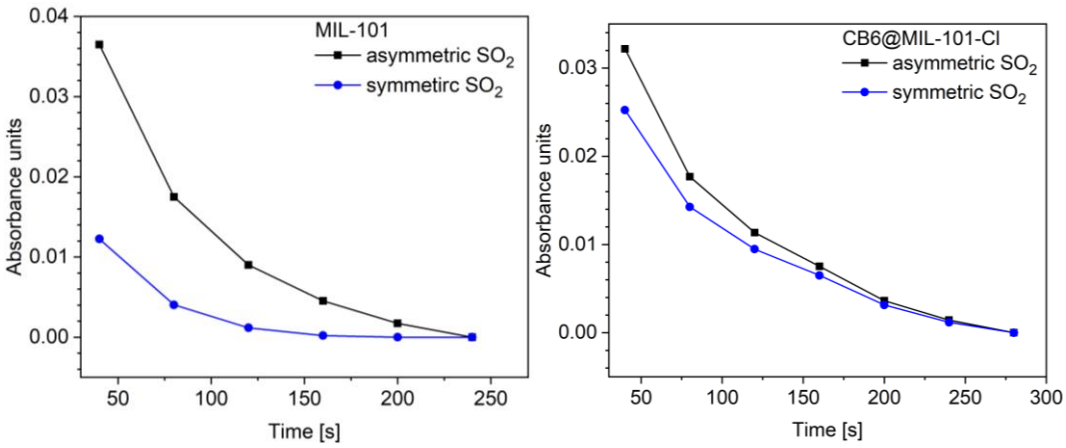


**Fig. S11** Intensity change of absorbance bands at ~1330 (black) and ~1144 $cm^{-1}$ (blue) of MIL-101 (left) and CB6@MIL-101-Cl (right) as a function of time, corresponding to the asymmetric and symmetric stretching vibration of physisorbed $SO_2$.

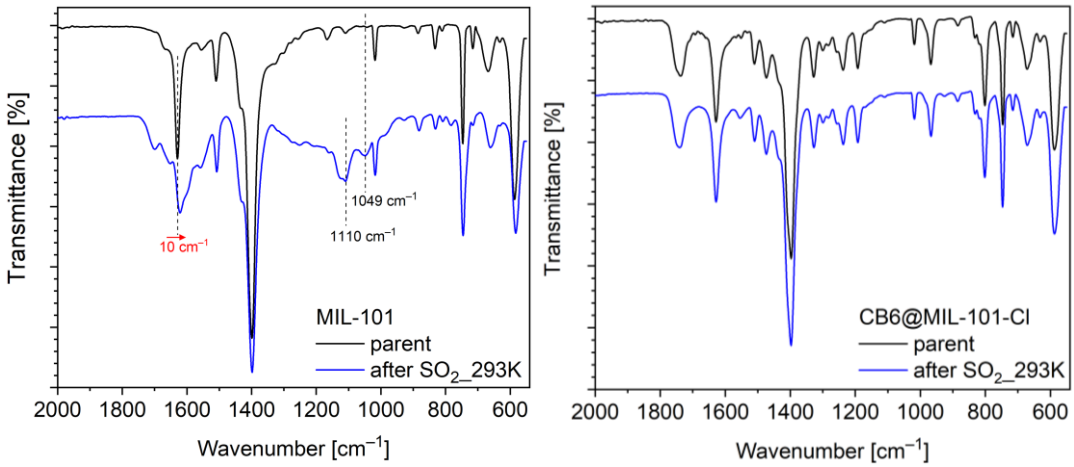


**Fig. S12** FT-IR spectra of MIL-101 and CB6@MIL-101-Cl before and after one-cycle full $SO_2$ adsorption-desorption at 293 K followed by degassing at 150 °C and 1 × $10^{-3}$ mbar for 12 h. We note that the peak at slightly below 700 $cm^{-1}$ in MIL-101 and CB6@MIL-101 exists in non-degassed samples prior to FT-IR measurements, however, it vanishes when the sample is well degassed directly prior to the measurement.

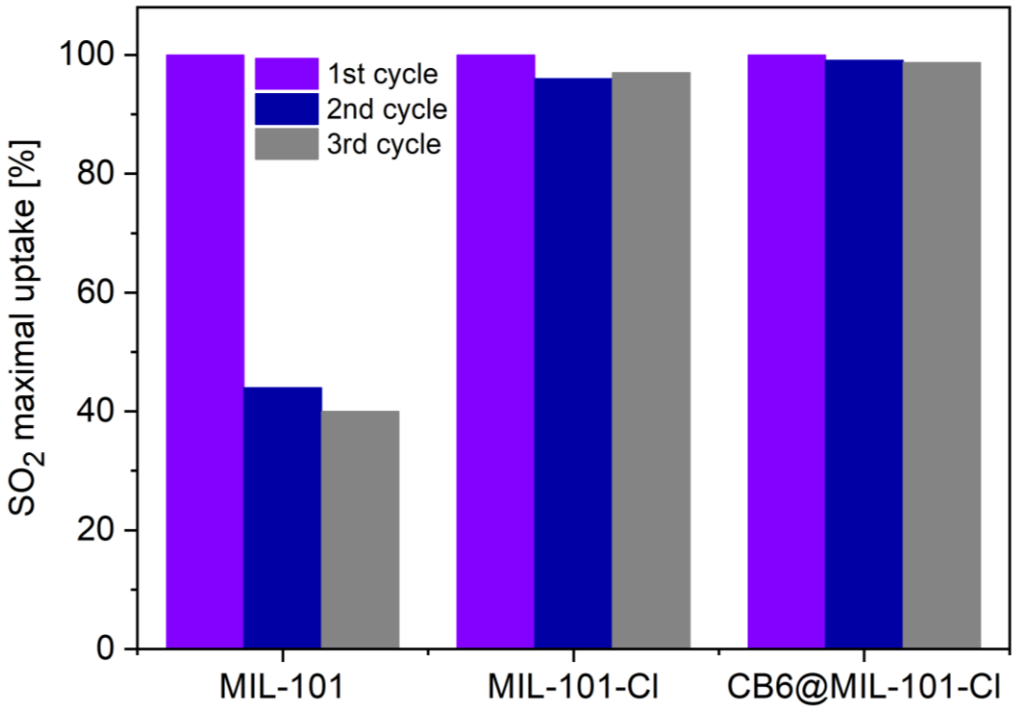


**Fig. S13** Cycling $SO_2$ adsorption-desorption performance of MIL-101[21], MIL-101-Cl and CB6@MIL-101-Cl at 293 K and 0.96 bar from three-cycle ad/desorption measurements, full isotherms (with 17 points for ads. and 12 points for des.). Between each individual isotherm sorption experiment the samples were activated at 150 °C under vacuum ($1\times10^{-3}$ mbar) for 12 hours. The first $SO_2$ uptake value was set to 100% as reference point with the second and third uptake value given relative to it.

**Table S7** Porosity characteristics of MIL-101, CB6@MIL-101-Cl, MIL-101-Cl and nanoCB6-H before and after exposure to cyclic $SO_2$ adsorption at 293 K, and after exposure to humid $SO_2$ for 6 h.

| | **before** | | **after cyclic $SO_2$ ads.** | | **after humid $SO_2$ exposure** | |
|---|---|---|---|---|---|---|
| | $S_{BET}$ [$m^2 \cdot g^{-1}$] | $V_{total}$ [$cm^3 \cdot g^{-1}$] | $S_{BET}$ [$m^2 \cdot g^{-1}$] | $V_{total}$ [$cm^3 \cdot g^{-1}$] | $S_{BET}$ [$m^2 \cdot g^{-1}$] | $V_{total}$ [$cm^3 \cdot g^{-1}$] |
| **MIL-101** | 3217 | 1.54 | 1768 | 0.84 | 3228 | 1.50 |
| **CB6@MIL-101-Cl** | 2077 | 1.00 | 2036 | 0.98 | 2104 | 1.03 |
| **MIL-101-Cl** | 3408 | 1.63 | 3541 | 1.66 | 3390 | 1.63 |
| **nanoCB6-H** | 435 | 0.24 | — | — | 79 | 0.06 |

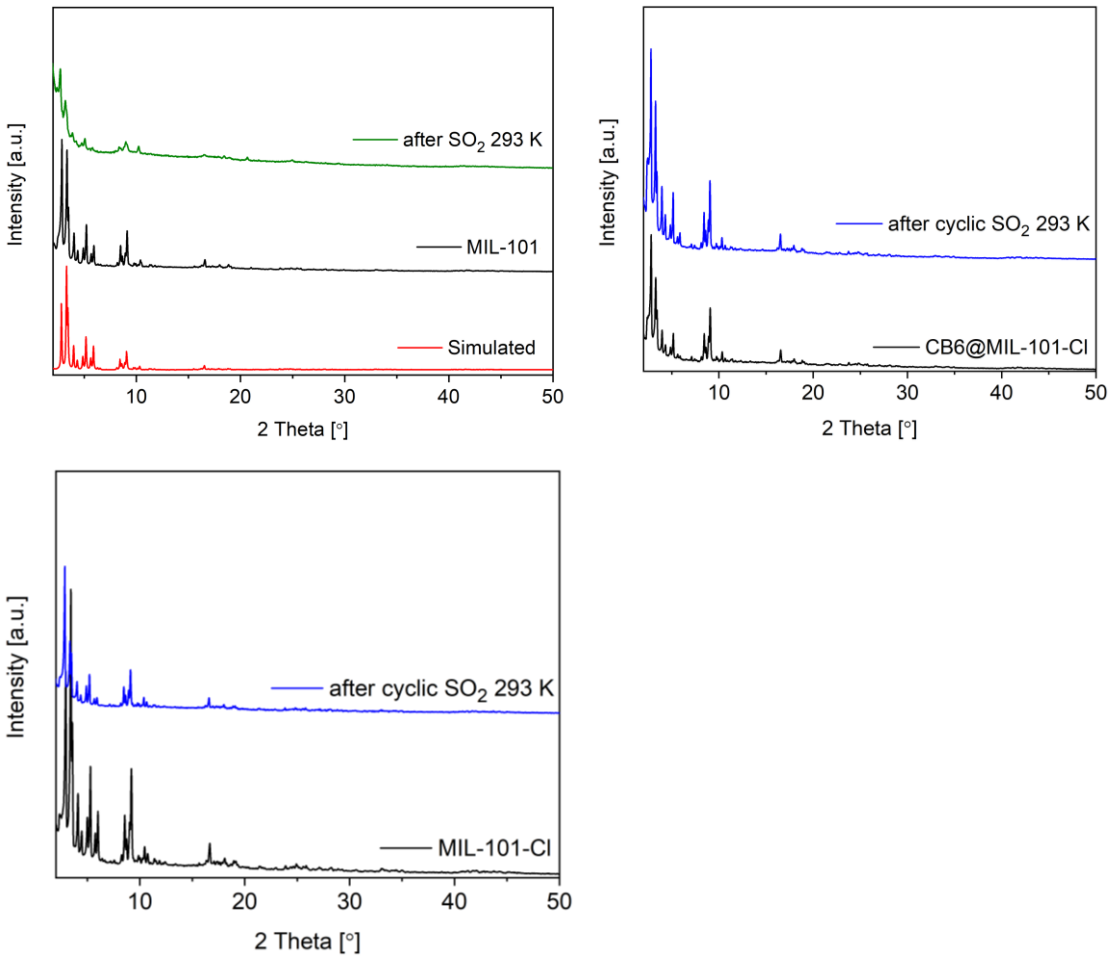


**Fig. S14** PXRD patterns of MIL-101, CB6@MIL-101-Cl and MIL-101-Cl after cyclic $SO_2$ adsorption (3 cycles for MIL-101 and MIL-101-Cl, 10 cycles for CB6@MIL-101-Cl. The samples between each individual sorption experiment were activated at 150 °C and $1\times10^{-3}$ mbar. After the last cycle each sample was degassed at 150 °C and $1 \times 10^{-3}$ mbar for 12 h.

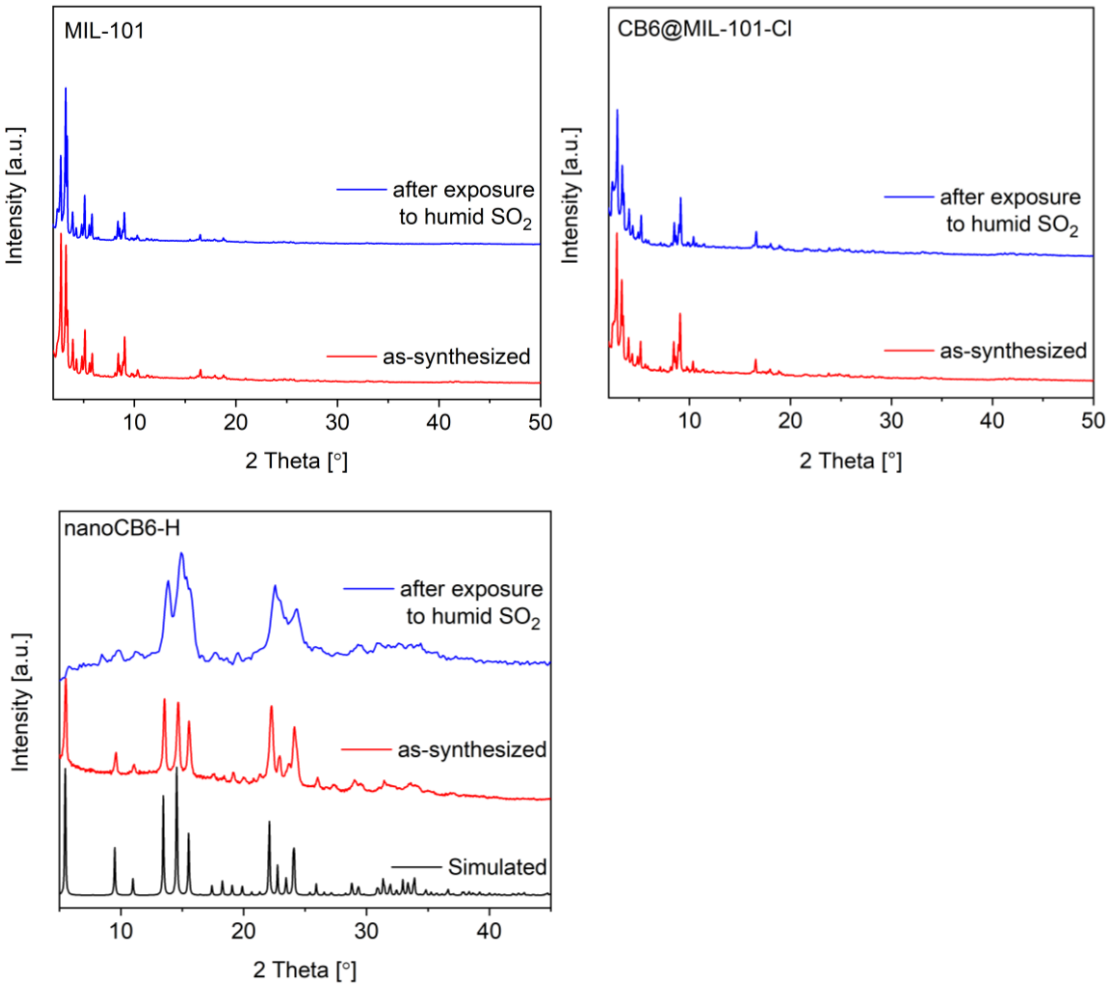


**Fig. S15** PXRD patterns of MIL-101, CB6@MIL-101-Cl and nanoCB6-H before and after exposure to humid $SO_2$ (35 ± 5 ppm) for 6h.

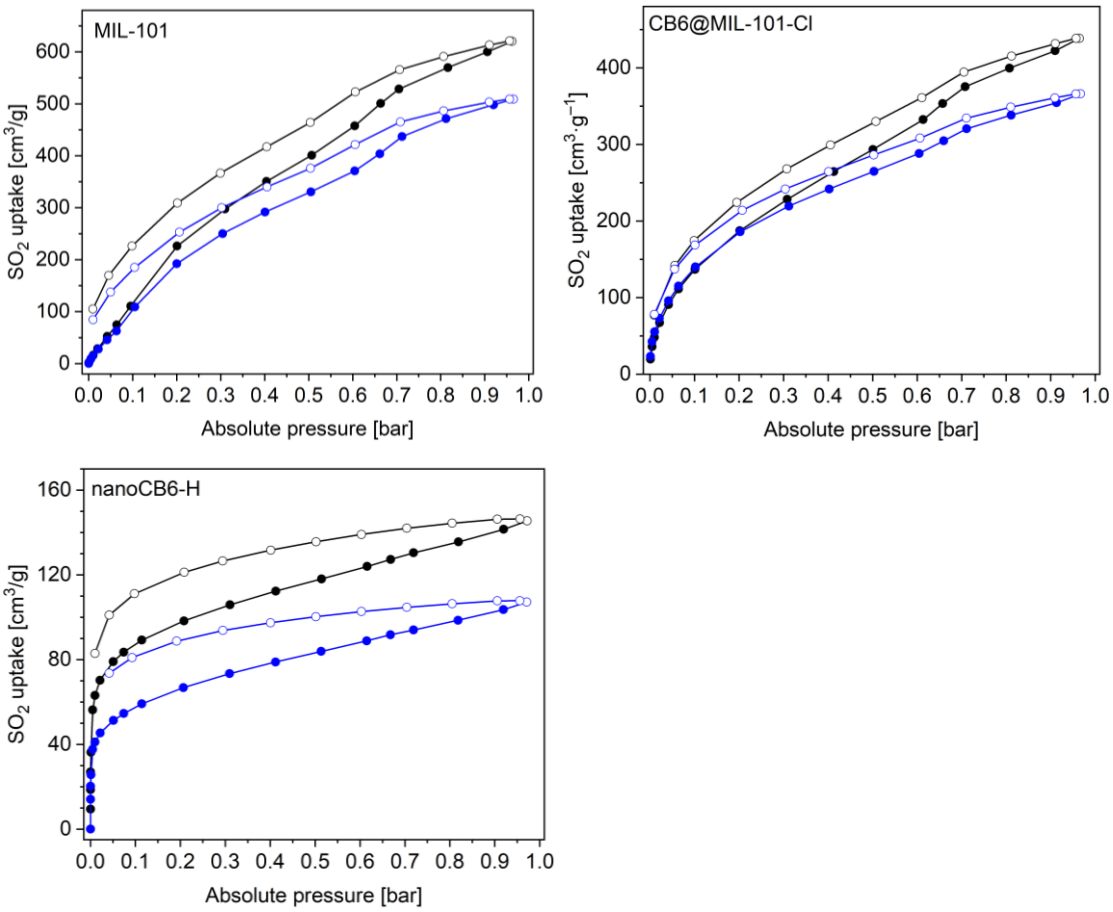


**Fig. S16** $SO_2$ adsorption isotherms at 293 K of MIL-101, CB6@MIL-101-Cl and nanoCB6-H before (black) and after (blue) exposure to humid $SO_2$ for 6 h.

**Table S8** $SO_2$ uptake at 293K of MIL-101, CB6@MIL-101-Cl and nanoCB6-H at 0.01 bar and 1 bar.

| | **dry conditions** | | **after exposure to humid $SO_2$** | |
|---|---|---|---|---|
| | $SO_2$ uptake at 293 K at [mmol·g$^{-1}$] | | $SO_2$ uptake at 293 K at [mmol·g$^{-1}$] | |
| | 0.01 bar | 1 bar | 0.01 bar | 1 bar |
| **MIL-101** | 0.7 | 27.7 | 0.7 | 22.7 |
| **CB6@MIL-101-Cl** | 2.1 | 19.5 | 2.4 | 16.3 |
| **nanoCB6-H** | 2.8 | 6.5 | 1.8 | 4.8 |

## References


1 J. Liang, A. Nuhnen, S. Millan, H. Breitzke, V. Gvilava, G. Buntkowsky and C. Janiak, *Angew. Chem. Int. Ed.*, 2020, **59**, 6068-6073.

2 G. Férey, C. Mellot-Draznieks, C. Serre, F. Millange, J. Dutour, S. Surblé and I. Margiolaki, *Science*, 2005, **309**, 2040.

3 S. Lim, H. Kim, N. Selvapalam, K.-J. Kim, S. J. Cho, G. Seo and K. Kim, *Angew. Chem. Int. Ed.,* 2008, **47**, 3352-3355.

4 3P INSTRUMENTS, 3P sim, Version 1.1.0.7, *Simulation and Evaluation Tool for mixSorb*, 3P INSTRUMENTS 2018.

5 X. Cui, Q. Yang, L. Yang, R. Krishna, Z. Zhang, Z. Bao, H. Wu, Q. Ren, W. Zhou, B. Chen and H. Xing, *Adv. Mater.*, 2017, **29**, 1606929.

6 P. Brandt, A. Nuhnen, M. Lange, J. Möllmer, O. Weingart and C. Janiak, *ACS Appl. Mater. Interfaces,* 2019, **11**, 17350-17358.

7 S. Xing, J. Liang, P. Brandt, F. Schäfer, A. Nuhnen, T. Heinen, I. Boldog, J. Möllmer, M. Lange, O. Weingart and C. Janiak, *Angew. Chem. Int. Ed*., 2021, **60**, 17998-18005.

8 L. Li, I. da Silva, D. I. Kolokolov, X. Han, J. Li, G. Smith, Y. Cheng, L. L. Daemen, C. G. Morris, H. G. W. Godfrey, N. M. Jacques, X. Zhang, P. Manuel, M. D. Frogley, C. A. Murray, A. J. Ramirez-Cuesta, G. Cinque, C. C. Tang, A. G. Stepanov, S. Yang and M. Schröder, *Chem. Sci.*, 2019, **10**, 1472-1482.

9 Z. Zhang, B. Yang and H. Ma, *Sep. Purif. Technol.*, 2021, **259**, 118164.

10 P. Brandt, S.-H. Xing, J. Liang, G. Kurt, A. Nuhnen, O. Weingart and C. Janiak, *ACS Appl. Mater. Interfaces*, 2021, **13**, 29137-29149.

11 P. Brandt, A. Nuhnen, S. Öztürk, G. Kurt, J. Liang and C. Janiak, *Adv. Sustain. Syst.*, 2021, **5**, 2000285.

12 M. Savage, Y. Cheng, T. L. Easun, J. E. Eyley, S. P. Argent, M. R. Warren, W. Lewis, C. Murray, C. C. Tang, M. D. Frogley, G. Cinque, J. Sun, S. Rudić, R. T.

Murden, M. J. Benham, A. N. Fitch, A. J. Blake, A. J. Ramirez-Cuesta, S. Yang and M. Schröder, *Adv. Mater.*, 2016, **28**, 8705-8711.

13 J. H. Carter, X. Han, F. Y. Moreau, I. da Silva, A. Nevin, H. G. W. Godfrey, C. C. Tang, S. Yang and M. Schröder, *J. Am. Chem. Soc.*, 2018, **140**, 15564-15567.

14 T. Grant Glover, G. W. Peterson, B. J. Schindler, D. Britt and O. Yaghi, *Chem. Eng. Sci.*, 2011, **66**, 163-170.

15 K. Tan, P. Canepa, Q. Gong, J. Liu, D. H. Johnson, A. Dyevoich, P. K. Thallapally, T. Thonhauser, J. Li and Y. J. Chabal, *Chem. Mater.*, 2013, **25**, 4653-4662.

16 E. Martínez-Ahumada, M. L. Díaz-Ramírez, H. A. Lara-García, D. R. Williams, V. Martis, V. Jancik, E. Lima and I. A. Ibarra, *J. Mater. Chem. A*, 2020, **8**, 11515-11520.

17 S. Glomb, D. Woschko, G. Makhloufi and C. Janiak, *ACS Appl. Mater. Interfaces,* 2017, **9**, 37419-37434.

18 G. L. Smith, J. E. Eyley, X. Han, X. Zhang, J. Li, N. M. Jacques, H. G. W. Godfrey, S. P. Argent, L. J. McCormick McPherson, S. J. Teat, Y. Cheng, M. D. Frogley, G. Cinque, S. J. Day, C. C. Tang, T. L. Easun, S. Rudić, A. J. Ramirez-Cuesta, S. Yang and M. Schröder, *Nat. Mater.,* 2019, **18**, 1358-1365.

19 S. Yang, L. Liu, J. Sun, K. M. Thomas, A. J. Davies, M. W. George, A. J. Blake, A. H. Hill, A. N. Fitch, C. C. Tang and M. Schröder, *J. Am. Chem. Soc.*, 2013, **135**, 4954-4957.

20 K. Tan, P. Canepa, Q. Gong, J. Liu, D. H. Johnson, A. Dyevoich, P. K. Thallapally, T. Thonhauser, J. Li and Y. J. Chabal, *Chem. Mater.*, 2013, **25**, 4653-4662.

21 Nuhnen and C. Janiak, *Dalton Trans.,* 2020, **49**, 10295-10307.

22 N. Tannert, Y. Sun, E. Hastürk, S. Nießing and C. Janiak, *Z. Anorg. Allg. Chem.*, 2021, **647**, 1124–1130.

# 4 Unpublished Part

The unpublished part includes three porphyrin-based MOFs, such as PCN-224 and Al-PMOF for heat transformation applications in section 4.1 and section 4.2, as well as PCN-222 in section 4.3. Chemicals and instrumentations are given in section 4.4 and the relevant experimental procedures are recorded in section 4.5.

## 4.1 Structure and vapor sorption of PCN-224

In PCN-224, $[Zr_6(\mu_3\text{-}O)_4(\mu_3\text{-}OH)_4(OH)_6(H_2O)_6(TCPP)_{1.5}$, TCPP = *meso*-tetrakis(4-carboxyphenyl)porphyrin)], each $Zr_6(OH)_8$ core is only connected to six carboxylates from TCPP ligands and the residual uncoordinated Zr sites are occupied by terminal OH (or $H_2O$) ligands. The structure of PCN-224 features 3-dimensional cubic channels with a diameter of 19 Å (Figure 11).[116]

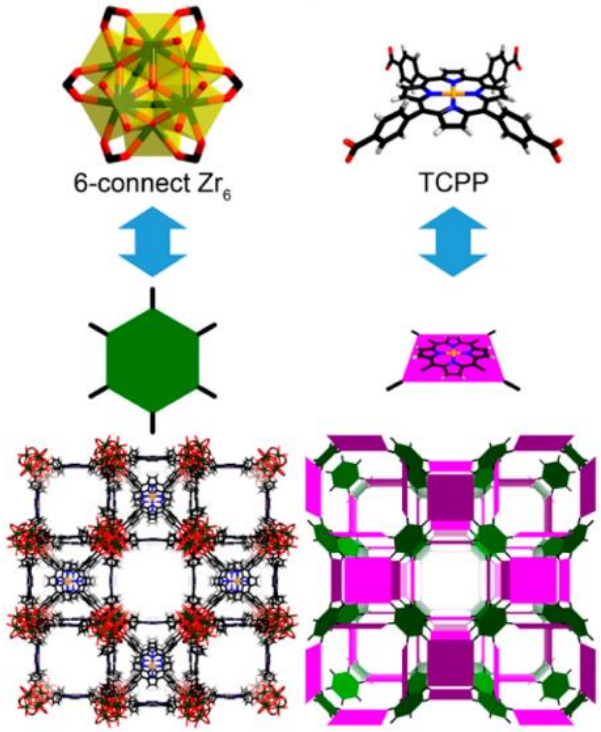


**Figure 11** Representation of PCN-224 with the 6-connected $D_{3d}$ symmetric $Zr_6$ and tetratopic TCPP ligand. Reproduced with permission from ref 116.Copyright 2013 American Chemical Society.

PCN-224 was synthesized via two different approaches, as described in the experimental part (section 4.5). Powder X-ray diffraction (PXRD) patterns of PCN-224 samples both well matched the simulated pattern, confirming the phase purity of the targeted materials (Figure 12). Compared to PCN-224_1, PCN-224_2 exhibits a higher crystallinity, which is in line with the following $N_2$ adsorption results.

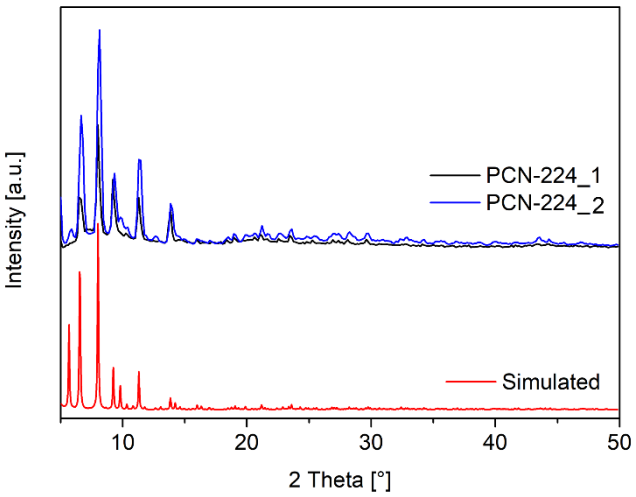


**Figure 12** PXRD patterns for simulated and experimental PCN-224 samples via two synthetic approaches (CCDC number: 919444).[116]

The porosity of the samples was evaluated by analysis of the $N_2$ adsorption-desorption isotherms measured at 77 K. The typical type Ib sorption isotherms of PCN-224 indicated their microporous nature. The Brunauer-Emmett-Teller (BET) surface area and total pore volume of PCN-224 from two synthetic approaches were found to be different. The isotherms of PCN-224_1 vs PCN-224_2 are shown in Figure 13. PCN-224_2 shows a higher crystallinity and porosity. However, it is still lower compared to the previous literature with a BET surface area of 2600 $m^2\ g^{-1}$.[116]

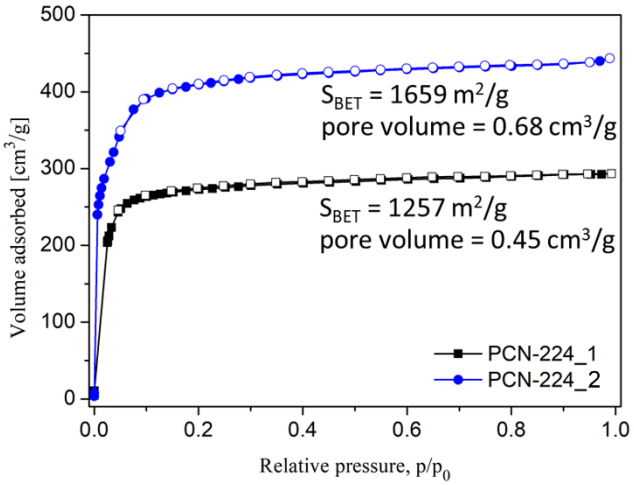


**Figure 13** $N_2$ adsorption-desorption isotherms at 77 K of PCN-224 samples via two synthetic approaches (Filled: adsorption, empty: desorption).

On account of the chemical stability of PCN-224 reported in the literature,[116] PCN-224 was used to study water vapor adsorption for adsorption heat transformation application (AHT). The water vapor adsorption isotherm of PCN-224 is shown in Figure 14 left. It shows a typical type V isotherm and the steep uptake occurred at 0.5 $p/p_0$, which indicates the high hydrophobic nature of PCN-224. The maximal water vapor uptake is 321 mg $g^{-1}$. However, the steep water vapor adsorption that occurs at high relative pressure is unfavorable for AHT applications.

In contrast to water vapor, PCN-224 exhibits a good affinity towards ethanol at a low relative pressure (Figure 14 right). The samples of PCN-224 via two synthetic approaches have similar adsorption curve types and the steep uptake for both samples takes place between 0.05-0.2 $p \cdot p_0^{-1}$. The uptakes at 0.2 $p \cdot p_0^{-1}$ are up to 373 mg $g^{-1}$ and 712 mg $g^{-1}$, which are 84% and 85% of the maximal uptake capacity, respectively (444 mg $g^{-1}$ for PCN-224_1 vs 839 mg $g^{-1}$ for PCN-224_2). Understandably, due to the high crystallinity and porosity in PCN-224_2, it shows a high ethanol adsorption uptake. The structural characterization, such as PXRD and $N_2$ sorption after ethanol vapor adsorption need to be further investigated.

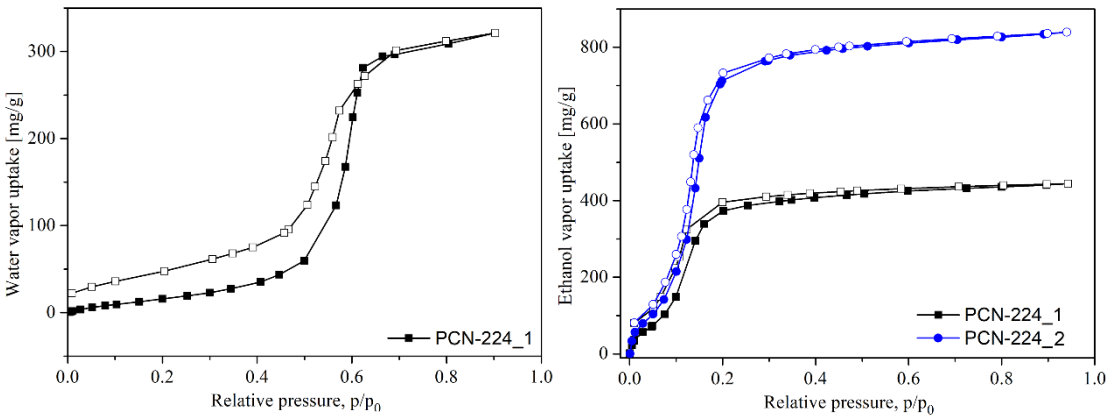


**Figure 14** Vapor sorption isotherm of PCN-224 with water (left) and ethanol (right) at 293 K

## 4.2 Structure and vapor sorption of Al-PMOF

Al-PMOF, $[Al_2(OH)_2TCPP]$, reported by Rosseinsky *et al.* in 2012, was found to be a water-stable material for optical applications.[117] In Al-PMOF, each porphyrin linker is coordinated to eight aluminum atoms via four carboxylates, and each aluminum (III) is connected to four carboxylates through oxygen atoms and is bridged by adjacent two $Al^{3+}$ centers via two $\mu_2$ axial $OH^-$, forming an infinite $Al(OH)O_4$ chain. The crystal structure is shown in Figure 15.

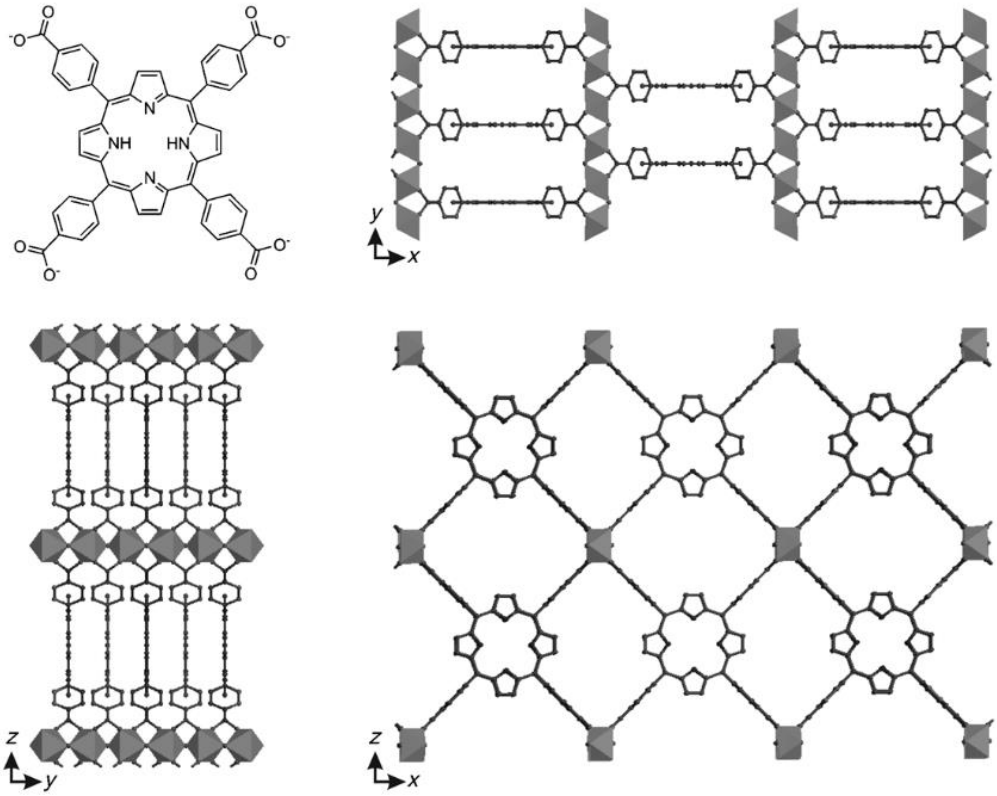


**Figure 15** TCPP porphyrinic linker and the crystal structure of Al-PMOF viewed from different directions. Reproduced with permission from ref 117.Copyright 2012 John Wiley and Sons.

PXRD pattern of synthesized Al-PMOF matches well with the simulated, which confirms the phase purity of Al-PMOF (Figure 16). An $N_2$ adsorption-desorption isotherm of Al-PMOF at 77 K (Figure 17) demonstrated a BET surface area of 966 $m^2g^{-1}$ with a pore volume of 0.41 $cm^3g^{-1}$ (at 0.80 $p\ p_0^{-1}$). The porosity of Al-PMOF before and after water vapor adsorption at 293 K remained almost unchanged (Figure 17).

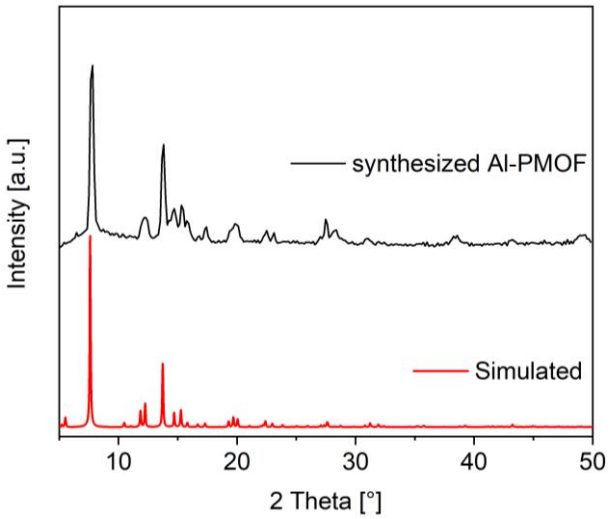


**Figure 16** Powder XRD patterns for simulated and experimental Al-PMOF sample (CCDC number:1500441)[117]

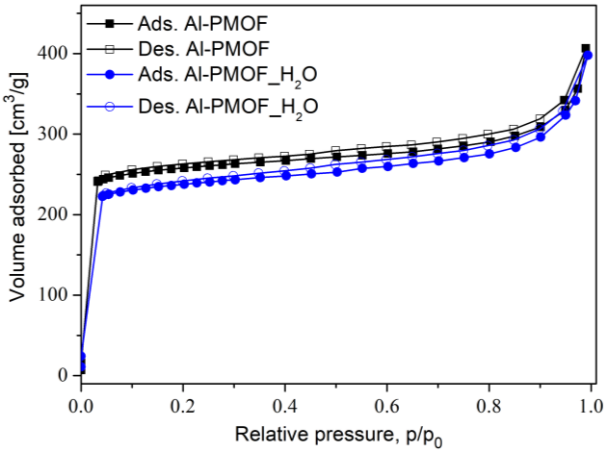


**Figure 17** $N_2$ adsorption-desorption isotherms at 77 K of Al-PMOF before (black) and after (blue) water vapor sorption (Filled: adsorption, empty: desorption).

Al-PMOF was synthesized under hydrothermal conditions and was therefore considered to be water stable. The water vapor adsorption and the ethanol vapor adsorption of Al-PMOF were measured, respectively (Figure 18). The results were similar to PCN-224 and showed that Al-PMOF exhibited quite hydrophobic nature with a steep water vapor uptake at around 0.5 $p\ p_0^{-1}$. The relative pressure of water vapor adsorption-desorption of Al-PMOF is not in the range which is favorable for AHT application (0.05-0.3 $p\ p_0^{-1}$). In addition, the behavior of Al-PMOF on ethanol vapor is different from that of water vapor. Al-PMOF showed a very strong affinity towards

ethanol vapor and steep vapor uptake at low pressure. The maximal water vapor and ethanol vapor uptake of Al-PMOF were 280 mg $g^{-1}$ and 305 mg $g^{-1}$, respectively.

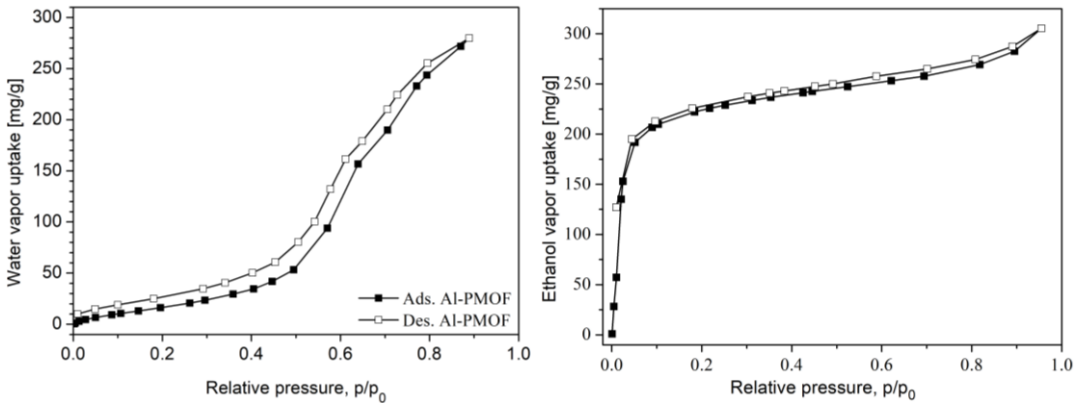


**Figure 18** Vapor sorption isotherm of Al-PMOF with water (left) and ethanol (right) at 293 K.

## 4.3 Structure and properties of PCN-222

PCN-222/MOF-545, $[Zr_6(\mu_3\text{-}O)_4(\mu_3\text{-}OH)_4(OH)_4(H_2O)_4(TCPP)_2]$, is a highly stable mesoporous porphyrinic zirconium MOF. It possesses large hexagonal 1D open channels, with a diameter of up to 3.7 nm along the c axis (Figure 19).[118] The framework of PCN-222 composes of $Zr_6$ clusters connected by the square planar TCPP ligands. Each $Zr_6(OH)_8$ core is connected to eight TCPP ligands and the $Zr_6$-octahedra in the triangular faces are capped by eight $\mu_3$-OH ligands.

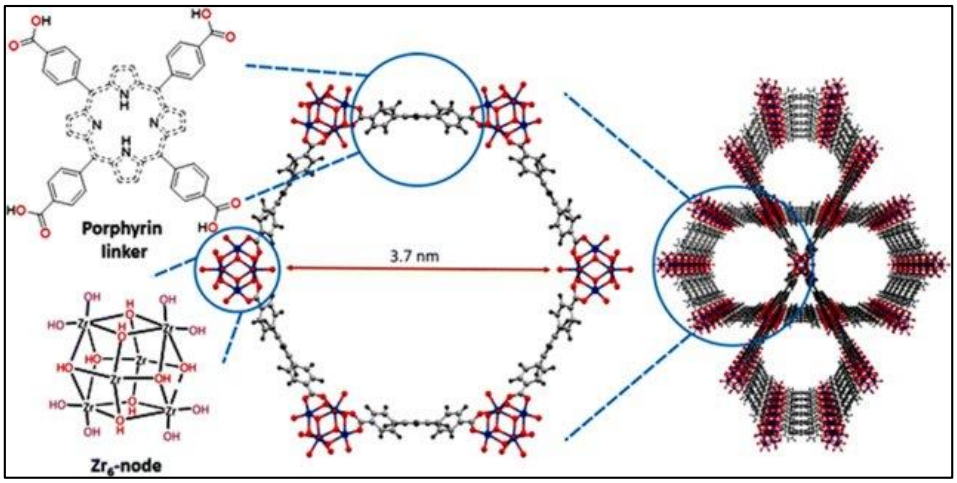


**Figure 19** Molecular representation of PCN-222 (Reproduced with the permission from ref 118. Copyright 2017 Springer New York)

PXRD pattern of PCN-222 is in line with the simulated pattern, demonstrating the successful synthesis of the pure-phase PCN-222 (Figure 20).

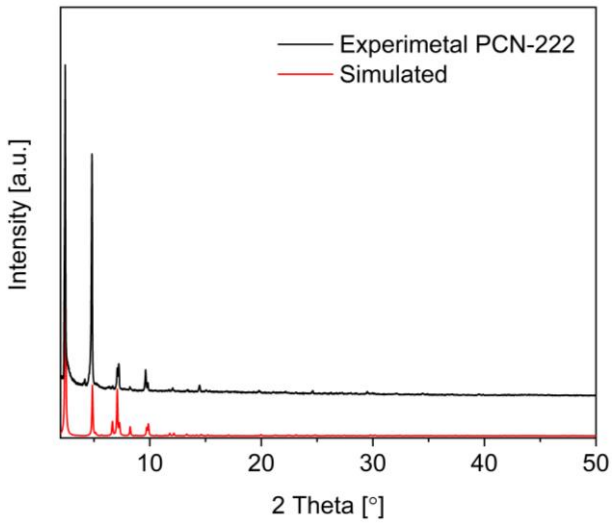


**Figure 20** PXRD patterns of experimental and simulated PCN-222 (CCDC number: 893545)[119].

The porosity of PCN-222 was examined by $N_2$ adsorption-desorption experiments at 77 K. PCN-222 affords a high $N_2$ uptake of up to 587 $cm^3\ g^{-1}$ at 77 K and 1 bar. The adsorption isotherm shows a steep increase at 0.3 $p\ p_0^{-1}$ and presents a typical type IV isotherm, indicative of the mesoporous framework of PCN-222. A high BET specific surface area of up to 1348 $m^2 \cdot g^{-1}$ with a total pore volume of 0.89 $cm^3\ g^{-1}$ (at 0.9 $p\ p_0^{-1}$) was calculated (Figure 21 left). The BET surface area and porosity of PCN-222 are lower, compared to the previous literature with a BET surface area of 2200 $m^2\ g^{-1}$, as well as the total pore volume of 1.56 $cm^3\ g^{-1}$.[116] The pore size distribution (PSD) of PCN-222 (Figure 21 right) shows pores with diameters of 12.3, 15.6 and 36.0 Å, assigned to triangular microchannels (12.3 and 15.6 Å) and hexagonal mesochannels (36.0 Å), which well corresponds the hexagonal diameter (37 Å) of the framework (Figure 19).

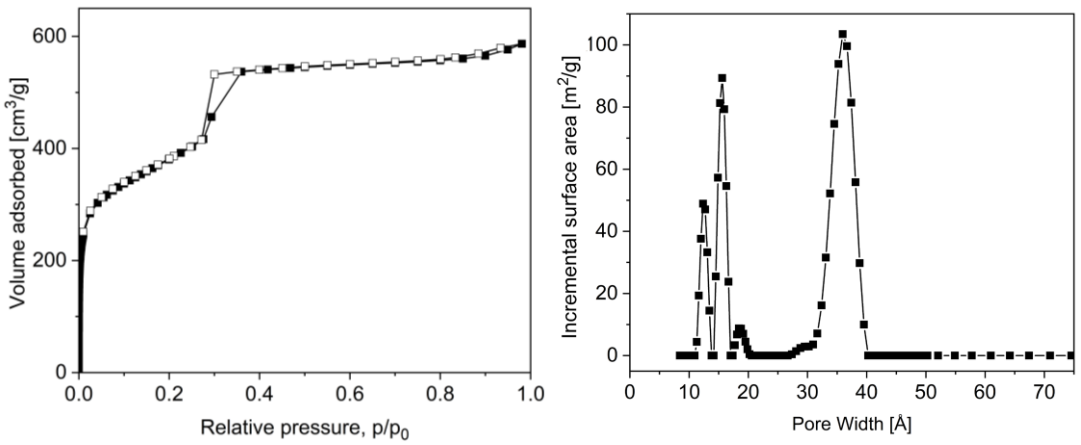


**Figure 21** $N_2$ sorption isotherm (left) and pore size distribution (right) for PCN-222 at 77 K.

Considering the high BET surface area and good chemical stability, PCN-222 could have the possibility of encapsulation of porous organic cage (POC). This part of the work was in cooperation with Dr. Jun Liang. The organic fluorinated [4+4] imine cage [120] was incorporated into PCN-222 by wet impregnation. Unfortunately, this experiment was not as expected, and the unsuccessful experiment may be due to the particularly poor solubility of fluorinated organic [4+4] imine cage, or the insufficient interactions between this kind of POC and the framework of PCN-222.

## 4.4 Chemicals and Instrumentation.

The chemicals used for this chapter are listed in Table 4.

Table 4 Starting materials and solvents are obtained from commercial sources.

| Item | Manufacturer |
|---|---|
| Zirconium(IV) chloride ($ZrCl_4$) | Alfa Aesar |
| *N,N*-dimethylformamide (DMF) | Fisher Chemicals |
| Propionic acid | Sigma–Aldrich/Merck |
| Methyl *p*-formylbenzoate | Alfa Aesar |
| Pyrrole | Sigma–Aldrich |
| Ethanol | Sigma–Aldrich |
| Ethyl acetate | Sigma–Aldrich |
| deuterated Chloroform ($CDCl_3$) | Sigma–Aldrich/Merck |
| Tetrahydrofuran | Sigma–Aldrich |

| | |
|---|---|
| Methanol | Sigma–Aldrich |
| Potassium hydroxide | Acros Organic |
| Hydrochloric acid | Fisher Chemicals |
| deuterated Dimethyl sulfoxide (DMSO-d) | Sigma–Aldrich/Merck |
| Benzoic acid | Acros Organic |
| Zirconyl chloride octahydrate ($ZrOCl_2$ $8H_2O$) | Acros Organic |
| Acetic acid | Fisher Chemicals |
| Aluminum chloride hexahydrate $AlCl_3 \cdot 6H_2O$ | Acros Organic |
| *N,N*-diethylformamide (DEF) | Fisher Chemicals |
| Acetone | Fisher Chemicals |

Powder X-ray diffractometry (PXRD) was performed at room temperature on a Bruker D2 Phaser (300 W, 30kV, 10mA) using Cu-Kα radiation (λ = 1.54182 Å) in the range of $5° < 2\theta < 50°$ with a scanning rate of $0.15° \ s^{-1}$ (300 W, 30 kV, 10 mA). The analyses of the diffractograms were carried out with the "Match! 3.5.3.109" software.

The adsorption–desorption isotherms of nitrogen were measured at 77 K using a Micrometrics ASAP 2020 for PCN-222 or an Autosorb-6 from Quantachrome for PCN-224 and Al-PMOF. For activation, the sample was degassed in a vacuum of $5 \times 10^{-2}$ mbar at 150 °C for 12 h. The Brunauer−Emmett−Teller (BET) surface areas were calculated in the $p/p_0$ range of 0.01−0.05. Total pore volumes were calculated from nitrogen adsorption isotherms at $p/p_0 = 0.90$. The pore size distribution which was calculated using NLDFT method at 77 K for "N2 on cylindrical pores".

1H NMR spectra were recorded on a Bruker Avance III-300. 5~10 mg of the dried sample was dissolved with 600 μL of the deuterated solvent ($CDCl_3$ or DMSO-d), followed by ultrasonication for half an hour to ensure digestion.

Volumetric water vapor sorption isotherms were measured on a Quantachrome VSTAR vapor sorption analyzer at 293 K. Before the measurements, the samples were placed in cap-sealed glass tubes for initial weighing. The tubes including the samples were degassed under vacuum for at least 3 hours at 150-170 ° C and weighed again.

## 4.5 Experimental part

### 4.5.1 Synthesis of tetrakis(4-carboxyphenyl)porphyrin ($H_4TCPP$)

Typically, the synthetic procedures were carried out by two steps according to the previous work:[116] Firstly, the ester form of TCPP was prepared from mixing propionic acid (200 ml), methyl *p*-formylbenzoate (13.8 g, 0.084 mol) and pyrrole (6.2 mL, $\rho$ = 0.96 $g \cdot cm^{-3}$) in a three-necked flask (250 mL). The solution was refluxed for 12 h at 140 °C and cooled down to room temperature. The product was then self-crystallized due to its insolubility in propionic acid. Afterward, the mixture was put in the refrigerator for 5 hours to precipitate crystals. At last, the precipitate was filtered through a No.4 sand core funnel and was washed slowly with ethanol (80 mL) to remove unreacted propionic acid, then with ethyl acetate to remove polypyrrole (by-product). Final washing was carried out with a few drops of THF. The product, a purple crystal, was put in a vacuum for drying. $^1$H-NMR (Figure 22): (300 MHz, $CDCl_3$) $\delta$ 8.82 (s, 8H), 8.44 (d, 8H), 8.30 (d, 8H), 4.11 (s, 12H), 2.81 (s, 2H).

Secondly, the acid form of TCPP was continually prepared. The 1.95 g of ester above was weighed in a flask and stirred in a mixed solvent of THF (60 mL) and MeOH (60 mL), followed by the addition of a KOH solution (6.82 g, 60 mL). This mixture was refluxed for 12 h and cooled down to room temperature. Afterward, THF and MeOH were evaporated by rotary evaporation at 335 mbar and 40 °C. Later, the condition was adjusted to 50 °C with a pressure of 150 mbar. The amount of liquid evaporated should be equal to the total amount of the mixed solution of THF and MeOH. After that, a large amount of water (800 mL) was added to completely dissolve the solid. The

solution was acidified with 1M HCl until a purple solid precipitated (use a disposable chemical dropper to suck up a small amount of the solution, and drop it on the tissue paper to see if the purple solid is precipitated). The sample was kept still overnight. Then the upper salt solution was slowly sucked out by a chemical dropper and the remaining small amount of the mixture is centrifuged, then washed with water and dried in a vacuum at 120 °C. $^{1}$H NMR (Figure 23): (300 MHz, DMSO-d) δ 2 8.86 (s 8H), 8.39 (d 16H) -2.93 (s, 2H);

### 4.5.2 Synthesis of PCN-224

Approach 1: Zirconium chloride (30 mg, 0.13 mmol) was added to *N,N*-dimethylformamide (DMF, 2 mL), followed by the addition of 400 mg benzoic acid, and tetrakis(4-carboxyphenyl) porphyrin (TCPP, 10 mg, 0.013 mmol). The mixture was transferred into an autoclave and heated at 120 °C for 24 h (PCN-224_1 sample).

Approach 2: Zirconyl chloride octahydrate (1.25 g, 3.88 mmol) was added to DMF (150 mL) and sonicated for 15 minutes, then TCPP (250 mg, 0.32 mmol) was added to the solution. After half an hour, acetic acid (25 mL) was added. The mixture was transferred into autoclaves (100 mL) and heated at 80 °C for three days (1 h for heating up to the target temperature and 2h cooling down to room temperature). The microcrystalline powder was filtered and washed with DMF (5 × 25 mL) over a three-hour period. The DMF was then replaced with acetone (5 × 25 mL) over a five-day period. Finally, the sample was dried at 120 °C under vacuum (0.05 – 0.01 mbar) overnight (PCN-224_2 sample).

### 4.5.3 Synthesis of Al-PMOF

According to the previous report,[117] 5,10,15,20-tetrakis(4-carboxyphenyl) porphyrin (100 mg, 0.126 mmol) and $AlCl_3 \cdot 6H_2O$ (60 mg, 0.25 mmol) were introduced into 10 mL of deionized water. The suspension was stirred for 10 minutes at room temperature and then transferred into a 40 mL Teflon-lined autoclave and heated at 180 °C for 16

hours (1.5 h for heating up to the target temperature, 3 h for cooling down to room temperature). The solid was centrifuged and washed with DMF (3 × 80 mL) to remove the unreacted porphyrin and acetone (3 × 80 mL). After drying, the Al-PMOF was obtained as a red solid (yield: 50 mg, 25%).

### 4.5.4 Synthesis of PCN-222

The synthetic procedure was carried out as follows with some modifications:[119] Benzoic acid (2.7 g, 22 mmol·g$^{-1}$) was firstly dissolved in *N,N*-diethylformamide (DEF), and $ZrCl_4$ (75 mg, 0.322 mmol g$^{-1}$) was added under stirring. After the mixture was dissolved, TCPP (50 mg, 0.063 mmol) was introduced. The mixture was transferred to an autoclave, which was heated in a temperature-programmed oven (80 minutes heating up to 120 °C, kept for 48 h, followed by 10 minutes heating up to 130 °C and kept for 24 h, then 24h for cooling down to room temperature). After the reaction, the precipitate was washed by filtration with DMF and acetone to remove the residual benzoic acid. Afterward, DMF (70 mL) and conc. HCl (12 mol L$^{-1}$, 0.35 mL) and the precipitate were added in a 250 mL flask, and the mixture was green. After ultrasonication for 20 min, the mixture was refluxed at 120 °C for 17 h, and then cooled down to room temperature. The mixture turned orange, and the precipitate was filtered. The precipitate was soaked in DMF for 2 days (4 × 80 mL), followed by washing and immersing with acetone for 3 days (6 × 80 mL). At last, the purple, needle-shaped crystal was centrifuged and dried in a vacuum (yield: 37 mg, 48%).

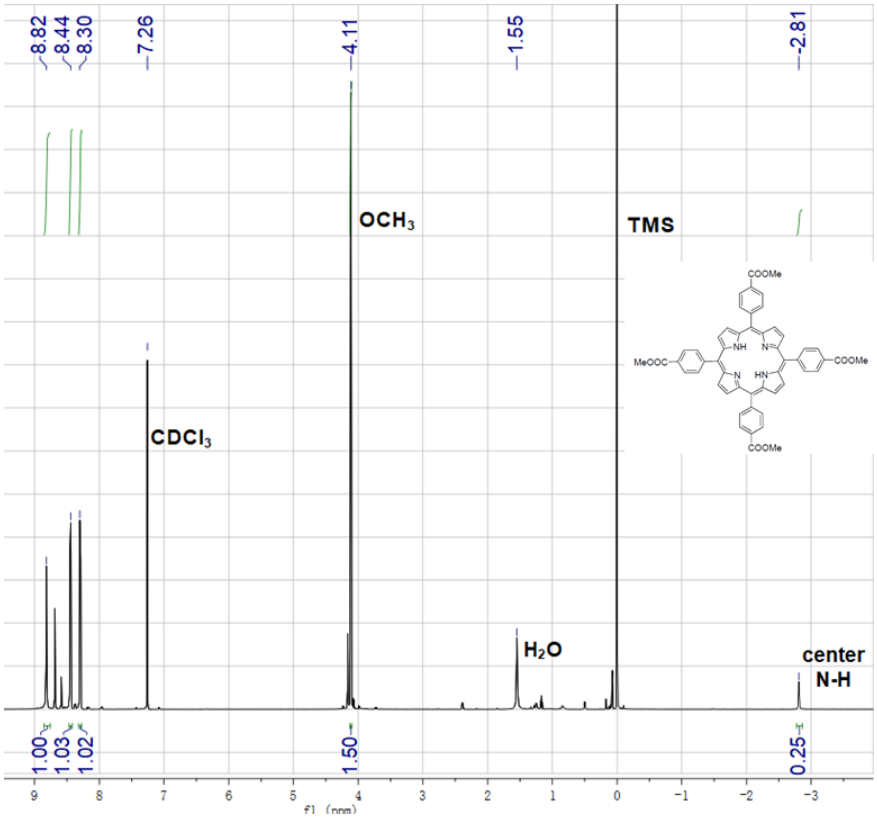


Figure 22 $^{1}$H-NMR of the ester form of TCPP.

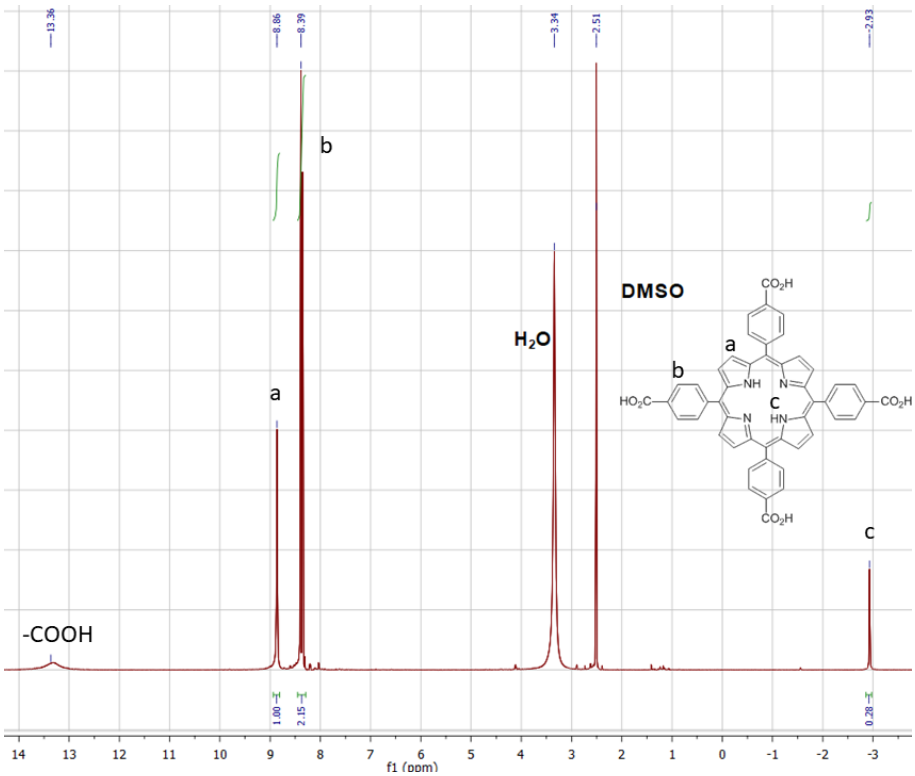


Figure 23 $^{1}$H-NMR of the acid form of TCPP.

# 5 References


1 S. Furukawa, J. Reboul, S. Diring, K. Sumida and S. Kitagawa, *Chem. Soc. Rev.*, 2014, **43**, 5700-5734.

2 M. P. Suh, H. J. Park, T. K. Prasad and D.-W. Lim, *Chem. Rev.*, 2012, **112**, 782-835.

3 Y. He, W. Zhou, G. Qian and B. Chen, *Chem. Soc. Rev.*, 2014, **43**, 5657-5678.

4 J.-R. Li, J. Sculley and H.-C. Zhou, *Chem. Rev.*, 2012, **112**, 869-932.

5 J.-R. Li, R. J. Kuppler and H.-C. Zhou, *Chem. Soc. Rev.*, 2009, **38**, 1477-1504.

6 F. Vermoortele, B. Bueken, G. Le Bars, B. Van de Voorde, M. Vandichel, K. Houthoofd, A. Vimont, M. Daturi, M. Waroquier, V. Van Speybroeck, C. Kirschhock and D. E. De Vos, *J. Am. Chem. Soc.*, 2013, **135**, 11465-11468.

7 W. P. Lustig, S. Mukherjee, N. D. Rudd, A. V. Desai, J. Li and S. K. Ghosh, *Chem. Soc. Rev.*, 2017, **46**, 3242-3285.

8 G. K. H. Shimizu, J. M. Taylor and S. Kim, *Science*, 2013, **341**, 354-355.

9 M. D. Allendorf, C. A. Bauer, R. K. Bhakta and R. J. T. Houk, *Chem. Soc. Rev.*, 2009, **38**, 1330-1352.

10 P.-L. Wang, L.-H. Xie, E. A. Joseph, J.-R. Li, X.-O. Su and H.-C. Zhou, *Chem. Rev.*, 2019, **119**, 10638-10690.

11 H. Li, M. Eddaoudi, M. O'Keeffe and O. M. Yaghi, *Nature*, 1999, **402**, 276-279.

12 S. S. Y. Chui, S. M. F. Lo, J. P. H. Charmant, A. G. Orpen and I. D. Williams, *Science*, 1999, **283**, 1148.

13 G. Férey, C. Mellot-Draznieks, C. Serre, F. Millange, J. Dutour, S. Surblé and I. Margiolaki, *Science*, 2005, **309**, 2040.

14 J. H. Cavka, S. Jakobsen, U. Olsbye, N. Guillou, C. Lamberti, S. Bordiga and K. P. Lillerud, *J. Am. Chem. Soc.*, 2008, **130**, 13850-13851.

15 J. A. Greathouse and M. D. Allendorf, *J. Am. Chem. Soc.*, 2006, **128**, 13312-13312.

16 M. Eddaoudi, J. Kim, N. Rosi, D. Vodak, J. Wachter, M. Keeffe and O. M. Yaghi, *Science*, 2002, **295**, 469.

17 J. Liu, J. T. Culp, S. Natesakhawat, B. C. Bockrath, B. Zande, S. G. Sankar, G. Garberoglio and J. K. Johnson, *J. Phys. Chem. C*, 2007, **111**, 9305-9313.

18 P. Krawiec, M. Kramer, M. Sabo, R. Kunschke, H. Fröde and S. Kaskel, *Adv. Eng. Mater.*, 2006, **8**, 293-296.

19 C. Prestipino, L. Regli, J. G. Vitillo, F. Bonino, A. Damin, C. Lamberti, A. Zecchina, P. L. Solari, K. O. Kongshaug and S. Bordiga, *Chem. Mater., 2006*, **18**, 1337-1346.

20 J. R. Álvarez, E. Sánchez-González, E. Pérez, E. Schneider-Revueltas, A. Martínez, A. Tejeda-Cruz, A. Islas-Jácome, E. González-Zamora and I. A. Ibarra, *Dalton Trans.*, 2017, **46**, 9192-9200.

21 P. Küsgens, M. Rose, I. Senkovska, H. Fröde, A. Henschel, S. Siegle and S. Kaskel, *Micropor. Mesopor. Mat.*, 2009, **120**, 325-330.

22 P. M. Schoenecker, C. G. Carson, H. Jasuja, C. J. J. Flemming and K. S. Walton, *Ind. Eng. Chem. Res.*, 2012, **51**, 6513-6519.

23 N. Al-Janabi, P. Hill, L. Torrente-Murciano, A. Garforth, P. Gorgojo, F. Siperstein and X. Fan, *Chem. Eng. J.*, 2015, **281**, 669-677.

24 C. Janiak and J. K. Vieth, *New J. Chem.*, 2010, **34**, 2366-2388.

25 S. S. Y. Chui, S. M. F. Lo, J. P. H. Charmant, A. G. Orpen and I. D. Williams, *Science*, 1999, **283**, 1148.

26 M. Hartmann, S. Kunz, D. Himsl, O. Tangermann, S. Ernst and A. Wagener, *Langmuir*, 2008, **24**, 8634-8642.

27 J. B. DeCoste, G. W. Peterson, B. J. Schindler, K. L. Killops, M. A. Browe and J. J. Mahle, *J. Mater. Chem. A*, 2013, **1**, 11922-11932.

28 F. Gul-E-Noor, B. Jee, A. Pöppl, M. Hartmann, D. Himsl and M. Bertmer, *Phys. Chem. Chem. Phys.*, 2011, **13**, 7783-7788.

29 O. M. Yaghi, M. J. Kalmutzki and C. S. Diercks, Binary Metal-Organic Frameworks, Wiley-VCH, Weinheim, 2019.

30 Q. Yang, A. D. Wiersum, P. L. Llewellyn, V. Guillerm, C. Serre and G. Maurin, *Chem. Commun.*, 2011, **47**, 9603-9605.

31 C. Serre, F. Millange, C. Thouvenot, M. Noguès, G. Marsolier, D. Louër and G. Férey, *J. Am. Chem. Soc.*, 2002, **124**, 13519-13526.

32 F. Millange, N. Guillou, R. I. Walton, J.-M. Grenèche, I. Margiolaki and G. Férey, *Chem. Commun.*, 2008, **39**, 4732-4734.

33 C. Serre, F. Millange, S. Surblé and G. Férey, *Angew. Chem. Int. Ed.*, 2004, **43**, 6285-6289.

34 M. Dan-Hardi, C. Serre, T. Frot, L. Rozes, G. Maurin, C. Sanchez and G. Férey, *J. Am. Chem. Soc.*, 2009, **131**, 10857-10859.

35 T. Loiseau, C. Serre, C. Huguenard, G. Fink, F. Taulelle, M. Henry, T. Bataille and G. Férey, *Chem. Eur. J.*, 2004, **10**, 1373-1382.

36 D.-Y. Hong, Y. K. Hwang, C. Serre, G. Férey and J.-S. Chang, *Adv. Funct. Mater.*, 2009, **19**, 1537-1552.

37 N. Stock and S. Biswas, *Chem. Rev.*, 2012, **112**, 933-969.

38 M. Schlesinger, S. Schulze, M. Hietschold and M. Mehring, *Micropor. Mesopor. Mat.*, 2010, **132**, 121-127.

39 J. Klinowski, F. A. Almeida Paz, P. Silva and J. Rocha, *Dalton Trans.*, 2011, **40**, 321-330.

40 A. L. Garay, A. Pichon and S. L. James, *Chem. Soc. Rev.*, 2007, **36**, 846-855.

41 T. Friščić, *J. Mater. Chem.*, 2010, **20**, 7599-7605.

42 M. Eddaoudi, D. F. Sava, J. F. Eubank, K. Adil and V. Guillerm, *Chem. Soc. Rev.*, 2015, **44**, 228-249.

43 H. Furukawa, K. E. Cordova, M. O'Keeffe and O. M. Yaghi, *Science*, 2013, **341**, 1230444.

44 H. Furukawa, N. Ko, Y. B. Go, N. Aratani, S. B. Choi, E. Choi, A. Ö. Yazaydin, R. Q. Snurr, M. O'Keeffe, J. Kim and O. M. Yaghi, *Science*, 2010, **329**, 424.

45 D. Mustafa, E. Breynaert, S. R. Bajpe, J. A. Martens and C. E. A. Kirschhock, *Chem. Commun.*, 2011, **47**, 8037-8039.

46 J. J. Low, A. I. Benin, P. Jakubczak, J. F. Abrahamian, S. A. Faheem and R. R. Willis, *J. Am. Chem. Soc.*, 2009, **131**, 15834-15842.

47 V. Colombo, S. Galli, H. J. Choi, G. D. Han, A. Maspero, G. Palmisano, N. Masciocchi and J. R. Long, *Chem. Sci.*, 2011, **2**, 1311-1319.

48 H. Jasuja, N. C. Burtch, Y.-g. Huang, Y. Cai and K. S. Walton, *Langmuir*, 2013, **29**, 633-642.

49 N. u. Qadir, S. A. M. Said and H. M. Bahaidarah, *Micropor. Mesopor. Mat.*, 2015, **201**, 61-90.

50 N. C. Burtch, H. Jasuja and K. S. Walton, *Chem. Rev.*, 2014, **114**, 10575-10612.

51 S. Yuan, J. S. Qin, C. T. Lollar and H. C. Zhou, *ACS Cent. Sci.*, 2018, **4**, 440-450.

52 N. L. Rosi, J. Kim, M. Eddaoudi, B. Chen, M. O'Keeffe and O. M. Yaghi, *J. Am. Chem. Soc.*, 2005, **127**, 1504-1518.

53 J. B. DeCoste, G. W. Peterson, B. J. Schindler, K. L. Killops, M. A. Browe and J. J. Mahle, *J. Mater. Chem. A*, 2013, **1**, 11922-11932.

54 D. N. Dybtsev, H. Chun and K. Kim, *Angew. Chem. Int. Ed.*, 2004, **43**, 5033-5036.

55 O. M. Yaghi, M. J. Kalmutzki and C. S. Diercks, Functionalization of MOFs, Wiley-VCH, Weinheim, 2019.

56 J.-W. Sun, P.-F. Yan, G.-H. An, J.-Q. Sha, G.-M. Li and G.-Y. Yang, *Sci. Rep.*, 2016, **6**, 25595.

57 L. Bromberg, Y. Diao, H. Wu, S. A. Speakman and T. A. Hatton, *Chem. Mater.*, 2012, **24**, 1664-1675.

58 Y. Fu, D. Sun, Y. Chen, R. Huang, Z. Ding, X. Fu and Z. Li, *Angew. Chem. Int. Ed.*, 2012, **51**, 3364-3367.

59 M. Dan-Hardi, C. Serre, T. Frot, L. Rozes, G. Maurin, C. Sanchez and G. Férey, *J. Am. Chem. Soc.*, 2009, **131**, 10857-10859.

60 D. Aulakh, J. B. Pyser, X. Zhang, A. A. Yakovenko, K. R. Dunbar and M. Wriedt, *J. Am. Chem. Soc.*, 2015, **137**, 9254-9257.

61 Y. K. Hwang, D.-Y. Hong, J.-S. Chang, S. H. Jhung, Y.-K. Seo, J. Kim, A. Vimont, M. Daturi, C. Serre and G. Férey, *Angew. Chem. Int. Ed.*, 2008, **47**, 4144-4148.

62 H. Fei and S. M. Cohen, *Chem. Commun.*, 2014, **50**, 4810-4812.

63 P. Deria, J. E. Mondloch, E. Tylianakis, P. Ghosh, W. Bury, R. Q. Snurr, J. T. Hupp and O. K. Farha, *J. Am. Chem. Soc.*, 2013, **135**, 16801-16804.

64 J. Jiang, F. Gándara, Y.-B. Zhang, K. Na, O. M. Yaghi and W. G. Klemperer, *J. Am. Chem. Soc., 2014*, **136**, 12844-12847.

65 M. Kim, J. F. Cahill, Y. Su, K. A. Prather and S. M. Cohen, *Chem. Sci.*, 2012, **3**, 126-130.

66 S. Yuan, W. Lu, Y.-P. Chen, Q. Zhang, T.-F. Liu, D. Feng, X. Wang, J. Qin and H.-C. Zhou, *J. Am. Chem. Soc.*, 2015, **137**, 3177-3180.

67 Z. Wang and S. M. Cohen, *J. Am. Chem. Soc.*, 2007, **129**, 12368-12369.

68 E. A. Kapustin, S. Lee, A. S. Alshammari and O. M. Yaghi, *ACS Cent. Sci.*, 2017, **3**, 662-667.

69 Q.-L. Zhu and Q. Xu, *Chem. Soc. Rev.*, 2014, **43**, 5468-5512.

70 I. Ahmed and S. H. Jhung, *Mater. Today*, 2014, **17**, 136-146.

71 F. P. Kinik, A. Uzun and S. Keskin, *ChemSusChem*, 2017, **10**, 2842-2863.

72 L. Chen, X. Zhang, X. Cheng, Z. Xie, Q. Kuang and L. Zheng, *Nanoscale Adv.*, 2020, **2**, 2628-2647.

73 N. A. Khan, Z. Hasan and S. H. Jhung, *Chem. Commun.*, 2016, **52**, 2561-2564.

74 N. A. Khan, Z. Hasan and S. H. Jhung, *Chem. Eur. J.*, 2014, **20**, 376-380.

75 J. Ma, Y. Ying, X. Guo, H. Huang, D. Liu and C. Zhong, *J. Mater. Chem. A*, 2016, **4**, 7281-7288.

76 S. Abednatanzi, A. Abbasi and M. Masteri-Farahani, *Catal. Commun.*, 2017, **96**, 6-10.

77 A. Aijaz, A. Karkamkar, Y. J. Choi, N. Tsumori, E. Rönnebro, T. Autrey, H. Shioyama and Q. Xu, *J. Am. Chem. Soc.*, 2012, **134**, 13926-13929.

78 B. Tan, Y. Luo, X. Liang, S. Wang, X. Gao, Z. Zhang and Y. Fang, *Micropor. Mesopor. Mat.*, 2019, **286**, 141-148.

79 A. Permyakova, S. Wang, E. Courbon, F. Nouar, N. Heymans, P. D'Ans, N. Barrier, P. Billemont, G. De Weireld, N. Steunou, M. Frère and C. Serre, *J. Mater. Chem. A*, 2017, **5**, 12889-12898.

80 K. Fujie, T. Yamada, R. Ikeda and H. Kitagawa, *Angew. Chem. Int. Ed.*, 2014, **53**, 11302-11305.

81 K. Fujie, R. Ikeda, K. Otsubo, T. Yamada and H. Kitagawa, *Chem. Mater.*, 2015, **27**, 7355-7361.

82 T. Ishida, M. Nagaoka, T. Akita and M. Haruta, *Chem. Eur. J.*, 2008, **14**, 8456-8460.

83 J. Liang, V. Gvilava, C. Jansen, S. Öztürk, A. Spieß, J. Lin, S. Xing, Y. Sun, H. Wang and C. Janiak, *Angew. Chem. Int. Ed.*, 2021, **60**, 15365-15370.

84 S. Hermes, F. Schröder, S. Amirjalayer, R. Schmid and R. A. Fischer, *J. Mater. Chem.*, 2006, **16**, 2464-2472.

85 M. Müller, O. I. Lebedev and R. A. Fischer, *J. Mater. Chem.*, 2008, **18**, 5274-5281.

86 P.-Z. Li, K. Aranishi and Q. Xu, *Chem. Commun.*, 2012, **48**, 3173-3175.

87 J. Settino, T. Sant, C. Micallef, M. Farrugia, C. Spiteri Staines, J. Licari and A. Micallef, Renew. Sustain. *Energy Rev.*, 2018, **90**, 892-909.

88 International Energy Agency, World Energy Outlook. 2011, p 696; http://www.iea.org/publications/freepublications/publication/ weo2011_web.pdf (accessed 17-01-2015).

89 F. Jeremias, A. Khutia, S. K. Henninger and C. Janiak, *J. Mater. Chem.*, 2012, **22**, 10148-10151.

90 M. F. de Lange, K. J. Verouden, T. J. Vlugt, J. Gascon and F. Kapteijn, *Chem. Rev.*, 2015, **115**, 12205-12250.

91 D. B. Boman, D. C. Hoysall, D. G. Pahinkar, M. J. Ponkala and S. Garimella, *Appl. Therm. Eng.*, 2017, **123**, 422-434.

92 V. D. Ugale and A. D. Pitale, *Int. J. Air-Cond. Refrig.*, 2015, **23**, 1530001.

93 M. F. de Lange, B. L. van Velzen, C. P. Ottevanger, K. J. F. M. Verouden, L.-C. Lin, T. J. H. Vlugt, J. Gascon and F. Kapteijn, *Langmuir*, 2015, **31**, 12783-12796.

94 E. Hastürk, S.-J. Ernst and C. Janiak, *Curr. Opin. Chem. Eng*, 2019, **24**, 26-36.

95 EPA. Power Plant Data Highlights. US Environmental Protection Agency https://www.epa.gov/airmarkets/ coal- fired-power- plant-data (2018).

96 F. C. Menz and H. M. Seip, *Environ. Sci. Policy*, 2004, **7**, 253– 265.

97 K. Sumida, D. L. Rogow, J. A. Mason, T. M. McDonald, E. D. Bloch, Z. R. Herm, T.-H. Bae and J. R. Long, *Chem. Rev.*, 2012, **112**, 724–781.

98 R. Quadrelli and S. Peterson, *Energy Policy*, 2007, **35**, 5938–5952.

99 Chemical Attack Fact Sheet: Warfare Agents, Industrial Chemicals, and Toxins; US Department of Homeland Security, 2004. https:// www.dhs.gov/sites/default/files/publications/prep_chemical_fact_ sheet.pdf (accessed on 2020-03-02).

100 World Health Organization, https://www.who.int/en/newsroom/fact-sheets/detail/ambient-(outdoor)-air-quality-andhealth, accessed December 2020.

101 M. O. Andreae and P. Merlet, *Global Biogeochem. Cycles*, 2001, **15**, 955–966.

102 J.-Y. Lee, T. C. Keener and Y. J. Yang, *J. Air Waste Manage. Assoc.*, 2009, **59**, 725–732.

103 R. Zevenhoven and P. Kilpinen, in *Control of Pollutants in Flue Gases and Fuel Gases, Helsinki Univ. of Technology, Otaniemi (Finland)*. Energy Engineering and Environmental Protection, Finland, 2005, ch. 2, pp. 2–4.

104 F. Rezaei, A. A. Rownaghi, S. Monjezi, R. P. Lively and C. W. Jones, *Energy Fuels*, 2015, **29**, 5467–5486.

105 Y. Sun, E. Zwolinska and A. G. Chmielewski, *Environ. Sci. Technol.*, 2016, **46**, 119–142.

106 R. K. Srivastava, W. Jozewicz and C. Singer, *Environ. Prog.*, 2001, **20**, 219–228.

107 T. Islamoglu, Z. Chen, M. C. Wasson, C. T. Buru, K. O. Kirlikovali, U. Afrin, M. R. Mian and O. K. Farha, *Chem. Rev.*, 2020, **120**, 8130-8160.

108 X. Han, S. Yang and M. Schröder, *Nat. Rev. Chem.*, 2019, **3**, 108–118.

109 G. L. Smith, J. E. Eyley, X. Han, X. Zhang, J. Li, N. M. Jacques, H. G. W. Godfrey, S. P. Argent, L. J. McCormick McPherson, S. J. Teat, Y. Cheng, M. D. Frogley, G. Cinque, S. J. Day, C. C. Tang, T. L. Easun, S. Rudić, A. J. Ramirez-Cuesta, S. Yang and M. Schröder, *Nat. Mater.*, 2019, **18**, 1358-1365.

110 M. Savage, I. da Silva, M. Johnson, J. H. Carter, R. Newby, M. Suyetin, E. Besley, P. Manuel, S. Rudić, A. N. Fitch, C. Murray, W. I. F. David, S. Yang and M. Schröder, *J. Am. Chem. Soc.*, 2016, **138**, 9119-9127.

111 M. Savage, Y. Cheng, T. L. Easun, J. E. Eyley, S. P. Argent, M. R. Warren, W. Lewis, C. Murray, C. C. Tang, M. D. Frogley, G. Cinque, J. Sun, S. Rudić, R. T. Murden, M. J. Benham, A. N. Fitch, A. J. Blake, A. J. Ramirez-Cuesta, S. Yang and M. Schröder, *Adv. Mater.*, 2016, **28**, 8705–8711.

112 L. M. Rodríguez-Albelo, E. López-Maya, S. Hamad, A. R. Ruiz-Salvador, S. Calero and J. A. R. Navarro, *Nat. Commun.*, 2017, **8**, 14457.

113 X. Cui, Q. Yang, L. Yang, R. Krishna, Z. Zhang, Z. Bao, H. Wu, Q. Ren, W. Zhou, B. Chen and H. Xing, *Adv. Mater.*, 2017, **29**, 1606929.

114 J. Hungerford, S. Bhattacharyya, U. Tumuluri, S. Nair, Z. Wu and K. S. Walton, *J. Phys. Chem. C*, 2018, **122**, 23493–23500.

115 W. P. Mounfield, C. Han, S. H. Pang, U. Tumuluri, Y. Jiao, S. Bhattacharyya, M. R. Dutzer, S. Nair, Z. Wu, R. P. Lively, D. S. Sholl and K. S. Walton, *J. Phys. Chem. C*, 2016, **120**, 27230–27240.

116 D. Feng, W.-C. Chung, Z. Wei, Z.-Y. Gu, H.-L. Jiang, Y.-P. Chen, D. J. Darensbourg and H.-C. Zhou, *J. Am. Chem. Soc.*, 2013, **135**, 17105-17110.

117 A. Fateeva, P. A. Chater, C. P. Ireland, A. A. Tahir, Y. Z. Khimyak, P. V. Wiper, J. R. Darwent and M. J. Rosseinsky, *Angew. Chem. Int. Ed.*, 2012, **51**, 7440-7444.

118 M. R. Rezaei Kahkha, S. Daliran, A. R. Oveisi, M. Kaykhaii and Z. Sepehri, *Food Anal. Methods*, 2017, **10**, 2175-2184.

119 D. Feng, Z.-Y. Gu, J.-R. Li, H.-L. Jiang, Z. Wei and H.-C. Zhou, *Angew. Chem. Int. Ed.*, 2012, **51**, 10307-10310.

120 T. Kunde, E. Nieland, H. V. Schröder, C. A. Schalley and B. M. Schmidt, *Chem. Commun.*, 2020, **56**, 4761-4764.